Doklady Physics, Vol. 45, No. 11, 2000, pp. 569–573. Translated from Doklady Akademii Nauk, Vol. 375, No. 2, 2000, pp. 172–176.
Original Russian Text Copyright © 2000 by Aleksandrov.

PHYSICS

Theory of Solidification with a Quasi-Equilibrium Two-Phase Zone

D. V. Aleksandrov

Presented by Academician N. A. Vatolin February 4, 2000

Received February 15, 2000

Directed solidification of binary melts is commonly used for producing metal ingots, whose quality is determined by the transition character of the metal from the liquid to solid state [1, 2]. The metal undergoing solidification consists of three regions, in which it is in solid, liquid, and two-phase states, respectively. Being situated between the liquid and solid zones, the two-phase region determines all general properties of the solid phase [3]. This region forms mainly due to supercooling occurring in the melt ahead of the crystallization front [4]. Supercooling arising under certain conditions is related to concentration changes (diffusion) which cause the formation of a region where the melt temperature is lower than the equilibrium temperature of the phase transition; consequently, the melt is in the metastable state. Thus, concentration-caused supercooling can lead to the formation of a cellular front, a dendritic structure, and so forth. According to experimental papers [5, 6], the solidification of metal melts is accompanied by the fast formation of a dendritic structure. This leads to the removal of supercooling attained through heat release by dendrite growth in the two-phase zone. The system of equations of heat-and-mass transfer describing crystallization under such conditions was first proposed by V.T. Borisov in [3, 7], and the two-phase zone was then referred to as the quasi-equilibrium zone.

The nonlinear system of equations of the quasi-equilibrium two-phase zone was analyzed by asymptotic methods in [8, 9]. Based on the obtained solutions, the authors of these papers were able to replace the two-phase zone with a discontinuity surface in the case of both the "narrow" [8] and "wide" [9] zone. Analysis of the stability of these solutions was carried out afterwards in [10–12]. We note that the obtained solutions far from involve all the possible cases of solidification because the parameters, in terms of which the asymptotic expansions are written, are not always small. This paper presents the general analytic solution to the system of equations describing the quasi-equilibrium two-phase zone and also presents calculations of temperature and impurity-concentration jumps caused by passing across the two-phase zone. With these jumps in mind, we replaced the quasi-equilibrium two-phase with a discontinuity surface which separated the solid and liquid phases in the general case.

We consider the solidification of a binary melt with fixed temperature gradients in the solid phase (g_s) and in the melt (g_l). The solidification rate u_s and the width of the two-phase zone δ are assumed to be steady-state. The solid phase and the melt occupy the regions $\xi < u_s\tau$ and $\xi > u_s\tau + \delta$, respectively, where ξ is the coordinate and τ is the time. Plane $\xi = u_s\tau$ is the boundary between the solid phase and the two-phase zone, whereas plane $\xi = u_s\tau + \delta$ separates the two-phase zone from the melt. The system of equations for heat-and-mass transfer in the quasi-equilibrium two-phase zone has the following form (as usual, the diffusion of the impurities is neglected in the solid phase):

$$\frac{\partial}{\partial\tau}[(1-\varphi)\sigma] = \frac{\partial}{\partial\xi}\left(D\frac{\partial\sigma}{\partial\xi}\right) - k\sigma\frac{\partial\varphi}{\partial\tau}; \tag{1}$$

$$\frac{\partial}{\partial\xi}\left(\lambda\frac{\partial\theta}{\partial\xi}\right) + \rho L\frac{\partial\varphi}{\partial\tau} = 0, \quad \theta = \theta_0 - m\sigma, \quad u_s\tau < \xi < u_s\tau + \delta; \tag{2}$$

$$\frac{\partial\sigma_l}{\partial\tau} = D_l\frac{\partial^2\sigma_l}{\partial\xi^2}, \quad \frac{\partial\theta_l}{\partial\xi} = g_l, \quad \xi > u_s\tau + \delta, \quad \frac{\partial\theta_s}{\partial\xi} = g_s, \quad \xi < u_s\tau. \tag{3}$$

Here, σ and σ_l are the impurity concentrations in the two-phase zone and in the melt, respectively; θ_l, θ_s, and θ are the temperatures in the melt, solid phase, and two-phase zone, respectively; θ_0 is the transition temperature of the pure melt; φ is the volume fraction of the solid phase in the two-phase zone; D and D_l are the diffusion coefficients in the two-phase zone and in the melt, respectively; m is the slope of the liquidus line; k is the equilibrium distribution coefficient of the impurity; ρ is the density; L is the latent heat of the phase

Ural State University,
pr. Lenina 51, Yekaterinburg, 620083 Russia

1028-3358/00/4511-0569$20.00 © 2000 MAIK "Nauka/Interperiodica"

transition; and λ is the heat conductivity in the two-phase zone.

The terms proportional to $\frac{\partial\varphi}{\partial\tau}$ in Eqs. (1) and (2) correspond to the trapping of impurities and heat release, both of which result from the formation of solid-phase domains in the two-phase zone. The second equation in (2), i.e., the condition of the quasi-equilibrium state of the two-phase zone, indicates that the temperature in the two-phase zone is equal to the transition temperature of the binary melt. In the region characterized by linear scale l and thermal diffusivity a, the relaxation time of the temperature field $\tau_a = \frac{l^2}{a}$ is much shorter than that of the diffusion field $\tau_D = \frac{l^2}{D_l}$ $\left(\frac{\tau_a}{\tau_D} \sim 10^{-3}\text{–}10^{-4}\right)$. Therefore, derivatives of temperature with respect to time are neglected in the equations of heat conduction. We consider that, far from the boundary between the two-phase zone and the melt, the impurity concentration is known:

$$\sigma \longrightarrow \sigma_\infty, \quad \xi \longrightarrow \infty. \tag{4}$$

The following conditions of heat-and-mass balance are met at surfaces $\xi = u_s\tau$ and $\xi = u_s\tau + \delta$, which bound the two-phase zone:

$$\lambda_s g_s - \lambda\frac{\partial\theta}{\partial\xi} = \rho L(1-\varphi)u_s, \quad \xi = u_s\tau; \tag{5}$$

$$(1-k)(1-\varphi)\sigma u_s + D\frac{\partial\sigma}{\partial\xi} = 0, \quad \xi = u_s\tau; \tag{6}$$

$$\varphi = 0, \quad \sigma = \sigma_l, \quad D\frac{\partial\sigma}{\partial\xi} = D_l\frac{\partial\sigma_l}{\partial\xi}, \quad \xi = u_s\tau + \delta. \tag{7}$$

The transport coefficients characterizing the two-phase zone are calculated using the simplest formulas,

$$\lambda = \lambda_l(1-\varphi) + \lambda_s\varphi, \quad D = D_l(1-\varphi), \tag{8}$$

which correspond to the well-known mixture rule. The model presented here is substantiated in detail in [8, 13].

In the reference system having velocity u_s, the solidification process is steady. Therefore, after transformation to this system, we can integrate the first equation in (2). Then, using the result from boundary condition (5), we can represent solidification rate u_s as

$$u_s = \frac{\lambda_s g_s - \lambda_l g_l}{\rho L}. \tag{9}$$

Let us introduce the following dimensionless variables and parameters:

$$x = \frac{u_s(\xi - u_s\tau)}{D_l}, \quad t = \frac{u_s^2\tau}{D_l}, \quad c = \frac{\sigma}{\sigma_\infty},$$

$$T = \frac{\theta}{m\sigma_\infty}, \quad \Lambda_1 = \frac{\lambda_l}{\lambda_s}, \quad P = \frac{\lambda_s m\sigma_\infty}{\rho L D_l}, \tag{10}$$

$$\varepsilon = \frac{\delta u_s}{D_l}, \quad G_l = \frac{g_l D_l}{m\sigma_\infty u_s}.$$

Eliminating temperature T in (1)–(9) with the help of the quasi-equilibrium state condition and using variables (10), we obtain two equations for functions $\varphi(x)$ and $c(x)$ at $0 < x < \varepsilon$ and boundary conditions in the form

$$\frac{d}{dx}\left[(1-\varphi)\left(\frac{dc}{dx} + c\right)\right] + kc\frac{d\varphi}{dx} = 0,$$
$$\frac{dc}{dx} = -\frac{\varphi + PG_l\Lambda_1}{P[\Lambda_1(1-\varphi) + \varphi]}; \tag{11}$$

$$(1-k)c + \frac{dc}{dx} = 0, \quad x = 0; \tag{12}$$

$$\varphi = 0, \quad c = 1 + G_l, \quad \frac{dc}{dx} = -G_l, \quad x = \varepsilon. \tag{13}$$

Condition (13) determines the zone width ε. Below, we consider the exact solution to system (11)–(13). The first equations in (11) is multiplied by dx with substitution of $\frac{dc}{dx}$ with the expression given in the second equation in (11). This leads to the differential equation determining function $c(\varphi(x))$:

$$(1-\varphi)\frac{dc}{d\varphi} - (1-k)c = \frac{1}{P}\frac{d}{d\varphi}\left[\frac{(1-\varphi)(\varphi + PG_l\Lambda_1)}{\Lambda_1(1-\varphi) + \varphi}\right].$$

Its solution, meeting boundary condition (13), has the form

$$c(\varphi(x)) = (1-\varphi)^{k-1}\left[1 + G_l + \frac{J(\varphi)}{P}\right], \tag{14}$$

$$J(\varphi) = \int_0^\varphi \frac{\Lambda_1(1-y)^2 - y^2 - PG_l\Lambda_1}{(1-y)^k[\Lambda_1(1-y) + y]^2}dy. \tag{15}$$

Substituting $\frac{dc}{dx}$ in the form $\frac{dc}{dx} = \frac{dc}{d\varphi}\frac{d\varphi}{dx}$ into the second equation in (11) and calculating $\frac{dc}{d\varphi}$, we get a dif-

ferential equation for $\varphi(x)$. Its solution has the form ($x = \varepsilon$, $\varphi = 0$):

$$x(\varphi) = \varepsilon - \int_0^{\varphi} \frac{d}{dy}\left[\left(1 + G_l + \frac{J(y)}{P}\right)(1-y)^{k-1}\right] \times \frac{P[\Lambda_l(1-y)+y]}{y + PG_l\Lambda_1}dy. \quad (16)$$

We denote the volume fraction of the solid phase at the left boundary $x = 0$ as φ_* and, by using (12), obtain the following equation for φ_*:

$$\frac{dc}{dx} = -(1-k)c, \quad \varphi = \varphi_*.$$

Then, $c(\varphi)$ is taken from (14) at $\varphi = \varphi_*$, $\frac{dc}{dx}$ is taken from the second equation in (11), and both are substituted into the previous equation. As a result, we have

$$\frac{\varphi_* + PG_l\Lambda_1}{P[\Lambda_1(1-\varphi_*)+\varphi_*]} = (1-k)(1-\varphi_*)^{k-1}\left[1 + G_l + \frac{1}{P}J(\varphi_*)\right]. \quad (17)$$

Substitution of $x = 0$ and $\varphi = \varphi_*$ into (16) yields the equation for the dimensionless width of the two-phase zone:

$$\varepsilon = \int_0^{\varphi_*} \frac{d}{dy}\left[\left(1 + G_l + \frac{J(y)}{P}\right)(1-y)^{k-1}\right] \times \frac{P[\Lambda_1(1-y)+y]}{y + PG_l\Lambda_1}dy. \quad (18)$$

Thus, the width of the two-phase zone is expressed in terms of thermal parameters. Figure 1 demonstrates plots $\varphi_*(g_s)$ and $\varepsilon(g_s)$ at $g_l = 1$°C/cm, which are calculated according to formulas (17) and (18) [velocity u_s, involved in dimensionless temperature gradient G_l, is eliminated by using relation (9)]. Under the assumption of a fixed value of gradient g_l, the dependence of the dimensional zone width δ on the solid-phase temperature gradient g_s,

$$\delta(g_s) = \frac{\varepsilon(g_s)D_l\rho L}{\lambda_s g_s - \lambda_l g_l}, \quad (19)$$

is derived by eliminating velocity u_s using expression (9). The corresponding curve is shown in Fig. 2. Function $x(\varphi)$ can be easily constructed by substituting $\varepsilon(g_s)$ from (18) into (16). The inverse function $\varphi(x)$ is plotted in Fig. 3. The concentration $c(x)$ of impurities in the solid phase (Fig. 3) is determined by substitution of the derived function into (14) and (15).

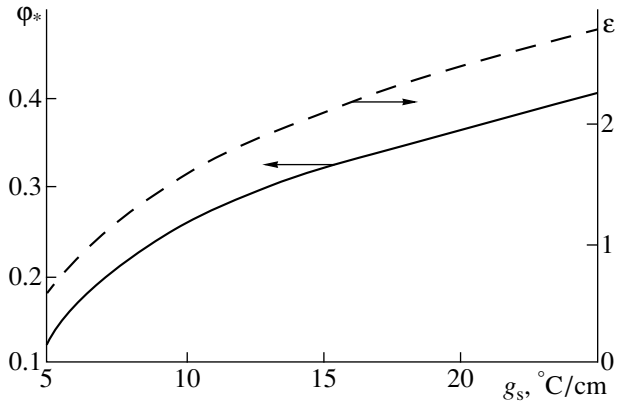

Fig. 1. $\varphi_*(g_s)$ and $\varepsilon(g_s)$ plots for the Fe–Ni alloy at $k = 0.68$, $m = 2.65$°C/wt %, $L = 485.5$ cal/g, $D_l = 5 \times 10^{-5}$ cm^2/s, $\rho = 7$ g/cm^3, $\lambda_l = 0.1$ cal cm °C/s, $\lambda_s = 0.177$ cal cm °C/s, $\sigma_\infty = 0.3$.

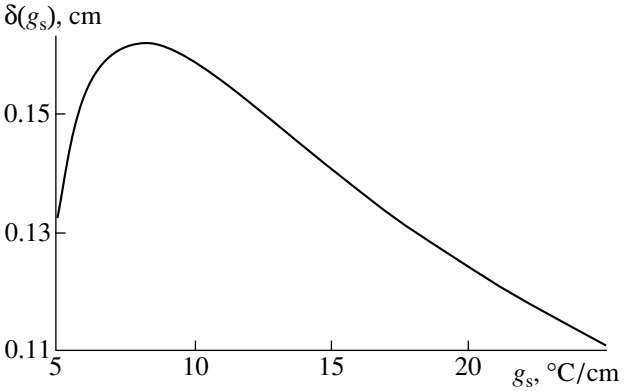

Fig. 2. $\delta(g_s)$ at $g_l = 1$°C/cm plots for the Fe–Ni alloy, whose thermal and physical characteristics correspond to Fig. 1.

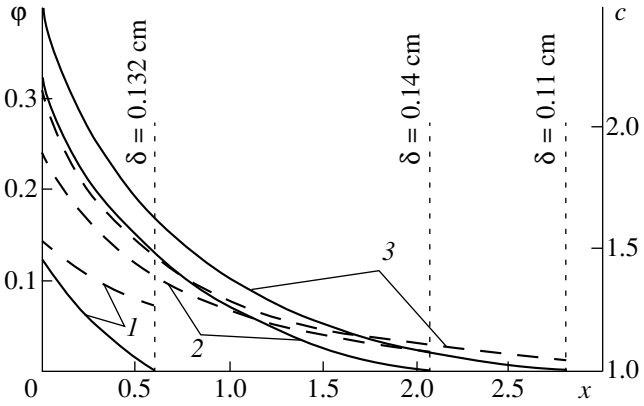

Fig. 3. $\varphi(x)$ (solid curves) and $c(x)$ (dashed curves) plots for the Fe–Ni alloy with thermal and physical characteristics corresponding to Fig. 1 at $g_l = 1$°C/cm and (*1*) $g_s = 5$, (*2*) 15, and (*3*) 25°C/cm. Vertical lines show the width δ of the quasi-equilibrium two-phase zone, which is calculated by formula (19) at the given gradients and conforms to Fig. 2.

Thus, the complete solution to the problem of directed solidification of a binary melt having a quasi-equilibrium two-phase zone is given by relationships (14)–(19).

The obtained solutions have the form of implicit functions. Therefore, to carry out stability analysis, solidification with a quasi-equilibrium two-phase zone should be replaced with an equivalent frontal process. The main idea lies in the substitution of the discontinuity surface $\xi = \Sigma(\tau)$ separating the solid phase from the melt for the actual two-phase zone. After this substitution, in the solid phase and the melt, the problem is described by equations of heat conduction at temperatures θ_s and θ_l, respectively. In the melt, there is an additional equation of impurity diffusion corresponding to concentration σ_l. The position of boundary $\Sigma(\tau)$ is also unknown in these second-order equations. Therefore, to solve the problem, it is necessary to specify seven boundary conditions. Three of them are specified far from the discontinuity surface (for example, it is possible to fix the temperature gradients and impurity concentration in the melt). The other four boundary conditions are obtained in the following way.

The temperature at the boundary separating the two-phase zone from the melt must be equal to the phase transition temperature:

$$\theta_l = \theta_0 - m\sigma_l, \quad \xi = \Sigma(\tau). \tag{20}$$

Another boundary condition results from condition $\theta \equiv \theta_0 - m\sigma$ $\left(\text{or } \dfrac{\partial\theta}{\partial\xi} \equiv -m\dfrac{\partial\sigma}{\partial\xi}\right)$, which is valid inside the two-phase zone, and from the boundary conditions given at the boundary between the two-phase zone and the melt:

$$\frac{\partial\theta}{\partial\xi} = \frac{\partial\theta_l}{\partial\xi}, \quad \frac{\partial\sigma}{\partial\xi} = \frac{\partial\sigma_l}{\partial\xi}.$$

It has the form

$$\frac{\partial\theta_l}{\partial\xi} = -m\frac{\partial\sigma_l}{\partial\xi}, \quad \xi = \Sigma(\tau). \tag{21}$$

Then, using condition (9), we can write the boundary condition related to the heat balance:

$$\lambda_s\frac{\partial\theta_s}{\partial\xi} - \lambda_l\frac{\partial\theta_l}{\partial\xi} = \rho L\frac{d\Sigma}{d\tau}, \quad \xi = \Sigma(\tau). \tag{22}$$

The last condition specified at $\xi = \Sigma(\tau)$ determines the temperature jump. Taking into account the condition of quasi-equilibrium and formulas (11) and (12), we find

$$\theta_s - \theta_l = m\sigma_\infty(c|_{x=\varepsilon} - c|_{x=0})$$

$$= m\sigma_\infty(1 + G_l) - \frac{m\sigma_\infty}{(1-k)P\Lambda_1(1-\varphi_*) + \varphi_*}.$$

At $\xi = \Sigma(\tau)$, the second term in the right-hand side of the above relationship can be expressed in terms of the jump of the temperature derivative:

$$\frac{1}{m\sigma_\infty}\left[\frac{d\theta_l}{dx} - \frac{d\theta_s}{dx}\right] = \left.\frac{dc}{dx}\right|_{x=0} - \left.\frac{dc}{dx}\right|_{x=\varepsilon}$$

$$= G_l - \frac{\varphi_* + PG_l\Lambda_1}{P[\Lambda_1(1-\varphi_*) + \varphi_*]}.$$

Here, the condition of the quasi-equilibrium state, the boundary conditions (12) and (13), and the second Eq. (11) are taken into account. The dimensional final expression presented below is obtained by eliminating the second terms in the right-hand sides of the last two relationships and by substituting u_s with $\dfrac{d\Sigma}{d\tau}$, g_l with $\dfrac{\partial\theta_l}{\partial\xi}$, and $\dfrac{d}{dx}$ with $u_s^{-1}D_l\dfrac{\partial}{\partial\xi}$:

$$(1-k)\frac{\partial\theta_l}{\partial\xi} - \frac{\partial\theta_s}{\partial\xi} = \frac{1-k}{D_l}(\theta_s - \theta_l - m\sigma_\infty)\frac{d\Sigma}{d\tau}, \tag{23}$$

$$\xi = \Sigma(\tau).$$

Stability analysis of the formulated model with the boundary conditions (20)–(23) specified at the discontinuity surface can now be carried out in the general case in analogy to papers [10–12]. Note that stability regions were found earlier in certain limiting cases [11, 12]. This means that, in these cases, the solution derived is stable.

Thus, in this paper, we have constructed the general solution to the classical system of nonlinear equations describing the quasi-equilibrium two-phase zone. This system was first proposed by Borisov in the early 1960s. The solution found allows us to calculate the jumps of thermal parameters corresponding to a pass through the two-phase zone and to replace them, in the general case, by a discontinuity surface between the solid phase and the melt. As a result, stability analysis can be carried out in the general case and we can apply conventional numerical methods for solving time-dependent problems with one moving boundary.

ACKNOWLEDGMENTS

This work was supported by INTAS (grant no. 96-0457) within the scope of the research program of the International Center of Fundamental Physics (Moscow).

REFERENCES

1. M. Flemings, *Solidification Processing* (McGraw-Hill, New York, 1974; Mir, Moscow, 1977).
2. B. Chalmers, *Principles of Solidification* (Wiley, New York, 1964; Metallurgiya, Moscow, 1968).
3. V. T. Borisov, *Theory of Two-Phase Zones in Metal Ingots* (Metallurgiya, Moscow, 1987).

4. G. P. Ivantsov, Dokl. Akad. Nauk SSSR **81** (2), 179 (1951).
5. V. T. Borisov and Yu. E. Matveev, Fiz. Met. Metalloved. **13**, 456 (1962).
6. B. W. Webb and R. Viskanta, in *Proceedings of the VIII International Conference on Heat Transfer, San Francisco, 1986* (Washington, 1986), Vol. 4, Gen. Papers.
7. V. T. Borisov, Dokl. Akad. Nauk SSSR **136**, 583 (1961) [Sov. Phys. Dokl. **6**, 74 (1961)].
8. Yu. A. Buevich, L. Yu. Iskakova, and V. V. Mansurov, Prikl. Mekh. Tekh. Fiz., No. 4, 46 (1990).
9. L. Yu. Iskakova and V. V. Mansurov, Rasplavy, No. 1, 82 (1994).
10. D. V. Aleksandrov and V. V. Mansurov, Kristallografiya **41**, 376 (1996) [Crystallogr. Rep. **41**, 357 (1996)].
11. D. V. Aleksandrov and V. V. Mansurov, Kristallografiya **42**, 402 (1997) [Crystallogr. Rep. **42**, 357 (1997)].
12. Yu. A. Buyevich, D. V. Alexandrov, and V. V. Mansurov, *Macrokinetics of Crystallization* (Begell House, New York, 1999).
13. N. A. Avdonin, *Mathematical Formulation of Crystallization Processes* (Zinatne, Riga, 1980).

Translated by Yu. Verevochkin

Doklady Physics, Vol. 45, No. 11, 2000, pp. 574–577. Translated from Doklady Akademii Nauk, Vol. 375, No. 2, 2000, pp. 177–180.
Original Russian Text Copyright © 2000 by Zakhidov, Kasymdzhanov, Kurbanov, Khabibullaev.

PHYSICS

Luminescence Centers on the Surface of Optical Glasses

É. A. Zakhidov, M. A. Kasymdzhanov, S. S. Kurbanov, and Corresponding Member of the RAS P. K. Khabibullaev

Received June 23, 2000

The study of the nature and properties of different glass defects, particularly in silicate glass, is of interest in solid state physics and chemistry and bears important significance on practical applications in the commercial production of optical fibers, optical systems, and microelectronic devices. These defects can be situated both in the bulk and on the surface of the solid. The bulk and surface defects of silicon dioxides, such as E'-centers, nonbridge oxygen atoms, peroxide radicals, and others, possess similar optical characteristics [1, 2].

On the glass surface, certain radicals like $\equiv Si^0$, $\equiv SiO^0$, $\equiv SiOO^0$, $\equiv SiOCO^0$, $\equiv SiONN^0$ can be stabilized and, thus, their individual absorption spectra can be identified [3]. However, while in contact with the environment, these defects are rapidly modified and under natural conditions, paramagnetic centers on the surface of the silicon dioxide are not detected. The characteristics of the surface layers always differ from those in the bulk of the material due to the sharp changes occurring at the phase boundary and in its vicinity. Silicate glass usually has a large chemical affinity for water vapor. Being in contact with an ambient atmosphere containing unsaturated water vapors, the freshly prepared surface of the silicate glass reacts with the active surface regions and forms OH^- ions (chemisorption). At longer exposures, adsorbed water reacts with an alkaline glass component, forming alkaline solutions on the surface. Thermal treatment of the glass surface may lead to its dehydration accompanied by the formation of two-, three-, and four-term rings consisting of Si and O atoms [4]. The three-term rings are stressed and decompose for the first turn under external actions.

Improved methods of synthesis and purification of initial glass constituents have made it possible to essentially lower the concentration of dyeing elements in the glass bulk. As a result, impurity bands in the absorption spectrum of the quartz glass disappear. The absence or low intensity of the doped luminescence enabled us to find a new form of previously unobserved luminescence in massive silicate glass, namely, rapid broadband luminescence excited within the glass transmission band [5–8]. As additional investigations have demonstrated, this luminescence is related to quasimolecular complexes composed of elements of a basic substance and an impurity.

With decreasing impurity concentration, the luminescence intensity excited in the bulk of glass also decreases. However, in this case, under normal conditions, it is impossible to provide for the glass surface purity as compared to the glass bulk purity. In this connection, the intensities of surface and bulk luminescence in certain conditions can be commensurable, although the thickness of the excited layers is significantly smaller in the former case. Therefore, in the high-purity glasses, the contribution of the surface luminescence to the bulk (rapid broadband) luminescence can be significant, especially when the thickness of the samples under investigation is small and the glass surface luminescence also arrives at the spectrometer slit. Usually, in high-purity glasses, the radiation intensity from the bulk of the material is quite low. As investigations [9] have shown, impurity concentrations in the bulk of glass and on its surface may differ by several orders of magnitude. The goal of the present study is to investigate the spectral-kinetic characteristics of the surface luminescence for pure quartz glass and multicomponent silicon glass under the action of UV radiation and to determine the contribution of the surface luminescence to the luminescence of the entire sample.

The investigations were performed with the help of a modernized spectral-computational KSVU-23 setup composed of an MDR-23 monochromator and signal acquisition and processing systems. The system for detecting optical signals consisted of FEU-77, FEU-79, and FEU-100 photodetectors and a boxcar integrator, making it possible to detect signals by the pulse-strobing method. The spectral range under investigation was 200 to 850 nm; the setup time resolution was not worse than 5 ns. The strobe width changed from 10 ns to 400 μs. This made it possible to set up a strobe at a certain part of the pulse being investigated and to detect spectra resolved in time. The bulk and surface luminescence were excited by a nitrogen-laser beam (with a wavelength of 337 nm, a duration of ~9 ns, and a power of ~15 kW) at an angle of 90° with respect to the regis-

Department of Thermal Physics, Academy of Sciences of Uzbekistan, ul. Katartal 28, kvartal Ts, Chilanzar, Tashkent, 700135 Uzbekistan

1028-3358/00/4511-0574$20.00 © 2000 MAIK “Nauka/Interperiodica”

tration axis. The results obtained were analyzed by a computer. We have investigated quartz glasses with trademarks KI, KU-2, KU-1, and KUVI (types I to IV) high-purity multicomponent silicon glass of the K1082 and F1087 types consisting of 70% silicon dioxide, and commercial glasses K8 and TF-1. The samples had high-quality polished surfaces. The sample thickness was from 10 to 12 mm.

The luminescence spectra were recorded with the help of a special diaphragm with dimensions of 5×5 mm, which was placed directly in front of the sample. In the cases when the position of the diaphragm was in the middle or at the edge of the sample, we recorded, correspondingly, the luminescence radiated only by the bulk or by both the bulk and the surface. In certain cases, the surface luminescence was excited by radiation slipping over the surface when the radiation fell onto the surface at a very acute angle.

Recording luminescence spectra of optical glass along with the luminescence of its surface has shown that they are more complicated in comparison with the case of the bulk. These spectra contain an additional long-wave band in the vicinity of 520 nm which determines the appearance of two spectral maxima in the luminescence spectrum or a maximum shifted towards the long-wave side. Figure 1 shows the luminescence spectra for both the bulk + surface (curve *1*) and bulk only (curve *2*) for the KU-1 (Fig. 1a) and KUVI (Fig. 1b) quartz glasses and for the K1082 multicomponent glass (Fig. 1c). We recorded only the rapidly damping part of the luminescence (the strobe width was 40 ns without time delay). Analysis of the luminescence spectra shows that the short-wave parts of the bulk + surface spectra and the pure bulk spectra coincide exactly, provided they are properly normalized. Such a coincidence is observed for all investigated samples and makes it possible to assume that the short-wave part of the bulk + surface luminescence spectrum is determined by the bulk luminescence centers, whereas the long-wave part is determined by both the bulk and the surface centers. Under this assumption, the bulk luminescence spectra were subtracted from the bulk + surface spectra. The difference spectra derived by this method are given in Fig. 1 (curves *3*). These spectra may be considered as the luminescence spectra for the glass surfaces. The surface luminescence spectra for the three types (KU-1, KUVI, and KI-2) of quartz glass have spectral maxima in the vicinity of 530 nm, which weakly differ from each other. At the same time, spectra of the KI quartz glass and of the K1082 multicomponent glass have their maxima in the vicinity of ~480 nm.

Investigations of time characteristics have shown that the attenuation of the surface luminescence has no exponential nature and that its full width at the half-maximum is on the order of 10 to 15 ns. The nonexponential nature of the attenuation law is well pronounced in the luminescence spectra obtained by the time-resolution method. For example, the steady luminescence spectrum of the KU-2 glass is much wider than that of the fast component (both obtained with a strobe width of 40 μs and without any time delay) and has a second impurity line at ~450 nm.

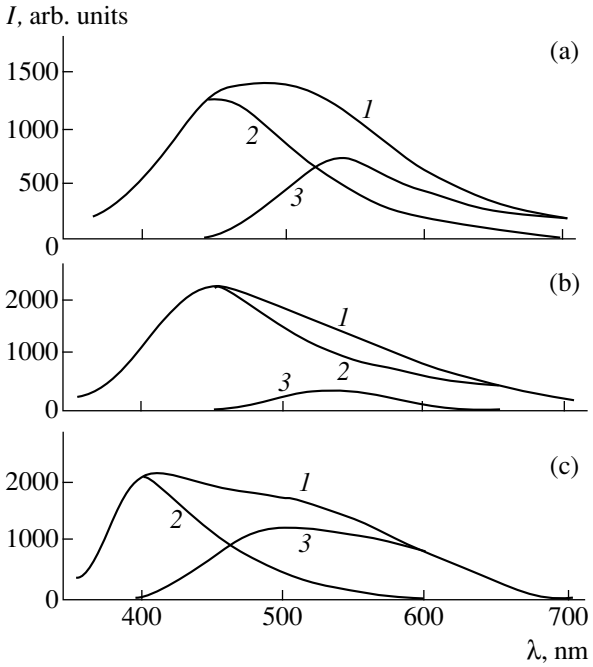

Fig. 1. Luminescence spectra for (a) KU-1, (b) KUVI, and (c) K1082 silicon glasses, which were measured under different conditions: (*1*) bulk + surface; (*2*) only bulk; (*3*) the luminescence spectrum obtained by subtracting spectrum (*2*) from spectrum (*1*) for a strobe width of 40 ns and zero time delay.

An increase in temperature leads to the temperature quenching of the luminescence. When a sample is heated from 20 to 300°C, the intensities of the bulk + surface luminescence and the bulk luminescence alone decrease by a factor of ~4.5 and ~2.5, respectively. The former spectra obtained at temperatures of 20 and 300°C differ insignificantly from one another, even though they have different thermal quenching coefficients. This might be related to the small overlap of the bulk and surface impurity lines.

As is seen from the bulk + surface spectra and the difference spectra, the relation between the bulk- and surface-luminescence intensities depends on the type of quartz glass. The statistical weight of the surface luminescence is the highest for the KU-1 quartz glass. In the K8, F1087, and TF-1 commercial optical glasses, the surface luminescence is not seen against the background of the intense bulk luminescence. In the case of the dispersive SiO_2, whose surface is well developed, the reversed situation is observed; i.e., the surface luminescence dominates in the luminescence spectrum [10]. As was established previously [6], the rapid broadband luminescence intensity, i.e., the bulk luminescence, increases in quartz glasses in accordance with the fol-

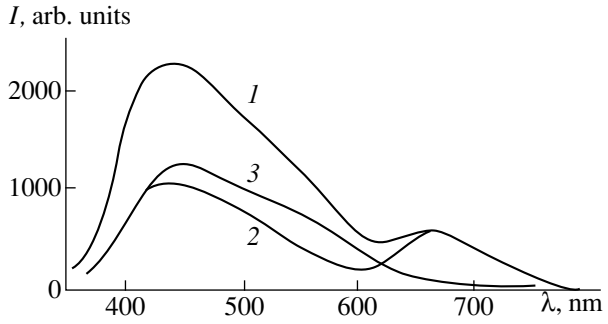

Fig. 2. Luminescence spectra for KU-2 quartz glass irradiated by γ-rays at a dose of 10^5 rad, which were measured under different conditions: (*1*) bulk + surface; (*2*) only bulk; (*3*) the luminescence spectrum obtained by subtracting spectrum (*2*) from spectrum (*1*) for a strobe width of 40 ns and zero time delay.

lowing sequence: KU-1, KSG (type III), KUVI (type IV), KU-2, KV (type II), and KI (type I). Hence, we may conclude that, indeed, the luminescence intensity does not change significantly from one glass sample to another and is determined, as a whole, by the polishing quality and the surface purity. The same conclusion also follows from analyzing the mechanisms of the formation of luminescence centers on the glass surface. Unlike the bulk luminescence centers, the surface centers are more subjected to the action of the environment. For example, the intensity of the surface luminescence for dispersive SiO_2 changes by a factor of ~1.6 [10] depending on the measurement conditions, i.e., whether they are performed in ambient air or in vacuum. After mechanical treatment, nonbridge-oxygen-atom and peroxide-radical type defects are formed on the surface of silicon dioxide relatively easily and their concentration before contact with the environment and interaction with its atoms is larger than in the case of the same bulk defects [2]. Therefore, we can suppose that, in our case, the luminescence surface centers are formed mainly during the mechanical processing of the glass surface and are modified under the influence of environmental atoms.

The luminescence centers may also be formed and stabilized in the bulk and on the surface of a substance under the action of radiation. To elucidate the role of radiation in forming the surface luminescence centers, we have investigated the surface luminescence of a KU-2 glass exposed 9 years ago to γ-rays at a dose of 10^5 rad. Absorption spectrum measurements show that an additional absorption induced by the radiation is not yet completely annealed. In Fig. 2, the bulk + surface (curve *1*) and bulk (curve *2*) steady luminescence spectra (the strobe width is 40 μs) for the KU-2 γ-irradiated glass and the difference spectrum obtained by subtracting the latter from the former are presented under the assumption that the impurity line at 670 nm is determined only by the bulk centers. This assumption is based on the results of [2], wherein, after contact with the environment, the surface centers of the nonbridge oxygen atoms are not observed. On the other hand, the power density of the nitrogen laser (~1 MW/cm^2) used in the experiments is not sufficient to destroy the glass surface. As is shown in [11], when destroying the SiO_2 surface by intense UV radiation, luminescence maxima at 440, 560, and 650 nm are observed. In the authors' opinion, the first and third luminescence bands are determined by the E'-center and nonbridge oxygen atom, respectively, while the second band is related to silicon nanoparticles. As is seen from analyzing the steady spectra for the surface luminescence of KU-2 quartz-glass samples irradiated and not irradiated by γ-rays, the γ-radiation leads only to a change in the relation between the intensities of the impurity lines at ~450 and ~520 nm. This relation changes in favor of the first line. The same changes occur with the impurity line at ~535 nm in the luminescence spectrum for the quartz glass of special manufacture, in which the concentration of transient metals, OH groups, and Cl_2 is lower than 10^{-5} wt %. These changes indicate that after (or during) γ-irradiation, the new luminescence centers appear on the sample surface. They may be formed as a result of the breaking off of OH bonds and the replacement of hydrogen by another element (impurity) with subsequent formation of a quasi-molecular complex consisting of elements of the basic substance and the impurity, as is the case for the rapid broadband luminescence. The same mechanism of center formation may also be suggested for the case of mechanically processing the glass surface, in which complexes can be formed by attaching impurities of broken ≡Si–O bonds appearing in great amount when the glass surface is ground or polished. The spectral-kinetic characteristics of the surface luminescence are the following: universality of the phenomenon for most optical glasses, close location of maxima, short durations, and a nonexponential character of the attenuation laws. The sensitivity to γ-radiation and temperature also indicates that the surface luminescence can have the same nature as that with the bulk luminescence of optical glasses (rapid broadband luminescence), which is excited within the glass transmission band.

In contrast to complexes being formed in the glass bulk, impurities that are absent there but available in great amounts in the environment can also participate in the creation of surface complexes. Therefore, the luminescence spectrum of surface complexes differs from that of bulk complexes. The energy states of a quasi-molecular complex depend strongly on the position, charge, and size of the impurity ion. Hence, we may expect that a complex formed with the participation of the same impurity ion will possess different energy characteristics depending on whether it is formed on the surface or in the bulk of the material. On the glass surface, the distance between a nonbridge oxygen atom and an impurity ion differs from that between them in the glass bulk. Therefore, the impurity

ion has a larger degree of freedom due to the absence of surrounding atoms on one side of the surface. Therefore, relaxation of the excited surface complex, which precedes photon emission, can be very strong and, as a consequence, there occurs a greater Stokes shift of the maximum in the luminescence spectrum compared to the case of the bulk complexes at the same energies of exciting radiation. The concentration of the surface complexes is higher than that in the bulk. However, because of the small thickness of the surface layer, where the complexes are formed, the intensity of their luminescence is very low. Therefore, the surface luminescence can be found only in those optical-glass samples in which the bulk luminescence intensity is low or when the bulk and surface luminescence spectra are shifted with respect to each other.

Thus, we may conclude that in high-purity optical glasses, the longer wave luminescence defined by the surface centers is excited simultaneously with the excitation of the rapid broadband luminescence. The spectrum of this luminescence has a large Stokes shift and kinetic characteristics similar to those of the bulk luminescence excited within the range of the glass transmission band. The surface luminescence is sensitive to the effects of γ-irradiation and temperature and has different spectral maxima depending on the glass type. It is possible that this luminescence is determined by quasimolecular complexes formed by nonbridge oxygen atoms and an impurity ion on the glass surface.

REFERENCES

1. A. V. Amosov, Fiz. Khim. Stekla **9** (3), 29 (1983).
2. L. N. Skuya and A. N. Streletskiĭ, Izv. Akad. Nauk Latv. SSR, Ser. Fiz. Khim. Nauk, No. 4, 47 (1985).
3. A. A. Bobyshev and V. A. Radtsig, Fiz. Khim. Stekla **14** (4) (1988).
4. V. K. Leko, Fiz. Khim. Stekla **19**, 673 (1993).
5. M. A. Kasymdzhanov, S. S. Kurbanov, and P. K. Khabibullaev, Dokl. Akad. Nauk SSSR **297**, 88 (1987) [Sov. Phys. Dokl. **32**, 896 (1987)].
6. M. A. Kasymdzhanov, S. S. Kurbanov, and P. K. Khabibullaev, Dokl. Akad. Nauk SSSR **311**, 131 (1990).
7. M. A. Kasymdzhanov, P. K. Khabibullaev, and S. S. Kurbanov, Turk. J. Phys. **22**, 475 (1998).
8. S. S. Kasymova, S. S. Kurbanov, M. A. Kasymdzhanov, and P. K. Khabibullaev, in *Abstracts of the XVIII International Congress on Glass, San Francisco, 1998*, p. AB132.
9. M. Henert and B. Rauschenbakh, Fiz. Khim. Stekla **9**, 696 (1983).
10. V. Ya. Degoda, M. V. Zakharchenko, and V. M. Ochenko, Zh. Prikl. Spektrosk. **66**, 814 (1999).
11. S. G. Demos, H. B. Radousky, L. Sheehan, and M. R. Kozlowski, in *Technical Abstract Digest of the International Symposium on High-Power Lasers and Applications, Laser 2000—Photonics West, San Jose, 2000*, p. 71.

Translated by Yu. Vishnyakov

Doklady Physics, Vol. 45, No. 11, 2000, pp. 578–580. Translated from Doklady Akademii Nauk, Vol. 375, No. 2, 2000, pp. 181–187.
Original Russian Text Copyright © 2000 by Mishin.

PHYSICS

Structure of Shock Waves in Gas-Discharge Plasma

G. I. Mishin

Presented by Academician A. M. Prokhorov February 1, 2000

Received February 15, 2000

Analysis of the results of precision measurements using a ballistic setup for studying the aerodynamic drag in the case of a spherical body flying in an air gas-discharge plasma and in nonionized air was performed in [1]. Comparison of the results shows that a certain frame formed by highly excited metastable strongly interbound molecules [2, 3] arises in plasma. The frame has a clearly expressed regular structure with a density of 0.224×10^{17} cm^{-3} and a binding energy of 2.42×10^4 erg/cm^3. In this case, the distance between the bound molecules is ~10^{-6} cm and the binding energy per molecule is 10.8×10^{-13} erg, which exceeds the mean thermal kinetic energy of an air molecule at a plasma temperature of 1400 K almost by a factor of four. Owing to the strong bond between the particles in the frame, they have no translational degrees of freedom and, therefore, do not participate in creating external pressure. As a whole, the frame parameters correspond to the Rydberg state of highly excited gas particles for which the collectivization of outer electron shells occurs. We denote the concentrations of free and bound molecules as n_f and n_b, while the external static pressure is $P_f = n_f kT$ ($k = 1.38 \times 10^{-16}$ erg/K is the Boltzmann constant and T is the gas-kinetic plasma temperature).

It was found that in the gas discharge process, in both polyatomic and monoatomic gases, frames of the same standard type are formed for each gas independently of the pressure and temperature of a perfect component of plasma and the method of ionization. The initiation of the frame has an energy threshold determined by the discharge voltage across the electrodes (~1 kV for air) of a plasma producing generator.

A complicated three-wave structure of shock waves in gas-discharge plasma, which is composed of a precursor [4] including a leader [5] and a remainder wave, was discovered in 1989–1990. Anomalous parameters of shock waves in plasma were investigated in a shock wave tunnel with a cross section of 100 × 100 mm in [6]. In the tunnel air operating section 160 mm in length, a cold pulsed transverse glow discharge was formed, whose combustion duration and mean temperature were <1 ms and approximately 300 K, respectively. The density and pressure in the shock wave were detected in the central zone of the operating section located at a distance of 150 mm from the onset of the transverse electric-discharge region.

The static pressure P_f (measured by a piezoelectric sensor mounted in a plane wedge with an apex of 30°) and the free-molecule concentration n_f (measured by a Michelson optical interferometer) were registered virtually simultaneously as functions of time lapsed from the moment of entry of the shock wave into the detection region. Note that the interpretation of the results obtained in this study only became possible after the specific elastic molecular frame in the gas-discharge plasma was discovered.

In the first series of experiments, a pressure of 6 torr was maintained both before plasma generation and in the state without ionization. While generating gas-discharge plasma, the frame was formed and, consequently, $n_{b0} = 0.224 \times 10^{17}$ cm^{-3} of the free molecules in the operating section were in the bound state and the external pressure reached $P_f = 5.29$ torr at $T = 300$ K ($n_{f0} = 1.708 \times 10^{17}$ cm^{-3}). In Fig. 1, we display the characteristic pressure P_f in plasma as a function of time t and in nonionized air (curves *1* and *2*) and the density n_f (curves *3* and *4*) for the shock wave entering into the operating section with a velocity of 516 m/s.

According to the dynamic equations of plasma in [2, 3], the sonic velocity in the plasma was 665 m/s at temperature $T = 300$ K. Hence, for the measured shock front velocity 714 m/s in the plasma, the wave was transonic with a Mach number M = 1.07. From the moment of the shock wave entry into the plasma, its compression occurred, the free and bound molecules being compressed simultaneously and identically. But with increasing n_{b0}, the potential energy of the plasma elevated, while the kinetic energy of the chaotic motion decreased correspondingly; i.e., plasma cooling took place [see Fig. 1a, the dependence $T(t) = P_f/kn_f$ (*5*); the segment $t = 0$–40 μs corresponds to a leader]. Due to decreasing flow temperature, the pressure at the wave front remained virtually invariable, while the density increased by approximately 10%.

International Academy of Astronautics,
BP 1268-16, F-75766 Paris, France

1028-3358/00/4511-0578$20.00 © 2000 MAIK "Nauka/Interperiodica"

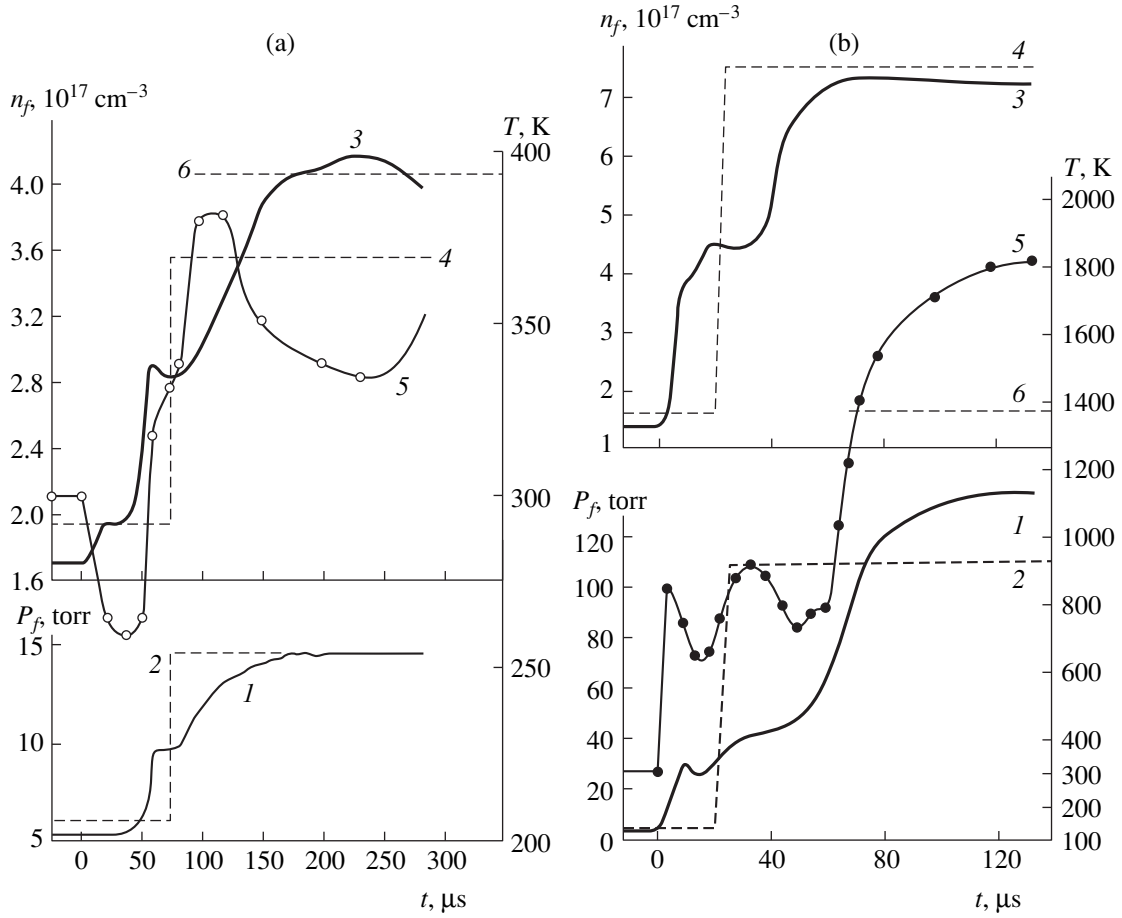

Fig. 1. Shock wave in air plasma and in nonionized air. (a) v_0 = 516 and (b) 1500 m/s; P_0 = 5 torr, T_0 = 300 K. Plasma: (*1*) $P_f(t)$, (*3*) $n_f(t)$, and (*5*) $T(t)$. Air: (*2*) $P_f(t)$, (*4*) $n_f(t)$, and (*6*) $T(t)$.

Furthermore, the nonlinear interaction between these four quantities (P_f, n_f, T, and the plasma velocity) resulted (to the time moment $t \approx 150$ μs) in the motion of the plasma flow being essentially slowed down, the plasma density and pressure increasing, and the plasma temperature proving to be ~50 K lower than that in the shock wave of nonionized air for the same velocity, 516 m/s.

Figure 1b shows the evolution of the shock wave entering into the plasma with a velocity of 1500 m/s. Before the discharge was switched on, the pressure in the operating section was maintained at 5 torr. Because the velocity of sound was 662 m/s in this case and the shock front velocity was 1825 m/s, the supersonic motion of the shock wave occurred with a Mach number M = 2.76. The time dependence $T(t)$ of plasma temperature (curve *5*) showed that, in the interval from 30 to 50 μs, a decrease in plasma temperature of 216 K occurred owing to fast slowing down of the flow and an accompanying abrupt increase in plasma density. Therefore, in spite of a significant increase in n_f, we observed only a small rise in P_f.

At $t > 50$ μs, however, the situation changed radically because of frame destruction; his occurred as a result of compression by a factor of ~3.4. The bound molecules became free, whereas the accumulated potential energy and the binding energy were returned to the flow. In this case, the plasma temperature increased to 1801 K and the pressure increased by a factor of 3.3. Since the accumulated energy corresponded to a temperature of 1365 K for the shock wave in nonionized air, the difference $\Delta T_{\text{expt}} = 436$ K in these temperatures appeared by virtue of the liberation of the binding energy. In fact, because the specific binding energy is 2.42×10^4 erg/cm^3, while the heat capacity of all the 1.61×10^{17} molecules contained in 1 cm^3 is 55.53 erg/K, the calculated value of the originated temperature difference $\Delta T_{\text{calcd}} = 436$ K coincides with that measured in the experiment.

It should be noted that the formation time for a steady precursor is on the order of 100 μs and that its thickness in the shock-wave tunnel of larger diameter is ~5.5 cm. When the directions of the wave motion and of the electron drift in the longitudinal electric field of the discharge coincided with each other, the thickness

and the velocity of the precursor were greater than in the case when the electrons drifted towards the wave [6].

In the case of frame deformation, thermal energy loss leads to a decrease in the actual experimental shock-front velocity compared to theoretical values found for a completely reversible elastic deformation. For a shock wave entering with a velocity of 516 m/s into decomposing plasma (Fig. 1a), the experimental front velocity was 714 m/s, while its theoretical value was 742 m/s; i.e., it was 3.8% higher. Thus, in this case, the irreversibility of the frame compression process was relatively small. For the shock wave with a velocity of 1500 m/s (Fig. 1b), the experimental value of the front velocity was found to be 1825 m/s, while the corresponding calculated value (ignoring the irreversibility of the deformation process) was equal to 1978 m/s; i.e., the loss (7.7%) was twice as high as in the previous example.

As a consequence of the summation of concentrations for molecules bound in the frames in the incident and reflected waves in the air gas-discharge plasma, it becomes possible to detect the interaction between the external long-wave laser radiation and the frame elements [7]. In this case, it was found that the probing radiation with wavelengths $\lambda = 0.638$ and 0.534 nm do not damp, whereas anomalously high damping (scattering) was found for laser radiation with $\lambda = 10.6$ μm, the damping coefficient being $\sim 2 \times 10^{-2}$ cm^{-1}. This can only be explained by the presence of molecules in the plasma which are bound in a Rydberg collective system owing to the joining of their external electron shells.

REFERENCES

1. A. P. Bedin and G. I. Mishin, Pis'ma Zh. Tekh. Fiz. **21** (1), 14 (1995) [Tech. Phys. Lett. **21**, 5 (1995)].
2. G. I. Mishin, Pis'ma Zh. Tekh. Fiz. **24** (11), 80 (1998) [Tech. Phys. Lett. **24**, 448 (1998)].
3. G. I. Mishin, AIAA Pap., No. 99–4906 (1999).
4. I. V. Basargin and G. I. Mishin, Pis'ma Zh. Tekh. Fiz. **15** (8), 55 (1989) [Sov. Tech. Phys. Lett. **15**, 311 (1989)].
5. A. I. Klimov and G. I. Mishin, Pis'ma Zh. Tekh. Fiz. **16** (23), 53 (1990) [Sov. Tech. Phys. Lett. **16**, 960 (1990)].
6. G. I. Mishin, A. I. Klimov, and A. Yu. Gridin, Pis'ma Zh. Tekh. Fiz. **17** (16), 84 (1991) [Sov. Tech. Phys. Lett. **17**, 602 (1991)].
7. G. I. Mishin, A. I. Klimov, and A. Yu. Gridin, Pis'ma Zh. Tekh. Fiz. **18** (6), 37 (1992) [Sov. Tech. Phys. Lett. **18**, 183 (1992)].

Translated by V. Bukhanov

Doklady Physics, Vol. 45, No. 11, 2000, pp. 581–584. Translated from Doklady Akademii Nauk, Vol. 375, No. 3, 2000, pp. 320–323.
Original Russian Text Copyright © 2000 by Yalamov, Yushkanov, Kuznetsova.

PHYSICS

Intense Evaporation of Molecular Gas from a Spherical Particle into Vacuum

Yu. I. Yalamov, A. A. Yushkanov, and I. A. Kuznetsova

Presented by Academician R. F. Ganiev March 1, 2000

Received February 15, 2000

In this paper, we solve the kinetic problem of intense evaporation of molecular gas from a spherical particle into vacuum. We explicitly find the hydrodynamic boundary conditions for intense evaporation of diatomic and triatomic gases and demonstrate their strong dependence on the Knudsen number in the range $0 < \mathrm{Kn} \le 0.1$ ($\mathrm{Kn} = \lambda/r_0$, λ is the mean free path of molecules near the evaporating surface and r_0 is the particle radius). This problem was not discussed in earlier papers [1–3]. We show that internal degrees of freedom lead to an appreciable decrease in the temperature jump and only slightly affect the gas concentration at the boundary of the Knudsen layer.

The problem of intense evaporation from a spherical particle into vacuum was discussed in [1–3]. According to numerical calculations presented in [2, 3], at $\mathrm{Kn} \ll 1$, the flow near a particle is formed in a region with size far exceeding λ. Consequently, under this condition ($\mathrm{Kn} \ll 1$), the flow is hydrodynamic and can be described by the Navier–Stokes equations with correction for kinetic boundary conditions. Relations of parameters of condensed and gas phases, i.e., the jumps of parameters in the Knudsen layer, can be determined only within the framework of kinetic theory.

A three-layer model of steady-state gas flow was proposed in [4] for the gas flowing from a pointlike source and was characterized by the Reynolds number $\mathrm{Re} \gg 1$ and the Prandtl number $\mathrm{Pr} = 3/4$. The nonequilibrium region located near the source is fitted to the region of the nonviscous supersonic gas flow described by the Euler equations through an interlayer of the viscous flow being characterized by the Mach number $\mathrm{M} \sim 1$.

In the limiting case $\mathrm{Kn} \longrightarrow 0$, the three-layer model [4] was used in [1] to obtain hydrodynamic boundary conditions corresponding to the evaporation of monoatomic and diatomic gases.

In all papers mentioned above, except [1], only monoatomic gases were considered. However, most gases are polyatomic. Therefore, it is of significant interest to study these processes for molecular gases.

It is well known that the vibrational degrees of freedom of most molecular gases are "frozen" in a wide temperature range, whereas the rotational degrees of freedom can be considered using the quasi-classical approach [5, 6].

We assume that the following parameters characterizing a particle are known: T_s is the temperature of the particle surface and n_s is the concentration of saturated vapor of the surface material at temperature T_s. Let us consider the case of a steady-state spherically symmetric expansion of the evaporated substance. Taking into account that the Knudsen number is small, we can use the Chapman–Enskog function as a distribution function within the gas. A linearized version of this function has the form [5, 7]

$$f = f_i(1 + \Phi + \Psi_i), \quad i = 1, 2, 3, \tag{1}$$

$$f_1(\mathbf{v}) = n\left(\frac{m}{2\pi kT}\right)^{3/2} \exp\left\{-\frac{m\mathbf{c}^2}{2kT}\right\},$$

$$f_i(\mathbf{v}, \nu_i) = n\left(\frac{m}{2\pi kT}\right)^{3/2} \exp\left\{-\frac{m\mathbf{c}^2}{2kT} - \nu_i^2\right\}, \quad i = 2, 3,$$

$$\Phi = -\frac{4}{3}\eta\left(\frac{du}{dr} - \frac{u}{r}\right)\frac{1}{p}\frac{m}{2kT}\left[c_r^2 - \frac{v_\theta^2 + v_\varphi^2}{2}\right],$$

$$\Psi_1 = \frac{\kappa}{c_p p}\frac{1}{T}\frac{dT}{dr}c_r\left(\frac{5}{2} - \frac{mc^2}{2kT}\right),$$

$$\Psi_i = \frac{\kappa}{c_p p}\frac{1}{T}\frac{dT}{dr}c_r\left(\frac{5+j}{2} - \frac{mc^2}{2kT} - \nu_i^2\right), \quad i = 2, 3,$$

$$\nu_2 = \sqrt{\frac{J\omega^2}{2kT}}, \quad \nu_3 = \sqrt{\frac{J_1\omega_1^2}{2kT} + \frac{J_2\omega_2^2}{2kT} + \frac{J_3\omega_3^2}{2kT}}.$$

Here, subscripts $i = 1$, 2, and 3 correspond to monoatomic, diatomic, and triatomic gases, respectively; terms Φ and Ψ_i are related to the viscosity and heat con-

Moscow Pedagogical University,
ul. Radio 10a, Moscow, 105007 Russia

1028-3358/00/4511-0581$20.00 © 2000 MAIK "Nauka/Interperiodica"

duction; j is the number of internal degrees of freedom ($j = 2$ and 3 for diatomic and triatomic gases, respectively); m is the molecular mass; J is the moment of inertia of a diatomic molecule; J_1, J_2, and J_3 are the principal moments of inertia of a triatomic molecule; $\mathbf{v}$ and $\boldsymbol{\omega} = (\omega_1, \omega_2, \omega_3)$ are the translational and angular velocities of a molecule; $\mathbf{u}$ and $\mathbf{c} = \mathbf{v} - \mathbf{u}$ are the average and thermal velocities of molecules; k is the Boltzmann constant; p, n, and T are the pressure, concentration, and temperature of the gas; η and κ are the viscosity and thermal conductivity; and c_p is the specific heat at constant pressure.

For gases, the boundary condition at surface $r = r_0$ can be written under the assumption that the Maxwell distribution f_{si} ($i = 1$, 2, and 3 for monoatomic, diatomic, and triatomic gases, respectively) with temperature equal to that of the surface (T_s) is valid for molecules emitted by the surface. For the sake of simplicity, evaporation and energy-accommodation coefficients are set equal to unity. As a result,

$$f_{s1}(\mathbf{v}) = n_s\left(\frac{m}{2\pi k T_s}\right)^{3/2}\exp\left\{-\frac{m\mathbf{v}^2}{2kT_s}\right\}, \quad v_r > 0,$$

$$f_{si}(\mathbf{v}, \nu_i) = n_s\left(\frac{m}{2\pi k T_s}\right)^{3/2}\exp\left\{-\frac{m\mathbf{v}^2}{2kT_s} - \nu_{si}^2\right\}, \quad (2)$$

$$v_r > 0, \quad i = 2, 3,$$

$$\nu_{s2} = \sqrt{\frac{J\omega^2}{2kT_s}}, \quad \nu_{s3} = \sqrt{\frac{J_1\omega_1^2}{2kT_s} + \frac{J_2\omega_2^2}{2kT_s} + \frac{J_3\omega_3^2}{2kT_s}}.$$

Taking into account viscosity η and thermal conductivity κ, we can describe the motion of an evaporated substance in the expanding flow of the system using the Navier–Stokes equations.

Far from the particle, in the region of the nonviscous flow ($\eta = 0$ and $\kappa = 0$), the system of the Navier–Stokes equations reduces to the Euler equations. The solution to these equations is known and presented in [4]. In the intermediate region situated near the sonic point $r = r_1$, the solution to the Navier–Stokes equations is expressed in terms of the modified Hankel functions [4].

At Pr = 3/4 and Kn $\ll 1$, in the interior region adjacent to the evaporating surface, the equations of fluid dynamics are transformed to [1, 4]

$$\frac{dw}{d\xi} = 2 - (k_1 a)^{2/3} - w - \frac{1}{w}, \quad (3)$$

$$\theta + \frac{\gamma - 1}{2}w^2 - \frac{\gamma + 1}{2} = 0,$$

$$\xi = \frac{x - x_1'}{a}, \quad x = \frac{r_1}{r}, \quad a = \frac{8\gamma}{3(\gamma + 1)}\eta\frac{r_1}{\dot{m}},$$

$$\beta = \frac{\gamma - 1}{\gamma + 1}, \quad x_1' = 1 + [1(1 - \beta)]^{-1/3}a^{2/3}\xi_1, \quad (4)$$

$$k_1 = \frac{4}{\gamma + 1}\xi_1^{3/2}.$$

Here, $w = u/c_1$, $\theta = T/T_1$, γ is the adiabatic index, $\dot{m}$ is the mass flux from the particle ($\dot{m} = \text{const}$), $c_1 = \sqrt{\gamma R_\mu T_1}$ and T_1 are the average values of velocity $\mathbf{u}$ and temperature T at the sonic point $r = r_1$ (i.e., at $r = r_1$, we have $w = 1$ and $\theta = 1$), and a is a small parameter ($a^{-1} \sim \text{Re}$).

A solution to Eq. (3) has the form

$$\frac{1}{R} = x_1' + k_1^{-1/3}a^{2/3} \times\left[\frac{1}{\arctan\{(k_1 a)^{-1/3}(1 - w)\}} - \frac{\pi}{2}\right] - \frac{a}{k_1}\log(1 - w). \quad (5)$$

Here, $R = 1/x = r/r_1$ is the dimensionless radius vector and the value $\xi_1 = 2.3381$ is calculated by using the condition of the asymptotic sewing of solution (3) together with that from the intermediate region where $w \sim 1$.

Expressions (3)–(5) can be used to determine the gradients of thermodynamic functions $\frac{dT}{dr}$ and $\frac{du}{dr}$ involved in distribution function (1). After the corresponding transformations are undergone, taking into account relationship $\eta = \lambda p_0(2m/\pi k T_0)^{1/2}$, distribution function (1) takes the form

$$f = f_i[b_0 + b_1 h_0^{1/2}v_r + b_2 h_0 v_r^2 + b_3 h_0^{3/2}v_r^3 + b_3 h_0^{3/2}v_r(v_\varphi^2 + v_\theta^2) + b_4 h_0(v_\varphi^2 + v_\theta^2) + 2h_0^{1/2}z_0\tau(v_r - u_0)\nu_{0i}^2],$$

$$b_0 = 1 + z_0^4 d - [(5 + j) - 2z_0^2]z_0^2\tau,$$

$$b_1 = -2z_0^3 d + [(5 + j) - 6z_0^2]z_0\tau, \quad (6)$$

$$b_2 = z_0^2 d + 6z_0^2\tau, \quad b_3 = -2z_0\tau, \quad b_4 = -z_0^2 d + 2z_0^2\tau,$$

$$d = \frac{\gamma + 1}{\gamma}\frac{1}{w_0}\left(\frac{dw}{d\xi}\right)_0, \quad \tau = \frac{\gamma^2 - 1}{2\gamma}\frac{w_0}{\theta_0}\left(\frac{dw}{d\xi}\right)_0,$$

$$R_0 = \frac{r_0}{r_1}, \quad z_0 = \sqrt{\frac{\gamma}{2}}\text{M}_0, \quad w_0 = \text{M}_0\sqrt{\frac{\gamma + 1}{2 + (\gamma - 1)\text{M}_0^2}},$$

$$a_0 = \frac{8\gamma}{3\sqrt{\pi}(\gamma + 1)}\frac{\text{Kn}}{z_0}\frac{1}{R_0}, \quad h_0 = \frac{m}{2kT_0}.$$

Here, subscript 0 corresponds to the parameters at the hydrodynamic evaporation boundary.

Let us assume the Knudsen layer to be infinitely thin. Then, it can be considered as a surface of hydrodynamic discontinuity which does not violate the conservation laws for fluxes of mass, momentum, and energy. In other words, the quantities C_{1n}, C_{2n}, and C_{3n} ($n = 1, 2, 3$) defined by the relationships

$$\int Q_{in} f_i d\Omega_i = C_{in}, \quad i = 1, 2, 3, \quad n = 1, 2, 3,$$

$$\Omega_1 = d^3v; \quad \Omega_2 = d^3v 2\nu_2 d\nu_2,$$

$$\Omega_3 = d^3v \frac{4}{\sqrt{\pi}}\nu_3^2 d\nu_3,$$

$$Q_{i1} = m, \quad Q_{i2} = mv_r, \quad i = 1, 2, 3, \tag{7}$$

$$Q_{13} = \frac{mv^2}{2}, \quad Q_{23} = \frac{mv^2}{2} + kT\nu_2^2,$$

$$Q_{33} = \frac{mv^2}{2} + kT\nu_3^2,$$

and corresponding to monoatomic, diatomic, and triatomic gases, respectively, also remain unchanged. Without solving the Boltzmann equation, these conditions provide an opportunity to establish a relationship between the surface parameters T_s and n_s and the vapor parameters T_0 and n_0 at the outer boundary of the Knudsen layer. Integration of (7) performed with allowance for (6) leads to a system of three equations with the following four unknown variables: M_0, Kn, T_0/T_s, and n_0/n_s. It is convenient to use M_0 as a free parameter. Then, dimensionless temperature T_0/T_s and concentration n_0/n_s are determined by the expressions

$$\frac{T_0}{T_s} = \frac{(4 + j)X_1}{2X_3}, \quad \frac{n_0}{n_s} = \frac{T_s}{2X_2T_0}, \tag{8}$$

whereas the Knudsen number Kn is found from the equation

$$\frac{\sqrt{\pi}}{\sqrt{2(4 + j)}}\frac{\sqrt{X_1}\sqrt{X_3}}{X_2} - 1 = 0. \tag{9}$$

The notation used above is as follows:

$$X_1 = b_0'F_0 + b_1'F_1 + b_2F_2 + b_3F_3 + b_4F_0 + b_3F_1,$$

$$X_2 = b_0'F_1 + b_1'F_2 + b_2F_3 + b_3F_4 + b_4F_1 + b_3F_2,$$

$$X_3 = b_0'\left(\frac{2 + j}{2}F_0 + F_2\right) + jz_0^2\tau F_0$$

$$+ b_1'\left(\frac{2 + j}{2}F_1 + F_3\right) - jz_0\tau F_1 + b_2\left(\frac{2 + j}{2}F_2 + F_4\right)$$

$$+ b_3\left(\frac{2 + j}{2}F_3 + F_5\right) + b_4\left(\frac{3 + j}{2}F_0 + F_2\right)$$

$$+ b_3\left(\frac{3 + j}{2}F_1 + F_3\right),$$

$$F_0 = z_0y_1 + y_2, \quad F_1 = \left(\frac{1}{2} + z_0^2\right)y_1 + z_0y_2,$$

$$F_2 = \left(\frac{3z_0}{2} + z_0^3\right)y_1 + (1 + z_0^2)y_2,$$

$$F_3 = \left(\frac{3}{4} + 3z_0^2 + z_0^4\right)y_1 + \left(\frac{5z_0}{2} + z_0^3\right)y_2,$$

$$F_4 = \left(\frac{15z_0}{4} + 5z_0^3 + z_0^5\right)y_1 + \left(2 + \frac{9z_0^2}{2} + z_0^4\right)y_2,$$

$$F_5 = \frac{1}{8}(15 + 90z_0^2 + 60z_0^4 + 8z_0^6)y_1$$

$$+ \frac{1}{8}(66z_0 + 56z_0^3 + 8z_0^5)y_2,$$

$$b_0' = b_0 + jz_0^2\tau, \quad b_1' = b_1 - jz_0\tau,$$

$$y_1 = 1 + \mathrm{erf}(z_0), \quad y_2 = \frac{\exp(-z_0^2)}{\sqrt{\pi}},$$

$$\mathrm{erf}(z_0) = \frac{2}{\sqrt{\pi}}\int_0^{z_0}\exp(-x^2)dx.$$

For monoatomic ($j = 0$), diatomic ($j = 2$), and triatomic ($j = 3$) gases, the calculated boundary values of the macroscopic parameters are presented in the table. If Kn $\longrightarrow$ 0, then the Mach number M_0, temperature T_0/T_s, and concentration n_0/n_s tend to their limiting values, which, for monoatomic ($j = 0$) and diatomic ($j = 2$) gases, agree rather satisfactorily with the results of [1] corresponding to Kn $\longrightarrow$ 0. These values are ($j = 0$) $M_0 = 0.423$, $T_0/T_s = 0.838$, and $n_0/n_s = 0.645$; ($j = 2$) $M_0 = 0.415$, $T_0/T_s = 0.913$, and $n_0/n_s = 0.661$. According to the table, for both molecular and monoatomic gases, an increase in the Knudsen number Kn leads to the growth of Mach number M_0 and to a decrease in dimensionless gas temperature T_0/T_s and concentration n_0/n_s. Consequently, temperature and concentration jumps occurring in the Knudsen layer become more pronounced.

Table 1

Kn	$j = 0$			$j = 2$			$j = 3$		
	M_0	T_0/T_s	n_0/n_s	M_0	T_0/T_s	n_0/n_s	M_0	T_0/T_s	n_0/n_s
Kn $\longrightarrow$ 0	0.386	0.911	0.664	0.404	0.942	0.663	0.410	0.950	0.663
0.0025	0.410	0.903	0.648	0.430	0.936	0.647	0.437	0.945	0.646
0.005	0.425	0.897	0.638	0.447	0.932	0.637	0.454	0.941	0.636
0.01	0.450	0.888	0.624	0.477	0.924	0.620	0.484	0.935	0.619
0.02	0.500	0.868	0.597	0.528	0.911	0.593	0.437	0.923	0.590
0.03	0.550	0.847	0.573	0.577	0.897	0.568	0.586	0.911	0.560
0.04	0.590	0.829	0.555	0.622	0.884	0.547	0.632	0.899	0.545
0.05	0.632	0.811	0.537	0.665	0.871	0.529	0.675	0.888	0.526
0.06	0.670	0.794	0.522	0.703	0.858	0.513	0.713	0.877	0.510
0.07	0.700	0.780	0.511	0.735	0.848	0.501	0.745	0.868	0.498
0.08	0.732	0.764	0.499	0.762	0.838	0.491	0.771	0.860	0.488
0.09	0.755	0.752	0.491	0.782	0.830	0.484	0.791	0.853	0.481
0.1	0.774	0.742	0.486	0.798	0.824	0.479	0.806	0.848	0.476

Comparison of the results obtained at the same values of the Knudsen number for monoatomic and molecular gases leads to the conclusion that excitation of the rotational degrees of freedom produces a pronounced effect on the boundary values of the gas temperature: T_0/T_s increases (its jump becomes smaller) and only slightly affects concentration n_0/n_s. At Kn = 0.1, the largest temperature change is as high as 11 and 14% at the transition from monoatomic gas to diatomic and triatomic gases, respectively.

REFERENCES

1. R. H. Edwards and R. L. Collins, in *Proceedings of the International Symposium on Rarefied Gas Dynamics* (Academic, New York, 1969), Vol. 2, p. 1489.
2. Y. Sone and H. Sugimoto, Phys. Fluids A **5**, 1491 (1993).
3. N. M. Bulgakova, M. Yu. Plotnikov, and A. K. Rebrov, Izv. Akad. Nauk, Mekh. Zhidk. Gaza, No. 6, 137 (1997).
4. A. Sakurai, Q. J. Mech. Appl. Math. **11**, 274 (1958).
5. V. M. Zhdanov and M. Ya. Alievskiĭ, *Transport and Relaxation Processes in Molecular Gases* (Nauka, Moscow, 1989).
6. L. D. Landau and E. M. Lifshitz, *Statistical Physics* (Nauka, Moscow, 1976; Pergamon, Oxford, 1980).
7. A. V. Latyshev and A. A. Yushkanov, Izv. Akad. Nauk, Mekh. Zhidk. Gaza, No. 5, 182 (1998).

Translated by Yu. Verevochkin

Doklady Physics, Vol. 45, No. 11, 2000, pp. 585–587. Translated from Doklady Akademii Nauk, Vol. 375, No. 1, 2000, pp. 29–31.
Original Russian Text Copyright © 2000 by Kechek'yan, Bazhenov.

TECHNICAL PHYSICS

Mechanical Self-Oscillations Driven by Extension of a Polymer Film

A. S. Kechek'yan* and S. L. Bazhenov**

Presented by Academician N. F. Bakeev December 21, 1999

Received February 15, 2000

The effect of jumplike growth of the neck in a polyethylene terephthalate (PETP) film accompanied by oscillations of the load and temperature at the neck front was reported in [1]. The neck jumps are interpreted in terms of the heat release at the neck front giving rise to local heating of the polymer, which results in an increase in velocity. This results in still more heat releases, and the neck velocity increases in an avalanche-like manner. Drastic elongation of the sample leads to a decrease in the load and a decrease in the heat release. The transient zone begins to cool down, causing a decrease in the neck growth rate. The growth rate decreases until the neck becomes nearly immobile. After that, the stress again begins to increase. When the stress reaches critical value, the jump of the neck front is repeated.

The aim of this paper is to find the criterion determining the generation of self-oscillations which accompany neck growth in a polymer film.

Film samples of commercial amorphous PETP 110 μm thick, 10 mm wide, and 40 mm long were used in the experiments. The extension of the samples studied was performed in air using the AGS-10 kNG testing apparatus supplied by the Shimazu company.

Typical stress dependence of the elongation is shown in Fig. 1. After attaining the yield stress, the load exhibits 3–4 oscillations. Then, a steady-state flow of the polymer is established under constant tensile stress. At a certain moment, periodic oscillations of the load appear on the diagram. The amplitude of oscillations is 1/5–1/4 that of the tensile stress.

The photograph illustrating neck formation is presented in Fig. 2. At the initial steady-state stage of the growth, the neck is transparent. This region is darker at the black background. At the stage of self-oscillations, alternation of dark and light (turbid) stripes is observed.

* *Institute of Synthetic Polymeric Materials, Russian Academy of Sciences, Profsoyuznaya ul. 70, Moscow, 117393 Russia*

** *Semenov Institute of Chemical Physics, Russian Academy of Sciences, ul. Kosygina 4, Moscow, 117977 Russia*

The elastic elongation of the sample is [2]

$$\Delta L_e = \frac{L_1\sigma}{E_1} + \frac{L_2\sigma_2}{E_2}, \quad (1)$$

where L is the length, E is the elasticity modulus, σ is the stress, and subscripts 1 and 2 denote the nonoriented part of the sample and the neck, respectively (Fig. 3). The stress in the neck is $\sigma_2 = S_1\sigma/S_2 = \lambda\sigma$, where λ is the degree of tension in the neck. The increment of the sample length during time dt is equal to $dL = Vdt$, where V is the extension rate. If the neck growth rate equals u, then the increment of the plastic strain in time dt is $dL_p = (\lambda - 1)u\,dt$. Hence, we obtain

$$\frac{d\sigma}{dt} = \frac{V - (\lambda - 1)u}{D}, \quad (2)$$

where $D = L_1/E_1 + \lambda L_2/E_2$ is the compliance of the sample. The plastic flow in the transient zone requires work equal to the force multiplied by the magnitude of the plastic elongation $(\lambda - 1)\sigma S_1 u\,dt$. Assuming α to be the

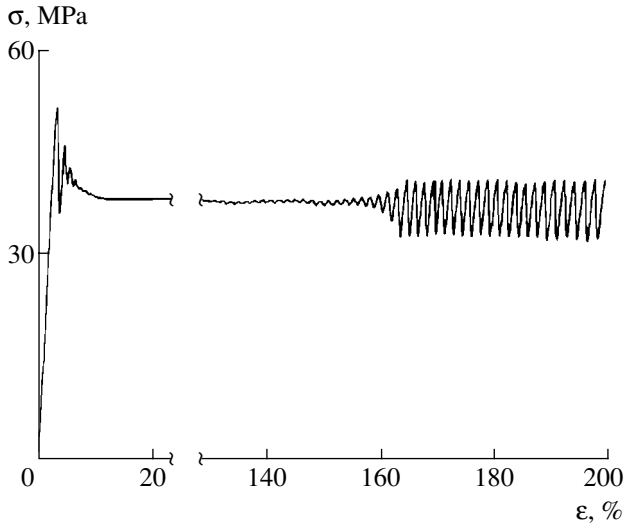

Fig. 1. Tensile stress versus strain for the PETP film 0.11 mm thick.

1028-3358/00/4511-0585$20.00 © 2000 MAIK "Nauka/Interperiodica"

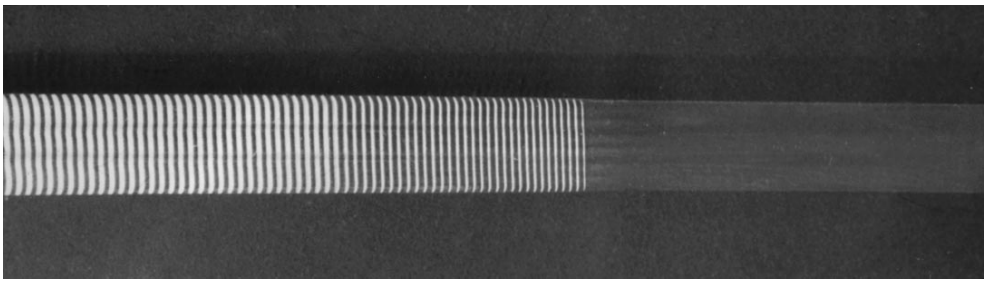

Fig. 2. Photograph of the sample after its extension. The neck grew from right to left.

fraction of work spent to heat release in the transient zone, we have

$$dQ_1 = \alpha(\lambda - 1)\sigma S_1 u dt. \quad (3)$$

The released heat causes an increase in temperature in the zone, and a certain part of it is dissipated. The heat losses are caused by the thermal conductivity of the polymer and heat transfer to the surrounding medium. Assuming that the sample cooling is convective, we find that the heat transfer to the outer medium is

$$dQ_2 = \beta(T - T_0)w d dt, \quad (4)$$

where β is the heat exchange coefficient, w is the sample width, d is the length of the transient zone, and T_0 is the temperature of the surrounding medium. The heat transferred from the transient zone by the heated polymer can be written as

$$dQ_3 = c\rho S_1 u(T - T_0)dt, \quad (5)$$

where c is the specific heat and ρ is the polymer density. The heat spent to the zone heating is equal to $dQ_1 - dQ_2 - dQ_3$, and we get

$$\frac{dT}{dt} = \frac{\alpha(\lambda - 1)\sigma u}{\rho c d} - \frac{u(T - T_0)}{d} - \beta\frac{(T - T_0)}{\rho c h}, \quad (6)$$

where T is the current temperature of the zone. Analyzing the stability of the neck growth, note that Eqs. (2) and (6) have a trivial solution, which corresponds to the constant neck growth rate:

$$u_s = \frac{V}{\lambda - 1}, \quad (7)$$

$$\frac{\alpha(\lambda - 1)\sigma_s u_s}{\rho c d} - \frac{u_s \Delta T}{d} - \frac{\beta \Delta T}{\rho c h} = 0, \quad (8)$$

where $\Delta T = T_s - T_0$ is the magnitude of the zone heating before instability arises and u_s and σ_s are the growth rate and the stress corresponding to the steady-state flow in the neck.

We linearize Eqs. (2)–(6). Let us assume that the neck moves with constant velocity (7). Then, we change the variables involved: $T = T_s + \theta$ and $\sigma = \sigma_s + S$, where θ and S are the deviations of the temperature and stress from their values corresponding to the steady-state transition to the neck. We should take into account that the neck growth rate depends on the temperature and stress. Performing the series expansion of the growth rate, we retain only linear terms:

$$u = u_s + \partial_T u\theta + \partial_\sigma u S,$$

where $\partial_T u = \partial u/\partial T$ and $\partial_\sigma u = \partial u/\partial\sigma$ are the partial derivatives of the growth rate with respect to temperature and stress, respectively. We assume that the values of θ and σ are small in comparison to σ_s and S. Retaining only the linear terms in the expansion, we obtain a system of two linear differential equations with constant coefficients:

$$\frac{dS}{dt} = -\frac{(\lambda - 1)\partial_\sigma u}{D} S - \frac{(\lambda - 1)\partial_T u}{D}\theta, \quad (9)$$

$$\frac{d\theta}{dt} = \left\{\frac{\beta \Delta T \partial_\sigma u}{\rho c h u_s} + \frac{\alpha(\lambda - 1)u_s}{\rho c d}\right\} S + \left\{\frac{\beta \Delta T \partial_T u}{\rho c h u_s} - \frac{\alpha(\lambda - 1)u_s \sigma_s}{\rho c d \Delta T}\right\}\theta. \quad (10)$$

The sum of the two exponentials is the solution to this system [3]. The initial fluctuations in stress and temperature infinitely increase if the argument of one of the

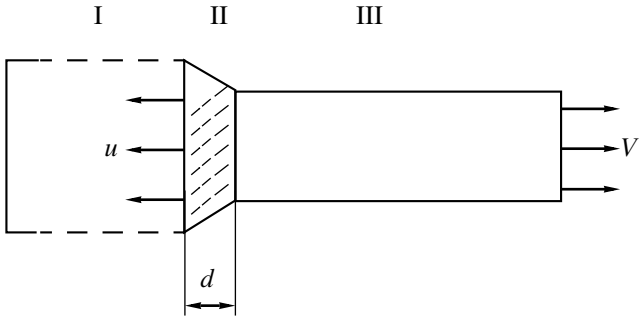

Fig. 3. Model: I. nonoriented part of the sample; II. transient zone; III. neck. V is the extension rate and u is the neck front velocity.

exponentials exceeds zero. Note that the exponents are positive if the following inequality is met:

$$-\frac{\alpha\beta(\lambda-1)\sigma_s}{\rho c(u_s\rho ch+\beta d)}\frac{d\sigma}{dT}-\frac{u_s\rho ch+\beta d}{\rho cdh\partial_\sigma u}-\frac{\lambda-1}{D}>0. \quad (11)$$

In (11), only the first term is positive (derivative $\frac{d\sigma}{dT}$ is negative); the second and third terms are negative. Therefore, to meet the inequality, the first term should be large and the second and third terms should be small. As a consequence, for the existence of self-oscillations, the derivatives $\frac{d\sigma}{dT}$ and $\partial_\sigma u$ should be large. These conditions are fulfilled at temperatures near the glass transition temperature T_g of the polymer. If the temperature of the outer medium is lower than T_g, it is necessary to take into account the heating of the transient zone. The extension rate must be sufficiently high for the temperature of the transient zone to be raised to the glass transition point. If the PETP film is stretched under room temperature, this condition is absolutely necessary for the generation of self-oscillations.

In addition, to meet criterion (11), compliance D of the sample must be high. Since the compliance is proportional to the sample length, the sample must be sufficiently long. Analyzing the effect of compliance, we can find the ratio of the first and third terms of inequality (11). The third term can be neglected, if it is much less than the first one. For the values $\frac{d\sigma}{dT}$, E, α, σ_s, λ, c [1], and ρ typical of PETP [4], inequality (11) reduces to $L \gg 50h$ [1]. For the film thickness $h = 0.11$ mm, inequality (11) is met, if the sample is much longer than 5 mm. Consequently, for sample lengths much larger than 5 mm, the effect of compliance influence can be neglected.

It is easier to meet criterion (11) when the transient zone has small length d and the sample thickness is large. Finally, the high degree λ of polymer stretching in the neck favors the validity of (11). In PETP, λ is equal to 5.5–6.0 [1, 5]. Such a value is higher than those obtained for most other polymers. This is probably why it was in PETP that the self-oscillations were observed for the first time. The specific heat and density are approximately equal for most polymers at normal temperatures, and these parameters cannot essentially affect the generation of self-oscillations.

The left side f of criterion (11) is plotted in Fig. 4 as a function of neck growth rate u. For low and very high rates, function $f(u)$ is negative and the neck motion is stable. The u range corresponding to $f > 0$ determines the existence domain for self-oscillations.

A change in heat transfer coefficient β shifts the curve in Fig. 4 along the u-axis. Function f remains unchanged if coefficient β and the neck growth rate change by the same factor. Consequently, high heat transfer β (in the course of extension, e.g., in a liquid) does not rule out the generation of self-oscillations, but only at very high extension rates. The decrease in compliance shifts function f downward along the vertical axis. For a certain value of compliance, function f turns out to be negative at any extension rate. Consequently, there exists a compliance threshold below which the self-oscillations cannot exist.

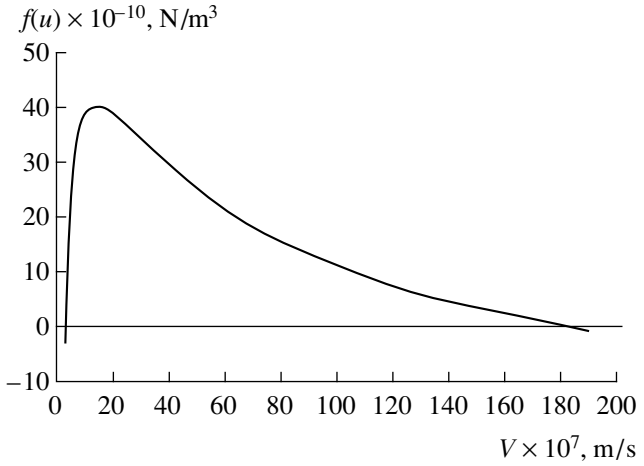

Fig. 4. The left side of inequality (11) versus neck growth rate.

Self-oscillations are caused by the thermal instability of the neck growth. Several conditions favor the generation of self-oscillations: first of all, a high value of $\frac{d\sigma}{dT}$ observed in the vicinity of the glass transition occurring in the polymer; second, a high sample compliance D (in our case, this condition is met if the sample length far exceeds 5 mm); third, a small length of the operating zone; and, finally, a high degree of polymer stretching in the neck. Note also the existence of the lower and upper bounds for the extension rate between which the self-oscillations exist.

REFERENCES

1. A. S. Kechek'yan, G. P. Andrianova, and V. A. Kargin, Vysokomol. Soedin., Ser. A **12**, 2424 (1970).
2. G. I. Barenblatt, Izv. Akad. Nauk SSSR, Mekh. Tverd. Tela, No. 5, 121 (1970).
3. A. S. Pontryagin, *Ordinary Differential Equations* (Nauka, Moscow, 1974).
4. *Physical Quantities. Handbook*, Ed. by I. S. Grigor'ev and E. Z. Meilikhov (Énergoizdat, Moscow, 1991).
5. Y. K. Godovsky, *Thermophysical Properties of Polymers* (Springer-Verlag, Berlin, 1993).

Translated by T. Galkina

Doklady Physics, Vol. 45, No. 11, 2000, pp. 588–591. Translated from Doklady Akademii Nauk, Vol. 375, No. 2, 2000, pp. 184–187.
Original Russian Text Copyright © 2000 by Vasilenok, Kablov, Bokshteĭn, Razumovskiĭ.

TECHNICAL PHYSICS

Diffusion of Carbon along Grain Boundaries in Niobium

L. B. Vasilenok*, Corresponding Member of the RAS E. N. Kablov*, B. S. Bokshteĭn, and I. M. Razumovskiĭ***

Received March 13, 2000

INTRODUCTION

The accelerated diffusion of impurities along grain boundaries has been observed in a number of transition metals: Co and Fe in α-Zr [1, 2], Co in α-Ti [3], Co and Ni in Nb [4, 5], and C in α-Fe [6]. Note, however, that the data on the grain-boundary diffusion of carbon, which is the most suitable element for the study of impurity diffusion in these metals, are incomplete: the results reported in [6] exhibit a significant spread and characterize the grain-boundary diffusion in α-Fe only at three temperature values (648, 686, and 739 K). These data do not allow us to estimate either the activation energy of the grain-boundary diffusion of carbon or the value of the preexponential factor. The main method used to measure the diffusion penetrability of grain boundaries is based on the plotting of profiles of diffusion-driven penetrations using layer-by-layer radiometric analysis. Hence, the main difficulty in the measurement of the carbon diffusion in α-Fe seems to be related to the very low solubility of carbon in the bulk of α-Fe. The diffusion "wedges" arising after annealing in the vicinity of grain boundaries are very narrow, and the concentration of the diffusing element at the boundaries determined after removing the layer of the bulk diffusion is low. Therefore, it is very difficult to perform measurements at the "tails" of the concentration profiles, which characterize the diffusion along the grain boundaries.

From this standpoint, Nb is the most suitable object for experimental study of carbon grain-boundary diffusion, since carbon solubility seems to be somewhat higher in Nb than in α-Fe. However, in the study of carbon diffusion in niobium, another difficulty arises which severely complicates the interpretation of the experimental profiles of the diffusion-driven penetration. The difficulty is that the grain boundaries in pure Nb are characterized by a high mobility [4, 5] and the migration of boundaries is observed under diffusion annealings; this migration cannot even be suppressed by preliminary high-temperature annealings. The presence of mobile grain boundaries in a polycrystal during the course of diffusion annealing can strongly affect the shape of the measured concentration profiles. Thus, the correct interpretation of these profiles becomes almost impossible. This problem was solved when the model of diffusion along the moving grain boundary was developed [7, 8] alongside a procedure based on this model, which provides an opportunity to process the concentration profiles in a polycrystal with two types of boundaries, mobile and immobile [4]. The developed models and techniques were successfully applied to the study of Co and Ni diffusion in niobium by the method of radiometric layer-by-layer analysis [4, 5].

In this paper, the diffusion of carbon along grain boundaries in Nb was studied using radioisotope techniques. Taking into account the importance of identifying the moving grain boundaries in the structure of the polycrystals, we made an attempt to reveal them using high-resolution autoradiography.

EXPERIMENTAL TECHNIQUE AND THE PROCESSING OF MEASURED PROFILES

We used high-purity Nb samples. The impurity content in Nb and the sample preparation technique are described in [4, 5].

The carbon diffusion in Nb was studied by the following technique. The donor samples saturated by the radioactive carbon served as the sources of β radiation (with energy E_{max} = 156 keV) of the radioactive carbon ^{14}C. The saturation was performed by the application of a special paste containing ^{14}C (the total radioactivity 3.7×10^9 Bq) onto the donor samples and by subsequent annealing. For the diffusion annealings, a pair of Nb samples was packed together with a donor in a such way that an air space remained between them. The diffusion pairs prepared in such a manner were wrapped in titanium foil and placed in a vacuum-sealed silica ampoule, which was then annealed at a given temperature. After diffusion annealing, a layer approximately 1 mm thick was removed from the Nb sample surface, but not from the flat operating part.

* *All-Russia Institute of Aviation Materials, ul. Radio 17, Moscow, 105007 Russia*

** *Moscow Institute of Steel and Alloys, Leninskiĭ pr. 4, Moscow, 117936 Russia*

1028-3358/00/4511-0588$20.00 © 2000 MAIK "Nauka/Interperiodica"

The profiles of the diffusion penetration of the radioactive isotope ^{14}C into the Nb polycrystals after diffusion annealing were measured using the method of radiometric layer-by-layer analysis. The activity of the removed layers was measured using a liquid-based radioactivity sensor.

The obtained profiles were interpreted within the framework of the generalized Fisher model [7, 8]. This model predicts that under diffusion in a polycrystal with immobile and mobile grain boundaries, the grain-boundary region of the concentration curve consists of two parts: the tail of the curve usually related to the diffusion along the stationary boundaries and the intermediate region between the zone of the bulk diffusion and the tail, which characterizes the diffusion along the mobile grain boundaries. The whole profile of the grain-boundary diffusion in a polycrystal with immobile and mobile grain boundaries was approximated by the function [4]

$$\ln c = \ln[q_1 \exp(-q_2 y^{6/5}) + q_3 \exp(-q_4 y)], \quad (1)$$

where c is the layer concentration, y is the penetration depth, and q_i are the fitting coefficients. The coefficient $q_2 = -\dfrac{\partial \ln c}{\partial y^{6/5}}$ was used for calculating the diffusion penetrability of the stationary boundaries $P \equiv sD'\delta$ (here, s is the coefficient of the diffusant equilibrium segregation at the grain boundaries, D' is the coefficient of the grain-boundary diffusion, and δ is the diffusion width of the grain boundaries):

$$P = 1.308\left(\frac{D}{t}\right)^{1/2} q_2^{-5/3}. \quad (2)$$

Here, D is the coefficient of the bulk diffusion and t is the duration of diffusion annealing. It is obvious that formula (2) coincides with the conventional expression for calculating the diffusion penetrability of grain boundaries in a polycrystal with immobile boundaries [9].

In order to calculate the diffusion penetrability of grain boundaries, it is necessary to know the diffusion coefficients D in the bulk. For calculating D, we used the Le Claire expression [10], which was obtained as a result of averaging literature data on the bulk diffusion of carbon in Nb:

$$D = 1 \times 10^{-6} \exp\left(-\frac{141.92 \text{ kJ mol}^{-1}}{RT}\right) \text{m}^2 \text{ s}^{-1}. \quad (3)$$

RESULTS AND DISCUSSION

In the autoradiogram (Fig. 1), the pattern of the accelerated diffusion of carbon along the grain boundaries in Nb is clearly seen; this pattern reveals the presence of two kinds of grain boundaries in the structure, mobile and stationary. The moving boundary leaves a trace of radioactive atoms behind itself in the bulk. In the autoradiogram, it looks like a wide dark strip strewn with silver crystals. The immobile boundary is significantly narrower, and its autographic width is defined by the size of the developed emulsion crystals situated above it.

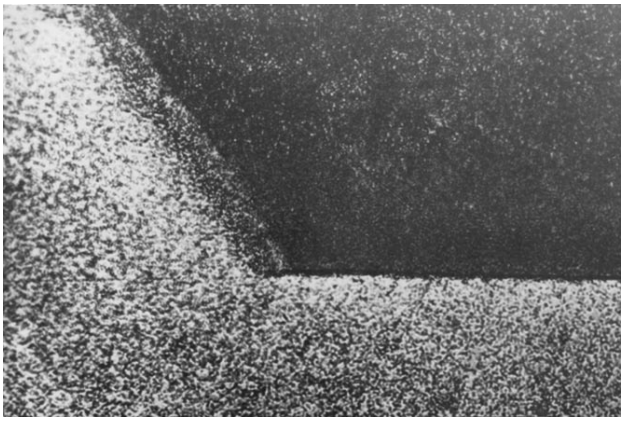

Fig. 1. Accelerated diffusion of ^{14}C along the immobile and mobile grain boundaries in niobium (autoradiogram, ×500).

The experimental profiles of the ^{14}C diffusion-driven penetration into the Nb polycrystals and the model curves approximating them (formula (1)) in the zone of the boundary diffusion are shown in Fig. 2 using the conventional coordinates $\log c - y^{6/5}$. The experimental profiles in the zone of grain-boundary diffusion consist of two regions. The first, a region of large penetration depths which is well linearized in these coordinates, characterizes the diffusion along the stationary (immobile) grain boundaries. The second is an intermediate region at smaller depths of penetration which characterizes the diffusion along the mobile grain boundaries.

The separation of the regions on the concentration profiles, which characterize the diffusion of carbon along the immobile grain boundaries, allows us to calculate the diffusion penetrability P of these boundaries using formula (2). The calculated values of P, together with the parameters of the boundary diffusion regime $\alpha = s\delta/2(Dt)^{1/2}$ and $\beta = P/[2Dx(Dt)^{1/2}]$, are given in the table. The Arrhenius equation obtained according to the

Parameters of the grain-boundary diffusion of carbon in niobium

T, K	t, 10^3 s	D, m^2/s	P, m^3/s	α*	β
951	3.6	1.6×10^{-14}	1.9×10^{-18}	3×10^{-5}	8
893	4.5	5.0×10^{-15}	7.0×10^{-19}	5×10^{-5}	15
878	3.9	3.6×10^{-15}	5.5×10^{-19}	7×10^{-5}	20
855	7.8	2.1×10^{-15}	2.4×10^{-19}	6×10^{-5}	14
803	6.6	5.9×10^{-16}	6.2×10^{-20}	1×10^{-4}	26

* Calculations were carried out under the assumption that $s \sim 1$.

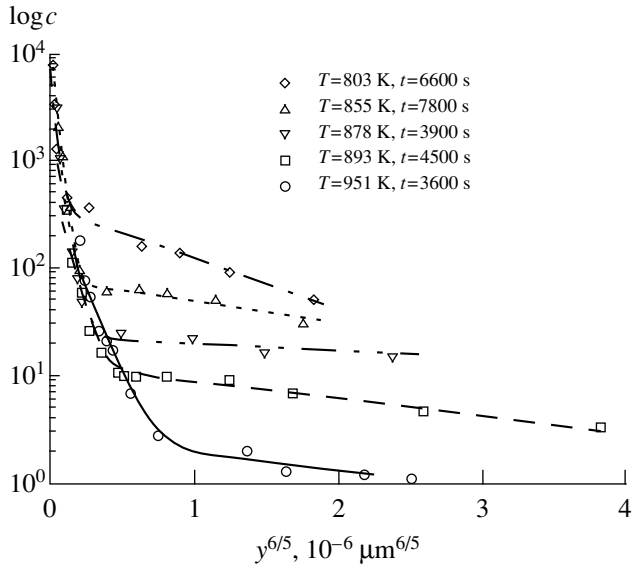

Fig. 2. Profiles of the diffusion-driven penetration of ^{14}C into niobium polycrystals at various temperatures.

temperature dependence of P for the grain-boundary diffusion of carbon in Nb has the form

$$P = (3.6^{+6.3}_{-2.3}) \times 10^{-6} \times \exp\left(-\frac{149.6 \pm 7.3 \text{ kJ mol}^{-1}}{RT}\right) \text{m}^3 \text{ s}^{-1}. \quad (4)$$

A conventional regime predicted by a mathematical model of the diffusion along the grain boundaries (regime B_2) occurs when $\beta \gg 1$ and $\alpha \ll 1$. In fact, for the onset of the B_2 regime, it is sufficient that conditions $\beta > 10$ and $\alpha < 0.1$ be met.

No difficulties occur in evaluating parameter β. Its values are given in the table. Evidently, condition $\beta > 10$ was met almost at all temperatures.

Difficulties arise when evaluating parameter α. In order to calculate parameter α, we must know the values of the equilibrium segregation coefficients s for carbon at the grain boundaries in Nb at low temperatures. Usually the values of s are estimated based on the data on the solubility of the diffusant in the volume of a solvent, i.e., the object under study. However, the solubility of carbon in Nb at low temperatures is also unknown. Therefore, it is difficult to implement such an approach in this case.

We specified the values of parameter α for the diffusion of carbon in Nb in the table; these values were calculated under the obviously untrue assumption that $s \sim 1$. It is clear from the table that the condition $\alpha < 0.1$ will not be met if $s \sim 10^5$. Now, we estimate the possibility that such a regime, unfavorable to our experiments, will occur.

Let us take an experimental value for the diffusion penetrability of the grain boundaries by diffusing C into Nb at $T = 900$ K: $P = 7 \times 10^{-19}$ m^3/s ($P \equiv sD'\delta$). According to the Fisher model, we assume $\delta = 5 \times 10^{-10}$ m. Then, we get $sD' = 1.4 \times 10^{-9}$ m^2/s for $T = 900$ K. Taking $s \sim 10^5$, we obtain $D' = 1.4 \times 10^{-14}$ m^2/s. Now, we compare the value obtained for D' with the diffusion coefficient for carbon in the Nb bulk at 900 K: $D = 5.8 \times 10^{-15}$ m^2/s. Assuming that $s \sim 10^5$, we obtain the values of the grain-boundary diffusion coefficients coinciding in order of magnitude with the diffusion penetrability in the bulk. However, this does not agree with our experimental data: the autoradiograms clearly show that the diffusion penetrability of grain boundaries in Nb for the diffusion of carbon is considerably higher than that in the bulk.

Thus, our suggestion that $s \sim 10^5$ is erroneous. In fact, condition $s \ll 10^5$ should be met. For example, assuming that $s \sim 10^3 \ll 10^5$, we get $D' = 1 \times 10^{-12}$ m^2/s. For such a value of the coefficients of the carbon boundary diffusion in Nb, condition $D' \gg D$ is met and both the conditions determining the onset of the B_2 regime arise ($\alpha < 0.1$, $\beta > 10$).

In conclusion, consider the relationship between the diffusion penetrabilities in the bulk and at the grain boundaries in Nb for the self-diffusion and diffusion of impurities. We choose for the estimates the specific temperature value $T = 900$ K. Calculating P to the self-diffusion along grain boundaries in Nb using the empirical Gust relationship [11], we obtain $P_{Nd} = (D'\delta)_{Nb} = 1.5 \times 10^{-27}$ m^3/s. Assuming that $\delta = 5 \times 10^{-10}$ m, we obtain the value $D' = 3 \times 10^{-18}$ m^2/s for the coefficient of the grain-boundary self-diffusion. In the case of volume self-diffusion in Nb, we calculate the corresponding diffusion coefficient using the formula [4]

$$D = 5.3 \times 10^{-5} \exp\left(-\frac{391.6 \text{ kJ mol}^{-1}}{RT}\right) \text{m}^2 \text{ s}^{-1}. \quad (5)$$

Hence, we obtain $D = 9.9 \times 10^{-28}$ m^2/s. In the case of self-diffusion, the ratio of the diffusion penetrability of the grain boundaries and the bulk at 900 K in Nb is $D'/D = 3 \times 10^9$. Taking into account that the temperature of 900 K is very low for diffusion in Nb ($T/T_m = 0.35$), the relationship obtained for the diffusion penetrability of the grain boundaries and for the bulk in Nb looks reasonable.

The similar relationships for the impurity diffusion in Nb at 900 K are

Co in Nb: $s \sim 10^2$, $\delta = 5 \times 10^{-10}$ m [4], and $D'/D = 4 \times 10^6$;

C in Nb: $s \sim 10^3$, $\delta = 5 \times 10^{-10}$ m, and $D'/D = 3 \times 10^2$.

We found that, on the one hand, the bulk and boundary diffusion of carbon in Nb differ by only two orders of magnitude. In contrast to most other systems, in the case of the carbon diffusion in Nb, this difference is also retained at high temperatures, since the activation

energies for the bulk and grain-boundary diffusion are close to each other.

On the other hand, in the sequence of diffusants Nb–Co(Ni)–C, a sharp decrease in the magnitude of the ratio D'/D is observed at low temperatures; it can be as large as seven orders of magnitude. The most probable cause of the observed effect is the change of the diffusion mechanism, which manifests itself most clearly in the diffusion of carbon in Nb.

REFERENCES

1. K. Vieregge, R. Willecke, and Chr. Herzig, J. Phys. C **51**, 1 (1990).
2. K. Vieregge and Chr. Herzig, J. Nucl. Mater. **175**, 29 (1990).
3. Chr. Herzig, R. Willecke, and K. Vieregge, Philos. Mag. A **63**, 949 (1991).
4. M. Koppers, Yu. Mishin, and Chr. Herzig, Acta Metall. Mater. **42**, 2859 (1994).
5. I. Razumovskii, Yu. Mishin, and Chr. Herzig, Mater. Sci. Eng. **212**, 45 (1996).
6. E. Budke, Chr. Herzig, and H. Wever, Phys. Status Solidi A **127**, 87 (1991).
7. Yu. Mishin and I. Razumovskiĭ, Poverkhnost' **7**, 5 (1983).
8. Yu. Mishin and I. Razumovskii, Acta Metall. Mater. **40**, 839 (1992).
9. I. Kaur, Y. Mishin, and W. Gust, *Fundamentals of Grain and Interphase Boundary Diffusion* (Wiley, Chichester, 1995).
10. A. D. le Claire, in *Landolt-Bornstein. New Series* (Springer-Verlag, Berlin, 1990), Vol. 3 (26), p. 626.
11. W. Gust, S. Mayer, A. Bogel, and B. Predel, J. Phys. C **46**, 537 (1985).

Translated by T. Galkina

Doklady Physics, Vol. 45, No. 11, 2000, pp. 592–595. Translated from Doklady Akademii Nauk, Vol. 375, No. 3, 2000, pp. 324–327.
Original Russian Text Copyright © 2000 by Aleksandrov, Kuznetsov.

TECHNICAL PHYSICS

Modeling of Liquid Motion in a Vertical Tube with Local Heat Release

E. N. Aleksandrov* and N. M. Kuznetsov**

Presented by Academician A. E. Shilov February 18, 2000

Received February 18, 2000

To analyze the effect on the tube walls and environment of a pressure pulse $P(t)$, generated in a vertical tube filled with a liquid as a result of the combustion of fuel in the bottom portion of the tube, we need to know the pulse duration and shape. The pressure rise induced by the combustion is followed by a pressure drop due to the expansion of the combustion products. This process is of practical interest, for example, as applied to oil wells, where the expansion of combustion products is driven by the compression and displacement of aqueous salt solutions (henceforth called water for brevity) occupying the well space above the combustion products. Some results of numerical simulations for processes of this type were reported in [1]. However, the presentation in [1] did not include any formulas or equations explaining the approximations employed and the dependence of the results on basic system parameters.

In what follows, we analyze the pressure pulse as depending on the combustion duration and other parameters (with water treated both as a compressible and incompressible fluid). The filtration of the combustion products and the formation of cracks in the ambient medium are not taken into account.

1. STATEMENT OF THE PROBLEM

At the initial moment, a quiescent combustible mixture fills a bottom tube segment of height L. A liquid (water) column (LC) fills the tube up to a point located at a certain distance from its top end. A cylindrical combustion wave propagating in the radial direction is simultaneously initiated on the tube axis. As the pressure increases in the burning mixture, the combustion products displace the water like a piston, giving rise to a compression wave propagating along the tube upwards. The qualitative and quantitative characteristics of the motion depend on the ratio of the combustion time τ to the time τ_w required for a hydrodynamic disturbance to propagate from the burning center to the upper LC boundary. Depending on the ratio τ/τ_w, the compression wave either transforms into a shock wave (the faster this occurs, the smaller the τ/τ_w ratio is) or retains a smooth pressure profile over the entire distance traveled up to the upper LC boundary. In the limit of $\tau/\tau_w \gg 1$, water can be treated as an incompressible fluid and the LC motion can be treated as that of a rigid rod.

At the pressures $P \le 1$ GPa considered below, the isentropic dependence of pressure on water density ρ is described by the Tait equation [2]:

$$P = B(\sigma^n - 1),\ B = 3047\ \text{atm},\ n = 7.15,\ \sigma \equiv \frac{\rho}{\rho_1}, \quad (1)$$

where ρ_1 is the initial water density. The values of B and n given above are characteristic of sea water with a salt concentration of 0.7 mol/l at an initial temperature of 20°C. Since these parameters weakly depend on the salt concentration (see sonic velocities for saline water in [3]) and on the temperature change along the tube, these values can be approximated for other initial temperatures and higher solution concentrations used in practice. Within the pressure range indicated above, shock-wave compression is close to an isentropic process and the Hugoniot adiabat for the water is given by Eq. (1).

In a rigorous formulation of the problem, the solution for $P(t)$ can only be obtained by numerical methods. However, the basic trends in the fluid dynamics of the process preceding to the formation of a rarefaction wave at the upper LC boundary can be determined analytically with a dependence on the parameters of the problem, thus reducing the calculations to a minimum. Below, we use the following basic approximations.

1. The gas bubble–LC interface (henceforth referred to as the contact surface) is assumed to be planar.

* *Émanuel Institute of Biochemical Physics, Russian Academy of Sciences, ul. Kosygina 4, Moscow, 117977 Russia*

** *Semenov Institute of Chemical Physics, Russian Academy of Sciences, ul. Kosygina 4, Moscow, 117977 Russia*

1028-3358/00/4511-0592$20.00 © 2000 MAIK “Nauka/Interperiodica”

2. The state of combustion products is modeled by a uniform gas bubble with pressure

$$P = P_m(t)\varphi(V_b), \tag{2}$$

where V_b is the bubble volume. The first multiplicand in (2) depends only on time and characterizes the variation of gas-bubble pressure due to heat release and changes in chemical composition in the course of a constant-volume combustion process. The second multiplicand represents the dependence of pressure on volume in an adiabatic process. Assuming that, in the case when a combustion process takes place in a constant closed volume, pressure is a linear function of the burnt mass fraction and that the combustion front propagates at a constant velocity, we obtain

$$P_m(t) = P_1 + P_{max}\left(\frac{t}{\tau}\right)^2, \quad t \le \tau;$$
$$P_m(t) = P_1 + P_{max}, \quad t > \tau. \tag{3}$$

Here, P_{max} is the pressure attained as the combustible mixture burns out in a constant volume. The second multiplicand in (2) is prescribed in the form of a polytrope:

$$\varphi(V_b) = \left(\frac{V_{b,0}}{V_b}\right)^k = \left(1 + \frac{X}{L}\right)^{-k}, \tag{4}$$

where X is the coordinate of the contact surface measured from its starting position upwards. The values of P_{max} and k are used as parameters that characterize the combustible mixture.

3. In the case of fast combustion, the approximation of a spatially isobaric process is used (see Section 3).

2. SLOW COMBUSTION ($\tau/\tau_w \sim 0.25$–1)

The combustion-induced gradual pressure growth in a gas bubble gives rise to an initially isentropic compression wave propagating in water and transforming into a shock wave after traveling a certain distance. However, it is shown below that when $\tau > \tau_w/4$ (which corresponds to $\tau > 0.5$ s for an LC height of 2700 mm), the distance required for a compression wave to transform into a shock wave is greater than the entire LC height. Under these conditions, until the compression wave reaches the upper LC boundary, the flow in the water column is described by a simple Riemann wave [4]. At the same time, the gas-bubble pressure can be found by solving a first-order ordinary differential equation without introducing any additional simplifying assumptions. In a simple compression wave, the

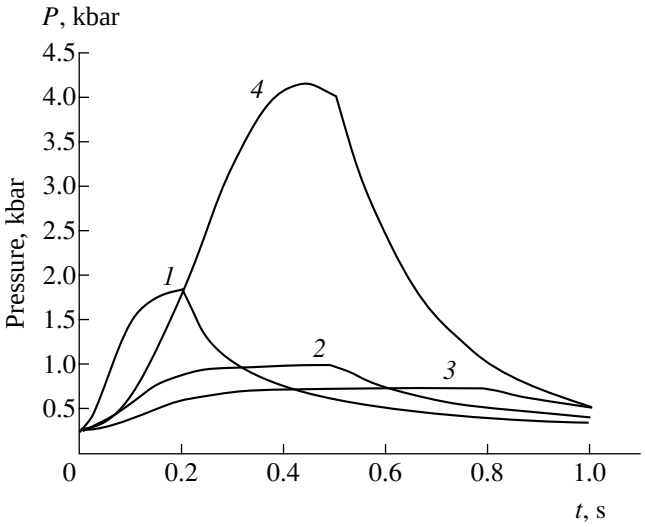

Gas-bubble pressure evolution: (*1*) $\tau = 0.2$; (*2*) 0.5; (*3*) 0.8 s. Incompressible-fluid approximation: (*4*) 0.5 s.

velocity of the medium U is related to the density variation by the well-known equation

$$U = \int_{\rho_1}^{\rho} \frac{C}{\rho} d\rho, \tag{5}$$

where C is the sonic velocity. Substituting into (5) the expression

$$C = \left(\frac{nB\sigma^{n-1}}{\rho_1}\right)^{1/2}, \tag{6}$$

which follows from (1), and integrating the resulting equation, we obtain

$$C = C_1 + \frac{n-1}{2}U. \tag{7}$$

Here, C_1 is the sonic velocity ahead of the wave. {Formula (7) is equivalent to a well-known relation for a simple wave in an inviscid gas [4] when the isentropic exponent is substituted for n.} Combining (6) with (1), we obtain an expression for the sonic velocity as a function of pressure. Then, using (7), we find the following relation between the fluid velocity U and pressure in a simple wave:

$$U(x,t) = \frac{2C_1}{n-1}\left\{\left[\frac{P-P_1}{B} + 1\right]^{(n-1)/2n} - 1\right\}. \tag{8}$$

Applying (8) to the contact surface, we find

$$\frac{dX}{dt} = \frac{2C_1}{n-1}\left\{\left[\frac{P(t)-P_1}{B} + 1\right]^{(n-1)/2n} - 1\right\}, \tag{9}$$

where $P(t)$ is the pressure at the contact surface. This pressure, equal to the gas-bubble pressure, is given

Table

τ, s	a, m/s^2	t_{sh}, s	x_{sh}, m	t_{min}, s
1	70	5.3	7800	2
0.5	190	2.0	2900	2
0.2	640	0.58	860	0.58
0.1	1450	0.27	380	0.27

by (2)–(4). Equation (9) is solved numerically with the initial condition $X_{t=0} = 0$. The figure shows the behavior of $P(t)$ predicted for three values of τ for $k = 2$: (*1*) τ = 0.2, (*2*) 0.5, and (*3*) 0.8 s. As an illustration of the importance of taking water compressibility into account in solving this problem, we also present a result calculated in the approximation of incompressible fluid (curve *4*).

These results can be used to estimate the scope of the solution in terms of the time t_{sh} and location x_{sh} of shock-wave formation. Noting that the contact-surface motion with an approximately constant acceleration a (depending on τ) at $t \le \tau$ is followed by its deceleration, we can use the self-similar solution for a motion driven by a piston moving with a constant acceleration to evaluate t_{sh} [4]. It can be shown that

$$t_{sh} = \frac{2C_1}{(n+1)a}, \quad x_{sh} = \frac{2C_1^2}{(n+1)a}$$

for media described by Eq. (1). The table shows approximate values of a and corresponding values of t_{sh} and x_{sh} for several values of τ. The results presented in the table imply that $t_{sh} > t_w$ and, equivalently, $x_{sh} > H$ when $\tau \ge 0.5$ s and $H \le 3000$ m. In other words, the compression wave cannot transform into a shock wave as it passes by the entire LC length and retains the characteristics of a simple wave described by (8) at $t < t_w$. In the general case of an arbitrary τ, the LC fluid dynamics is described by a simple wave at $t < t_{min} \equiv \min\{t_w, t_{sh}\}$. Analyzing the gas-bubble pressure development, we should bear in mind that the time interval over which Eq. (8) remains valid for a contact surface is approximately twice as long as that for the entire compression wave. This is explained by the fact that this time is determined by the moment when the acoustic wave carrying the information about the incipient breakdown of the simple wave caused by its reflection from the free surface or by its transformation into a shock wave reaches the contact surface, rather than by the moment t_{min}.

3. FAST COMBUSTION ($\tau/\tau_w \ll 1$)

In this case, the shock wave develops near the contact surface and substantially affects $P(t)$. To perform an approximate analytical calculation of $P(t)$, we use the isobaric model; i.e., we assume that the LC state is spatially isobaric (LC pressure is a function of time only). At pressures below 1 to 3 GPa, the Hugoniot adiabat in (1) rewritten in the *D*–*U* representation (where D and U are the shock-wave velocity and fluid velocity behind the front, respectively) is equivalent to the following relation [5]:

$$D = C_1 + 2U. \tag{10}$$

Assuming that the initial water-temperature gradient is negligible, we can use the isobaric model described above to formulate an equation for the motion of the contact surface. In this model, both water velocity and pressure are independent of the coordinate. Therefore, $\frac{dX}{dt} = U$. Substituting (10) into the well known expression for shock pressure $P = \rho_1 DU + P_1$, we obtain

$$P - P_1 = \rho_1 C_1 U + 2\rho_1 U^2. \tag{11}$$

Solving Eq. (11) for U and using the fact that $\frac{dX}{dt} = U$, we arrive at the equation for the coordinate of the contact surface:

$$\frac{dX}{dt} = G + \left[G^2 + \frac{P(X,t) - P_1}{2}\right]^{1/2}, \quad G \equiv -\frac{C_1}{4}, \tag{12}$$

where, as in (9), the function $P(X, t)$ is defined by (2)–(4). However, since $\tau\frac{dX}{dt} \ll L$ in the case of a fast combustion process, Eq. (12) can be integrated under the initial condition $(X = 0)_{t=\tau}$. According to (3), the function $P(X, t)$ does not involve any explicit time dependence under these conditions and Eq. (12) can be solved in quadratures.

CONCLUSION

The method proposed here for modeling the dynamics of a liquid filling a tube can be used to calculate the pressure profile generated when a combustible mixture placed at the bottom closed end of a tube is burned. The calculation takes into account the following defining parameters: the liquid compressibility, parameters of the equations of state, combustion duration, combustible-mixture and liquid heights, and others. This can be performed by both analytically and numerically solving a first-order ordinary differential equation (instead

of by time consuming numerical analysis of partial differential equations of fluid dynamics, as are commonly used in analyses of such problems). It is demonstrated that water compressibility is an important factor that must be taken into account within the range of the parameters considered here.

REFERENCES

1. M. A. Sobolev, A. A. Merkulov, *et al.*, Karotazhnik, No. 57, 24 (1999).
2. R. H. Cole, *Underwater Explosions* (Princeton Univ. Press, Princeton, 1948; Inostrannaya Literatura, Moscow, 1950).
3. *Physical Quantities. Handbook*, Ed. by I. S. Grigor'ev and E. Z. Meilikhov (Énergoizdat, Moscow, 1991).
4. L. D. Landau and E. M. Lifshitz, *Course of Theoretical Physics*, Vol. 6: *Fluid Mechanics* (Nauka, Moscow, 1986; Pergamon, New York, 1987).
5. A. N. Afanasenkov, in *Vzryvnoe delo* (Nedra, Moscow, 1975), No. 75/32, pp. 38–43.

Translated by A. Betev

Doklady Physics, Vol. 45, No. 11, 2000, pp. 596–598. Translated from Doklady Akademii Nauk, Vol. 375, No. 1, 2000, pp. 32–34.
Original Russian Text Copyright © 2000 by Grigolyuk, Fil'shtinskiĭ, Kovalev.

MECHANICS

Bending of a Thick Shell with a Finite Length in R^3

Corresponding Member of the RAS É. I. Grigolyuk*, L. A. Fil'shtinskiĭ, and Yu. D. Kovalev****

Received July 24, 2000

The bending of a layer weakened by a noncircular hole through it was considered in [1]. In [2–4], a similar problem for a layer with a circular hole was solved using other methods. Papers [2–4] are devoted to the study of the stressed states of a hollow circular cylinder with a finite length or an annular plate subjected to symmetric or skew-symmetric loads.

In this paper, we propose a new method for solving three-dimensional problems of elasticity theory for the bending of thick shells of finite length. This method reduces the boundary value problem to an infinite set of one-dimensional singular integral equations. The algorithm obtained makes it possible to study the stressed states of shells with variable thickness, which are used in various crucial constructions.

We consider a skew-symmetric loaded cylindrical shell with finite length $2h$, which is bounded by two cylindrical surfaces whose directrices are smooth closed contours L_1 and L_2 ($L_1 \cap L_2 = \varnothing$).

Let the bases $\bar{x}_3 = \pm h$ of the shell be force-free and the normal and tangential loads N, T, and Z be applied to the cylindrical surfaces.

We assume that the curvatures for both the directrices of the cylindrical surfaces and the vector components of the applied load satisfy the Hölder condition [5] in L_j ($j = 1, 2$) and, moreover, that the functions $N = N(x_1, x_2, \bar{x}_3)$, $T = T(x_1, x_2, \bar{x}_3)$, and $Z = Z(x_1, x_2, \bar{x}_3)$ can be expanded in the interval $[-h, h]$ into the Fourier series with respect to the $\bar{x}_3$-coordinate.

The boundary conditions on the cylindrical surfaces are given by

$$\begin{gathered}(\sigma_{11} + \sigma_{22}) - e^{-2i\psi}(\sigma_{22} - \sigma_{11} + 2i\sigma_{12}) = 2(N - iT), \\ \operatorname{Re}[e^{i\psi}(\sigma_{13} - i\sigma_{23})] = Z,\end{gathered} \tag{1}$$

where ψ is the angle between the outward normal to L_j and the Ox_1-axis.

To describe a stressed state of a thick shell, we proceed from the homogeneous solutions found by Lur'e [6]. These solutions correspond to homogeneous conditions at the cylinder bases.

We write out the integral representations for the biharmonic and metaharmonic functions entering into the homogeneous solutions in the following form:

$$F(x_1, x_2) = \int_L p\Delta G\,ds + \int_L qG\,ds,$$

$$\varphi_m(x_1, x_2) = \int_L g_m K_0(\sigma_m r)\,ds,$$

$$\psi_k(x_1, x_2) = \int_L q_k K_0(\gamma_k r)\,ds,$$

$$G = r^2 \ln r, \quad r = |\zeta - z|, \quad \zeta - z = re^{i\alpha}, \tag{2}$$

$$L = \bigcup_{j=1}^{2} L_j, \quad \operatorname{Im} g_m = 0, \quad \zeta = \xi_1 + i\xi_2 \in L,$$

$$z = x_1 + ix_2, \quad \sigma_m = \frac{\sigma_m^*}{h}, \quad \gamma_k = \frac{\gamma_k^*}{h},$$

$$\sigma_m^* = \frac{(2m+1)\pi}{2}.$$

Here, $K_n(x)$ is the MacDonald functions; the densities $p(\zeta), \ldots, q_k(\zeta)$ are subject to definition; and γ_k^* are the roots of the corresponding transcendental equation [6].

We expand all even and odd components of both the stress tensor and applied load into the Fourier cosine and sine series, respectively:

$$U = \sum u_m \cos\sigma_m^* x_3,$$

$$V = \sum v_m \sin\sigma_m^* x_3$$

with $x_3 = \dfrac{\bar{x}_3}{h}$.

With regard to these expansions, we obtain the following boundary conditions for the Fourier coefficients

* *Moscow State Technical University–Moscow Automotive Institute, Moscow, ul. Bol'shaya Semenovskaya 38, 105830 Russia*

** *Sumy State University, ul. Rimskogo-Korsakova 2, Sumy, 400007 Ukraine*

1028-3358/00/4511-0596$20.00 © 2000 MAIK "Nauka/Interperiodica"

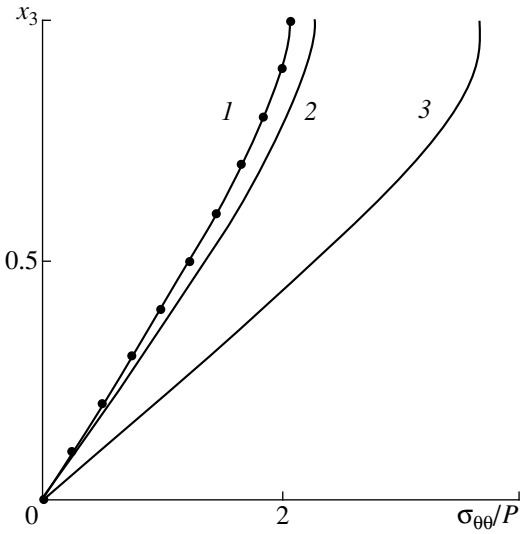

Fig. 1.

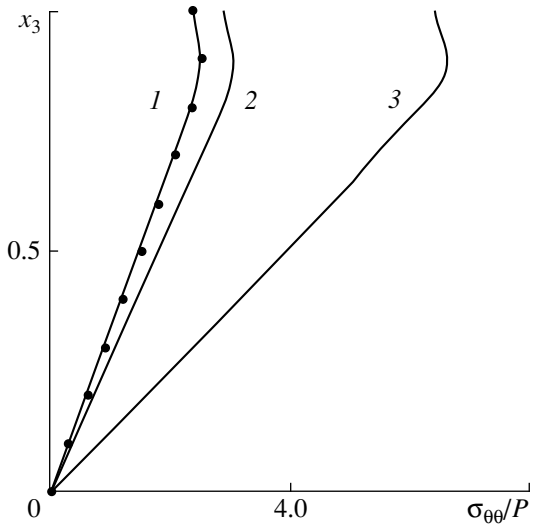

Fig. 2.

of the stress tensor:

$$(\sigma_{11}^{(m)} + \sigma_{22}^{(m)}) - e^{-2i\psi}(\sigma_{22}^{(m)} - \sigma_{11}^{(m)} + 2i\sigma_{12}^{(m)}) = 2(N_m - iT_m), \quad (3)$$

$$\mathrm{Re}[e^{i\psi}(\sigma_{13}^{(m)} - i\sigma_{23}^{(m)})] = Z_m, \quad m = 0, 1, \ldots$$

Using representations (2) and the expressions for stress given in [6], evaluating the Fourier coefficients $\sigma_{ij}^{(m)}$, and substituting their limiting values into boundary conditions (3), we arrive at an infinite set of one-dimensional singular integro-differential equations. Here, we do not write out this set because it is too cumbersome.

The numerical simulation of the infinite set was performed by the method of mechanical quadratures [7] and the subsequent application of the reduction method.

To characterize the stress state of the cylindrical surfaces, we consider three components of the stress vector:

$$\sigma_{\theta\theta} = \sigma_{11}\sin^2\theta + \sigma_{22}\cos^2\theta - 2\sigma_{12}\cos\theta\sin\theta,$$

$$\sigma_{\theta z} = -\sigma_{13}\sin\theta + \sigma_{23}\cos\theta, \quad \theta = \psi - \pi, \quad (4)$$

$$\sigma_{zz} = \sigma_{33}.$$

To evaluate them, we first solve numerically the set of the integro-differential equations for the boundary value problem, then determine the Fourier coefficients $\sigma_{ij}^{(m)}$ and, using formulas (4), calculate the desired stress of the cylindrical surface.

As an example, we consider a thick shell with a cylindrical surface having the following directrices:

$$L_1: \xi_1^{(1)} = R_1^{(1)}\cos\varphi_1, \quad \xi_2^{(1)} = R_2^{(1)}\sin\varphi_1, \quad 0 \le \varphi_1 < 2\pi;$$

$$L_2: \xi_1^{(2)} = R_1^{(2)}\cos\varphi_2 + p_1, \quad \xi_2^{(2)} = R_2^{(2)}\sin\varphi_2 + p_2, \quad 0 \le \varphi_2 < 2\pi.$$

Here, L_1 is the exterior contour.

Let the inner cylindrical surface of the shell be force-free and the outer surface be subjected to the load

$$2(N - iT) = Px_3(1 + e^{-2i\psi}).$$

In this case, the relative stress $\sigma_{\theta\theta}/P$ at the point $\varphi_2 = \pi/2$ is shown in Fig. 1 as a function of the x_3-coordinate. The curves *1*, *2*, and *3* correspond to $R_1^{(1)} = R_2^{(1)} = 11$,

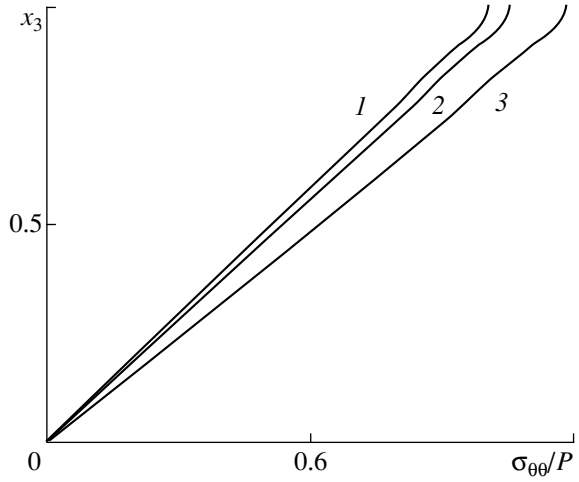

Fig. 3.

4, and 2, respectively, with $h/R_1^{(2)} = 1$ ($p_1 = p_2 = 0$) and $R_1^{(2)} = R_2^{(2)} = 1$. The similar curves in the case of $h/R_1^{(2)} = 4$ are presented in Fig. 2. The dots show the results of [2, 4], which correspond to the bending of a force-free layer weakened by the tunnel hole through it and subjected to the load $\sigma_{11}^{\infty} = Px_3$ at infinity.

Let the inner cylindrical surface of the shell be force-free and the outer surface be subjected to the load $N = Px_3$. In this case, the relative stress $\sigma_{\theta\theta}/P$ at the point $\varphi_2 = \pi/2$ as a function of the x_3-coordinate is shown in Fig. 3. The curves *1*, *2*, and *3* correspond to $p_1 = 0$, 6, and 8, respectively, with $h/R_1^{(2)} = 1$, $R_1^{(2)} = R_2^{(2)} = 1$, $R_1^{(1)} = 10$, $R_2^{(1)} = 5$, and $p_2 = 0$.

The numerical results are obtained for the Poisson's ratio $\nu = 1/3$.

REFERENCES

1. É. I. Grigolyuk, Yu. D. Kovalev, and L. A. Fil'shtinskiĭ, Dokl. Akad. Nauk **345**, 54 (1995) [Phys. Dokl. **40**, 592 (1995)].
2. V. T. Grinchenko, *Equilibrium and Steady Vibrations of Elastic Bodies of a Finite Size* (Naukova Dumka, Kiev, 1978).
3. A. S. Kosmodamianskiĭ and V. A. Shaldyrvan, *Thick Multiply Connected Plates* (Naukova Dumka, Kiev, 1978).
4. A. F. Ulitko, *Method of Proper Vector Functions in Spatial Problems of Elasticity Theory* (Naukova Dumka, Kiev, 1979).
5. N. I. Muskhelishvili, *Singular Integral Equations* (Fizmatgiz, Moscow, 1962; Wolters-Noordhoff, Groningen, 1972).
6. A. I. Lur'e, Prikl. Mat. Mekh. **6** (2/3), 151 (1942).
7. S. M. Belotserkovskiĭ and I. K. Lifanov, *Numerical Methods in Singular Integral Equations* (Nauka, Moscow, 1986).

Translated by V. Chechin

Doklady Physics, Vol. 45, No. 11, 2000, pp. 599–600. Translated from Doklady Akademii Nauk, Vol. 375, No. 1, 2000, pp. 35–36.
Original Russian Text Copyright © 2000 by Zubov.

MECHANICS

A New Form for the Newtonian Law of Gravitation

Corresponding Member of the RAS V. I. Zubov

Received June 05, 2000

In this study, the mathematical theory for a new form of the Newtonian law of gravitation is developed [1]. This form manifests itself in the appearance of time-independent sets in a gravitational field. The potential of this field can also differ from the Newtonian potential as little as desired. Yet this makes it possible to explain the quantization of planetary orbits, the appearance of Saturnian rings, and the striped character of the asteroid belt. Kepler developed his laws for planetary motion on the basis of the observations of Tycho Brahe. However, his extension of the results of these observations to arbitrary positions of closed orbits was unjustified. Newton found the potential for the gravitational field based on the Keplerian laws. Therefore, the potential found by Newton cannot be used for describing the planetary motion in the cases mentioned above.

We consider for definiteness the motion of a mass point in the central gravitational field:

$$m\ddot{R} = -\frac{kmR}{r^3}, \tag{1}$$

where $R = \begin{pmatrix} x \\ y \\ z \end{pmatrix}$ is the vector column and r is its Euclidean length $r = \sqrt{x^2 + y^2 + z^2}$.

Equation (1) can also be represented in the form

$$\ddot{R} = \operatorname{grad}\frac{k}{r}. \tag{2}$$

Here, m is the mass of the mass point and k is the gravitational constant.

We put $\zeta = \log r$. Then, the Newtonian potential is

$$ke^{-\zeta}. \tag{3}$$

We introduce into the consideration the potential

$$ke^{-\zeta}[1 + f(\zeta)] \tag{4}$$

instead of potential (3). Then, for potential (4), Eq. (2) takes the form

$$\ddot{R} = -\frac{kR\varphi(\zeta)}{r^3}. \tag{5}$$

In this case, function $\varphi(\zeta)$ is determined from the equation

$$\varphi(\zeta) = 1 + f(\zeta) - f'(\zeta). \tag{6}$$

Here, the derivative of function f with respect to parameter ζ is denoted as f'.

Theorem 1. *For the arbitrary choice of a continuous bounded function $\varphi(\zeta)$ given for $\zeta \in (-\infty, +\infty)$, Eq.* (6) *has the unique bounded solution $f_0(\zeta)$, which is continuously differentiable. In this case, if function $\varphi(\zeta)$ is periodic, then $f_0(\zeta)$ is also periodic, and if function $\varphi(\zeta)$ is almost periodic, then $f_0(\zeta)$ is also almost periodic.*

Remark 1.1. The function $f_0(\zeta)$ is defined by the formula

$$f_0(\zeta) = \int_{\zeta}^{+\infty} e^{(\zeta-\eta)}\varphi(\eta)d\eta. \tag{7}$$

Remark 1.2. It follows from formula (7) that if function φ is a bounded integrable function, then f_0 is continuous and bounded.

We introduce into the consideration a set R of points in space E^3, in which function $\varphi > 0$, and denote this set as F^+. Similarly, we denote F^- and F^0 as sets of points in the space E^3 for which $\varphi < 0$ and $\varphi = 0$, respectively.

Theorem 2. *A set of circular orbits entirely situated in set F^+ passes through the arbitrary point of set F^+. None of the circular orbits can pass through the arbitrary point of set F^-. Moreover, any motion corresponding to the unbounded increase or decrease of time leaves set F^-. If the motion starts in set F^0 and has the initial zeroth velocity, then the motion remains there: in other words, the time-independent motions are accumulated in this set.*

Remark 2.1. If $R^0 \in F^0$, then the circular orbit

$$R = R^0\cos\omega t + \frac{1}{\omega}\dot{R}^0\sin\omega t$$

is the solution to system (5) and is entirely contained in

St. Petersburg State University,
Universitetskaya nab. 7/9, St. Petersburg,
199164 Russia

1028-3358/00/4511-0599$20.00 © 2000 MAIK “Nauka/Interperiodica”

set F^+ provided that R^0 is orthogonal to $\dot{R}^0$ and $|\dot{R}^0| = |R^0|\omega$, where $\omega = \sqrt{\varphi(\zeta)}$ and $\zeta = \ln r^0$.

Remark 2.2. If $R^0 \in F^-$, then for the motion with the initial given R^0, $\dot{R}^0$ remains in the Laplacian plane and exhibits hyperbolic behavior with a tendency to leave set F^- while increasing and decreasing time.

Remark 2.3. We assume $f(\zeta) = \varepsilon\cos\mu\zeta$; then for a reasonably small ε, the variation of the Newtonian potential is as small as desired. However, the function $\varphi(\zeta) = \varepsilon\cos\mu\zeta - \varepsilon\mu\sin\mu\zeta + 1$ for a sufficiently large parameter μ quantifies space E^+ into sets F^+ and F^-, which are separated by spheres belonging to set F^0.

The behavior of the motion in sets F^+, F^-, and F^0 are described above. This behavior shows that the modification proposed for the Newtonian law of gravitation is more adapted to the description of not only planetary systems but also of the structure of atoms, since function $\varphi(\zeta)$ is given for all values $\zeta \in (-\infty, +\infty)$.

Let the initial condition R^0, $\dot{R}^0$ for system (1) be given. Then, these conditions define the Laplacian plane passing through the origin, so that the motion given by these initial data lies in this plane. We represent the motions occurring in this plane with the help of polar coordinates:

$$\rho = \frac{\alpha}{1 - \varepsilon\cos\psi}. \tag{8}$$

Here, ρ and ψ are polar coordinates and ε and α are certain parameters.

In the Cartesian coordinates corresponding to this plane, the motion can be represented in the form

$$\begin{aligned} \xi &= \rho\cos\psi, \\ \eta &= \rho\sin\psi. \end{aligned} \tag{9}$$

Functions (9) satisfy the system of differential equations

$$\begin{aligned} \xi' &= -\eta + \gamma\xi\eta, \\ \eta' &= \xi + \gamma\eta^2, \end{aligned} \tag{10}$$

where $\gamma = \varepsilon/\alpha$ is the system parameter.

Theorem 3. *System* (10) *has the first integral*

$$\frac{\xi^2 + \eta^2}{(\gamma\xi - 1)^2} = I.$$

If the initial conditions ξ_0, η_0 for a given $\gamma > 0$ satisfy the inequality $I_0 < 1$, $I_0 = \dfrac{\xi_0^2 + \eta_0^2}{(\gamma\xi_0 - 1)^2}$, then they define an ellipse in the Laplacian plane. Moreover, the family of the ellipses has the boundary $I_0 = 1$, which is a parabola. For $I_0 > 1$, the equation $I = I_0$ determines a hyperbola in the plane. As $\gamma\xi_0 - 1 \longrightarrow 0$, $I_0 \longrightarrow +\infty$. The limiting value defines the integral manifold $\xi = 1/\gamma$. This integral manifold divides the Laplacian plane into two halves, so that motions beginning in one of the halves never approach the other half. This phenomenon is called The Great Chinese Wall in observational astronomy.

If $\gamma = 0$, then all motions in the Laplacian plane are circular. The behavior of system (10) for $\gamma < 0$ is determined from the above in the case of replacing ξ with $-\xi$ and ψ with $-\psi$.

For the modified potential, Eqs. (10) take the form

$$\begin{aligned} \xi' &= -\eta + \gamma\xi\eta(1 + g(\rho)), \\ \eta' &= \xi + \gamma\eta^2(1 + g(\rho)). \end{aligned} \tag{11}$$

Theorem 4. *Integrating system* (11) *yields the integral equation*

$$\rho = \frac{\alpha}{1 - \varepsilon\cos\left(\psi + \int_0^\psi g(\rho)d\psi\right)}. \tag{12}$$

Remark 4.1. It follows from Eqs. (11) and (12) that the existence of closed orbits situated in all the sets F^+, F^-, and F^0 is plausible. These orbits can help us to explain the diving motions of Martian satellites, the orbit-to-orbit transitions for Saturnian satellites, and the existence of fresh comets.

Remark 4.2. In the case of the Newtonian potential, it was established [2] that the arbitrary motion of matter can be represented in the phase space as a totality of three topological transformations occurring simultaneously: the orthogonal transformation, the transformation of compression or extension, and another successive orthogonal transformation. This remark also remains valid for the modified potential.

REFERENCES

1. M. F. Subbotin, in *Course of Celestial Mechanics* (Gostekhteorizdat, Moscow, 1941), Vol. 2.
2. V. I. Zubov, *Control Processes and Stability. Collection of Papers* (St. Petersburg Univ., St. Petersburg, 1999).

Translated by G. Merzon

Doklady Physics, Vol. 45, No. 11, 2000, pp. 601–605. Translated from Doklady Akademii Nauk, Vol. 375, No. 1, 2000, pp. 37–41.
Original Russian Text Copyright © 2000 by Klimov, Nesterov, Akulenko, Georgievskiĭ, Kumakshev.

MECHANICS

Flow of a Viscoplastic Medium with Low Yield Strength in a Flat Confuser

Academician D. M. Klimov*, S. V. Nesterov*, L. D. Akulenko*, D. V. Georgievskiĭ, and S. A. Kumakshev***

Received June 9, 2000

1. When the shear yield strength of a material tends to zero, the scalar constitutive relation of the viscoplastic medium (the Bingham–Il'yushin model) is reduced to a physically linear relation for viscous fluid. In this limit, the flow studied below, in a certain sense, tends to the classical Jeffery–Hamel flow. The steady motion of viscous fluid in a flat confuser and a diffuser have been studied intensively [1–6]. Sometimes, this motion was chosen as a support flow for the approximate solution of a more complicated problem, for example, the nonisothermal problem [3]. Perturbing the Jeffery–Hamel flow by a low yield strength can be classed as a problem of deformation stability against the perturbation of material functions [4, 5, 7].

We developed a mathematical formalism for investigation of the flows in a viscoplastic medium having a low yield strength under deformation in a flat confuser. The approach is valid at arbitrary values of constitutive parameters of the system, i.e., the opening angle and the Reynolds number. The efficient numerical and analytical method of accelerated convergence and the efficient computational algorithm are constructed. The corresponding software is created. A high-accuracy complete solution to the problem is constructed within the class of symmetrical functions at the fixed opening angle, and the numerical simulation is performed. Previously unknown graphical relationships are obtained; mechanical effects are revealed and interpreted.

Let the flow of a viscous incompressible fluid having density ρ and dynamic viscosity μ occur in the region $\Omega = \{r, \theta: r > 0, |\theta| < \beta\}$, where 2β is the confuser opening angle and $Q > 0$ is the outflow rate. Then, components v_r^0 and v_θ^0 of the velocity vector $\mathbf{v}^0$, components v_{rr}^0, $v_{\theta\theta}^0$, and $v_{r\theta}^0$ of the strain rate tensor v^0, and maximum slip velocity U^0 have the form

$$\begin{gathered} v_r^0 = -Qr^{-1}V(\theta), \quad v_{rr}^0 = -v_{\theta\theta}^0 = Qr^{-2}V(\theta), \\ v_{r\theta}^0 = -Qr^{-2}V'(\theta)/2, \\ v_\theta^0 \equiv 0, \quad U^0 \equiv (2v:v)^{1/2} = Qr^{-2}F(\theta), \\ F(\theta) = (V'^2 + 4V^2)^{1/2}, \end{gathered} \tag{1}$$

where V is an unknown dimensionless function to be determined. For flow (1), the incompressibility condition is met automatically.

In viscous fluid, components σ_{rr}^0, $\sigma_{\theta\theta}^0$, σ_{zz}^0, and $\sigma_{r\theta}^0$ of the stress tensor σ^0 as well as T^0 are expressed in the form

$$\begin{gathered} \sigma_{rr;\,\theta\theta}^0 = -p^0 \pm \frac{2\rho Q^2}{\mathrm{Re}} r^{-2}V(\theta), \quad \sigma_{zz}^0 = -p^0, \\ \sigma_{r\theta}^0 = -\frac{\rho Q^2}{\mathrm{Re}} r^{-2}V'(\theta), \quad T^0 = \frac{\rho Q^2}{\mathrm{Re}} r^{-2}F(\theta), \end{gathered} \tag{2}$$

where $\rho Q/\mu$ is the Reynolds number and p^0 is the pressure. The quantities U^0 and T^0 are interrelated by the scalar constitutive relation of a viscous medium $T^0 = (\rho Q/\mathrm{Re})/U^0$.

Desired function $V(\theta)$ is a solution to the following nonlinear boundary-value problem corresponding to a constant flow rate [1, 2, 6]:

$$\begin{gathered} V'' + 4V - \mathrm{Re}V^2 = C, \\ V(\pm\beta) = 0, \quad \int_{-\beta}^{\beta} V(\theta)d\theta = 1. \end{gathered} \tag{3}$$

Here, C is an arbitrary constant [$C = V'(\pm\beta)$] to be determined from (3). As a result, parameters (1), (2), and the pressure

$$p^0 = \frac{\rho Q^2}{\mathrm{Re}} r^{-2}\frac{C - 4V}{2} \tag{4}$$

will be fully determined.

* *Institute of Problems of Mechanics, Russian Academy of Sciences, pr. Vernadskogo 101, Moscow, 117526 Russia*

** *Moscow State University, Vorob'evy gory, Moscow, 119899 Russia*

1028-3358/00/4511-0601$20.00 © 2000 MAIK "Nauka/Interperiodica"

The numerical and analytical solution to problem (3), convenient in further analysis of viscoplastic flow, is constructed in [6] for the parameter range ($0 < \beta < \pi/2$, $0 < \mathrm{Re} \lesssim 10^3$) and is of interest for its potential applications.

2. We consider the flow of a viscoplastic medium (the Bingham–Il'yushin model) obeying the scalar relationship

$$T = \tau_s + \frac{\rho Q}{\mathrm{Re}} U, \quad \tau_s > 0. \tag{5}$$

The existence of shear yield point τ_s in (5) leads to contradictions when solving for the separation of variables. A review of analytical, numerical, and experimental studies of such flows both in flat and conical confusers and diffusers is given in [4]. Below, we present the formulation of the problem and possible approaches to its solution.

In domain Ω, we use the equations of motion and the incompressibility condition

$$-\mathrm{grad}\, p + \mathrm{Div} s = \rho \dot{\mathbf{v}}, \quad \mathrm{div}\mathbf{v} = 0. \tag{6}$$

The stress deviator $s = \sigma + pI$, where σ is the stress tensor, is related to the strain rate tensor v by the vector constitutive relations

$$s = 2\left(\frac{\tau_s}{U} + \frac{\rho Q}{\mathrm{Re}}\right) v. \tag{7}$$

Using the relation between tensor v and vector $\mathbf{v}$ (the Stokes relationships) in (7) and substituting (7) into (6) yields a closed system of three equations with respect to v_r, v_θ, and p. This system is complemented by nonslip boundary conditions and a constant flow rate condition:

$$\mathbf{v}(\pm\beta) = 0, \quad \int_{-\beta}^{\beta} r v_r d\theta = -Q. \tag{8}$$

An approximate solution to problem (5)–(7) is constructed using asymptotic expansion in powers of a small numerical parameter τ, which characterizes the relative smallness of dimensional quantity τ_s in (5) and (7):

$$\begin{aligned} &\mathbf{v} = \mathbf{v}^0 + \tau \mathbf{v}^{(1)} + \ldots, \quad p = p^0 + \tau p^{(1)} + \ldots, \\ &v = v^0 + \tau v^{(1)} + \ldots, \quad s = s^0 + \tau s^{(1)} + \ldots, \\ &U = U^0 + \tau U^{(1)} + \ldots. \end{aligned} \tag{9}$$

The first terms in expansions (9) correspond to the Jeffery–Hamel flow (Section 1). Substitution of (9) into (5)–(7) yields the following first-approximation equations for the unknown variables $\mathbf{v}^{(1)}$, $p^{(1)}$, $v^{(1)}$, $s^{(1)}$, and $U^{(1)}$ [4]:

$$\begin{aligned} -p^{(1)}_{,r} + \frac{s^{(1)}_{r\theta,\theta}}{r} + s^{(1)}_{rr,r} + 2\frac{s^{(1)}_{rr}}{r} &= -\rho Q\left(\frac{V}{r} v^{(1)}_{r,r} - \frac{V}{r^2} v^{(1)}_r + \frac{V'}{r^2} v^{(1)}_\theta\right), \\ -p^{(1)}_{,\theta} + \frac{s^{(1)}_{rr,\theta}}{r} + s^{(1)}_{r\theta,r} + 2\frac{s^{(1)}_{r\theta}}{r} &= -\rho Q\left(\frac{V}{r} v^{(1)}_{\theta,r} + \frac{V}{r^2} v^{(1)}_\theta\right), \\ v^{(1)}_{r,r} + \frac{v^{(1)}_r}{r} + \frac{v^{(1)}_{\theta,\theta}}{r} &= 0, \quad U^{(1)} = 2v^0 : \frac{v^{(1)}}{U^0}. \end{aligned} \tag{10}$$

Using both the Stokes relationships and formula (1), we can present tensor $s^{(1)}$ and its components as

$$\begin{aligned} s^{(1)} &= 2\left[\frac{\tau_s}{\tau}\frac{v^0}{U^0} + \frac{\rho Q}{\mathrm{Re}} v^{(1)}\right], \\ s^{(1)}_{rr} &= -s^{(1)}_{\theta\theta} = \frac{\tau_s}{\tau}\sin\Psi + \frac{2\rho Q}{\mathrm{Re}} v^{(1)}_{r,r}, \\ \sin\Psi &\equiv 2\frac{v^0_{rr}}{U^0}, \quad 0 < \Psi < \pi, \\ s^{(1)}_{r\theta} &= \frac{\tau_s}{\tau}\cos\Psi + \frac{\rho Q}{\mathrm{Re}}\left(\frac{v^{(1)}_{r,\theta}}{r} + v^{(1)}_{\theta,r} - \frac{v^{(1)}_\theta}{r}\right), \\ \cos\Psi &\equiv 2\frac{v^0_{r,\theta}}{U^0}. \end{aligned} \tag{11}$$

According to (3) and (8), the boundary conditions and the constant-flow-rate condition for $\mathbf{v}^{(1)}$ have the form

$$v^{(1)}_r(\pm\beta) = v^{(1)}_\theta(\pm\beta) = 0, \quad \int_{-\beta}^{\beta} r v^{(1)}_r d\theta = 0. \tag{12}$$

Substitution of expressions (11) into (10) leads to a closed linear system of equations with respect to $v^{(1)}_r$, $v^{(1)}_\theta$, and $p^{(1)}$. Due to functions $\sin\Psi$ and $\cos\Psi$, these equations are inhomogeneous and should be solved taking into account conditions (12).

3. A solution to problem (10)–(12) is sought in the form [4]

$$v^{(1)}_r = -\frac{\tau_s}{\tau\rho Q}\frac{rW'(\theta)}{2}, \quad v^{(1)}_\theta = \frac{\tau_s}{\tau\rho Q} rW(\theta), \tag{13}$$

where $W(\theta)$ is the dimensionless stream function. For expressions (13), incompressibility condition (10) is met automatically. Components of tensor $v^{(1)}$ are determined based on (13). The problem of finding the desired functions $v^{(1)}_r$, $v^{(1)}_\theta$, and $p^{(1)}$ can be reduced to

the following linear nonhomogeneous boundary-value problem for only one unknown stream function $W(\theta)$ [4]:

$$\left[-\frac{W'''}{\mathrm{Re}} - \frac{4W'}{\mathrm{Re}} + 2V'W + 2(\cos\Psi)' + 4\sin\Psi\right]' = 0, \quad W(\pm\beta) = W'(\pm\beta) = 0. \tag{14}$$

Using (14), we find $W(\theta)$ and then determine the pressure perturbation $p^{(1)}$:

$$p^{(1)} = \left[-\frac{\rho Q}{\mathrm{Re}}\left(\frac{W'''}{2} + 2W'\right) + \frac{\tau_s}{\tau}(\cos\Psi)' + 2\frac{\tau_s}{\tau}\sin\Psi + \rho Q V'W\right]\ln r + P(\theta), \tag{15}$$

$$P'(\theta) = 2\rho Q V W - \frac{\tau_s}{\tau}(\sin\Psi)' + 2\left(\frac{\tau_s}{\tau}\right)\cos\Psi.$$

Note that known expressions for function $V(\theta)$ and its derivatives should be substituted into (14) and (15). Otherwise, the boundary-value problems (3) and (14) should be solved simultaneously.

As is known, the rigid zones (flow cores) $\Omega_r \subseteq \Omega$ can form during the deformation of viscoplastic media. At small τ, these zones Ω_r and their boundaries Σ_r, which separate them from viscoplastic flow, are determined from the conditions

$$\Omega_r = \{r, \theta: T < \tau_s\}, \quad \Sigma_r = \{r, \theta: 2\tau\nu^0: \nu^{(1)} = -U^{02}\}. \tag{16}$$

In the laboratory reference system, the boundaries of rigid (quasi-rigid) zones are immobile. However, there occurs a mass transfer inside them.

Determination of the asymptotic boundaries Σ_r as $\tau_s \longrightarrow 0$ is of particular interest. Substituting expressions (1) for ν^0 and $\nu^{(1)}$ into (16), we find the boundary of rigid zone $r^*(\theta)$ in polar coordinates:

$$r^*(\theta) = Q\sqrt{\frac{\rho}{\tau_s}}R(\theta), \quad R = \frac{\sqrt{2}F}{D}, \quad D = (4VW' - V'W'')^{1/2}. \tag{17}$$

Denominator $D(\theta)$ is not defined at all $\theta \in (-\beta; \beta)$ (see below).

At the rigid-zone boundary $r^*(\theta)$ (17), the components of both velocity vector $\mathbf{v}^*$ and strain rate tensor ν^* are described by the approximate expressions

$$\mathbf{v}^* = \sqrt{\frac{\tau_s}{\rho}}\mathbf{V}(\theta), \quad V_r = -\frac{V}{R} - \frac{RW'}{2}, \quad V_\theta = RW,$$
$$\nu^* = \frac{\tau_s}{\rho Q}V(\theta), \quad V_{rr} = -V_{\theta\theta} = \frac{V}{R^2} - \frac{W'}{2}, \quad V_{r\theta} = -\frac{V'}{2R^2} - \frac{W''}{4}. \tag{18}$$

4. Approximate analysis of the problem concerning the steady-state flow of a viscoplastic medium with a low yield strength is reduced to solving a nonlinear boundary-value problem. It is described by an eighth-order system of equations and contains four unknown integration constants. The solution also depends on the parameters of the system, angle β and the Reynolds number Re, which vary in a wide range. Below, we present the results of a numerical and analytical study of the problem. These results are based on the modified method of accelerated convergence, which was developed by us and is accurate to a relative error of 10^{-5}–10^{-7}.

To calculate and present the results conveniently, we reduce the boundary-value problem (3), (14) to normalized variables, i.e., to argument x and unknown functions $y(x)$ and $w(x)$. As a result,

$$z' = y - 1, \quad y(x) \equiv 2\beta V(\theta), \quad x = \frac{\theta + \beta}{2\beta}, \quad 0 \le x \le 1,$$
$$y'' + a^2 y - by^2 = \lambda; \quad z, y, w, w' = 0, \quad x = 0, 1,$$
$$w''' + a^2 w' - 2by'w = k + \phi, \quad w(x) \equiv W(\theta), \tag{19}$$
$$\phi(y, y', \lambda, a, b) \equiv a^3 by(y'^2 + a^2y^2)^{-3/2} \times (2y'^2 + 2a^2y^2 - \lambda y - by^3),$$

where $\lambda = (2\beta)^3 C$ and k are arbitrary constants which should be determined while solving the boundary-value problem at given $a = 4\beta$ and $b = 2\beta\mathrm{Re}$. Parameters λ and k can be eliminated by differentiation with respect to x. Variable z corresponds to a quadrature in (3), i.e., to the condition of a constant flow rate. Function ϕ (19) arises owing to functions $\cos\Psi$ and $\sin\Psi$ in (14).

Note that the boundary-value problem for z and y can be separated out. Its sufficiently complete analytical and numerical solution, which belongs to the class of symmetrical functions, is presented in [6]. The computational aspect of the problem lies in the determination of $\gamma = y'(0)$ and $\lambda = y''(0)$ at given a and b. The solution is obtained as a result of integration of the Cauchy problem. At fixed values of the parameter a (i.e., angle β), $\gamma(b)$ and $\lambda(b)$ are determined by the recurrent algorithm of accelerated convergence and the continuation procedure with respect to the parameter b.

At known values of y, y', and λ, solving the linear boundary-value problem for $w(x)$ (19) is reduced to the determination of missing values of parameters $c = w''(0)$ and $k = w'''(0)$. Values of $c(b)$ and $k(b)$ (a is fixed) are calculated by a single integration of the three Cauchy problems for functions w_c, w_k, and w_ϕ. They are described by the equation and initial data of type (19) under the following additional conditions: $k = \phi \equiv 0$ and $w_c'' = 1$ (for w_c); $k = 1$, $\phi \equiv 0$, and $w_k''(0) = 0$ (for w_k); and $k = w_\phi''(0) = 0$ (for w_ϕ). Having been calculated, the functions $w_c(x)$, $w_k(x)$, and $w_\phi(x)$ then allow us to present the desired function $w(x)$ as $w = cw_c +$

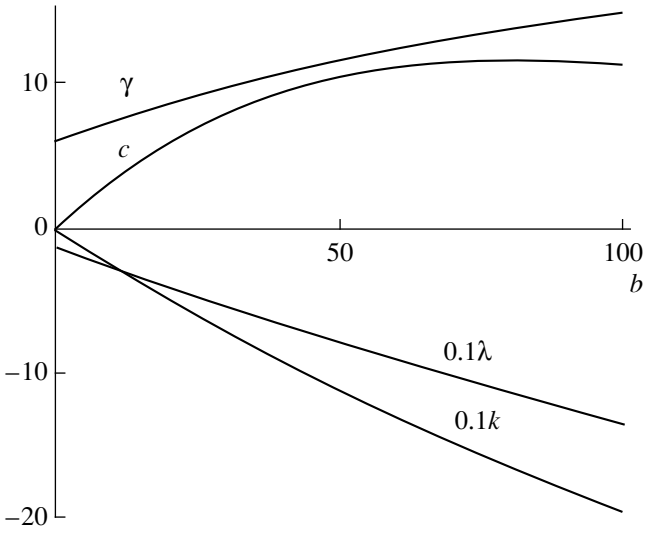

Fig. 1. Missing initial data vs. parameter b (Re number).

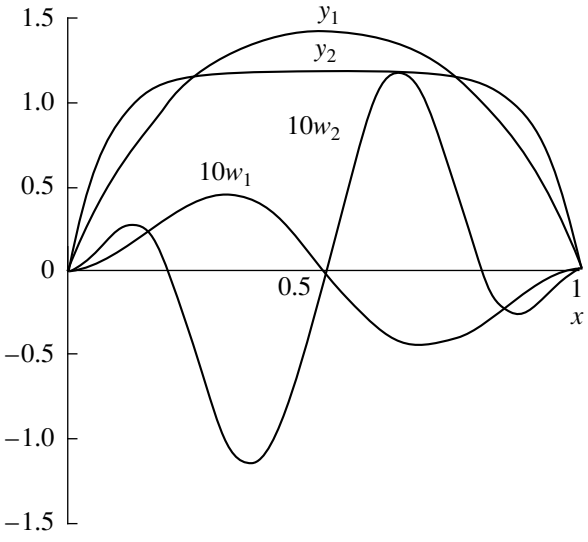

Fig. 2. Profiles $y_{1,2}(x)$ of velocity in a viscous fluid and the stream functions $w_{1,2}(x)$ of a viscoplastic medium at $b_1 = 10$ and $b_2 = 100$.

$kw_k + w_\phi$ and to find coefficients c and k using boundary conditions (19):

$$\begin{aligned} c &= [w_k(1)w'_\phi - w'_k(1)w_\phi(1)]\delta^{-1}, \\ k &= [w'_c(1)w_\phi - w_c(1)w'_\phi(1)]\delta^{-1}, \\ \delta &= w_c(1)w'_k(1) - w'_c(1)w_k(1) \neq 0. \end{aligned} \tag{20}$$

Using (19) and (20) to calculate the quantities c and k at required values of the parameters a and b, i.e., β and Re, we can determine function $w(x)$ and its derivatives w' and w'' as a solution to the Cauchy problem for Eq. (19). These functions are also used to construct the desired characteristics of the viscoplastic flow. They are r^*, v_r^*, v_θ^*, and so forth; i.e., $R^* = R(x)$, $V_r^* = V_r(x)$, $V_\theta^* = V_\theta(x)$, etc. [see (17) and (18)].

The calculated characteristics of viscous and viscoplastic flows symmetric with respect to $x = 1/2$ in a flat confuser are illustrated in Figs. 1–3. The calculations have the relative error of 10^{-4}–10^{-5}. For the sake of definiteness, we consider the case $\beta = 10°$. Parameter b varies within the range $0 \le b \le 100$, i.e., where $0 \le \mathrm{Re} \lesssim 300$. Functions $\gamma(b)$, $\lambda(b)$, $c(b)$, and $k(b)$, which determine a solution to boundary-value problem (19) through the integration of the corresponding Cauchy problem, are plotted in Fig. 1. These curves have a relatively simple form. However, they are difficult to plot based on (20) and [6] since tedious computations are required, especially at $b \gg 1$. Typical plots $y_{1,2}$ and $w_{1,2}$ of variables $y(x)$ and $w(x)$ at $b = b_{1,2}$, where $b_1 = 10$ and $b_2 = 100$, are shown in Fig. 2.

We revealed the following qualitative effect: at $0 < b \le b^* \lesssim 60$ ($b_1 < 60$), the flow of a viscoplastic medium in the confuser is characterized by two quasi-rigid zones, which are situated symmetrically with respect to $x = 1/2$ ($\theta = 0$) (Fig. 3a). Far from the origin of coordinates, the medium flows mainly through three gaps, which are situated along the confuser walls and between the zones, i.e., in certain neighborhoods of $x = 0$, 1/2, and 1. At small b, the central gap between the zones is narrow (arbitrarily narrow as $b \longrightarrow 0$). With an increase in b ($b \lesssim b^*$), expansion occurs while the zones become narrower. At $b > b^*$ ($b_2 > b^*$), the third quasi-rigid zone arises along the central confuser ray and the medium flows through four gaps, which are situated near the walls and between the zones (Fig. 3b). When the parameter b grows, the lateral zones converge and shift toward the confuser walls while the central zone expands. It is noteworthy that the boundaries $R_{1,2}(x)$ (17) of the quasi-rigid zones have vertical asymptotes corresponding to rays for argument θ. These asymptotes are related to zeros of the denominator $D(x)$ in the expression for $R(x)$ in (17); positive and negative values of the radicand in D correspond to the zones $R(x)$ and to the gaps through which the medium flows, respectively. According to (17) and (18), plots for the velocity components at zone boundaries $V_r(x)$ and $V_\theta(x)$ also have vertical asymptotes at the mentioned points. We note that at $b < b^*$, the radial velocity component V_{r1} changes its sign at the zone boundary when x varies with respect to the midpoint $x = 1/2$ ($\theta = 0$): it is positive between the zones and negative between the zones and the walls. The transverse component $V_{\theta 1}$ is antisymmetric with respect to $x = 1/2$ and directed toward the middle part of the confuser.

When there are three quasi-rigid zones ($b_2 = 100$), component V_{r2} of the velocity for particles in the outer zones varies similarly to V_{r1}. In the central zone, this quantity is strictly negative and the transverse velocity

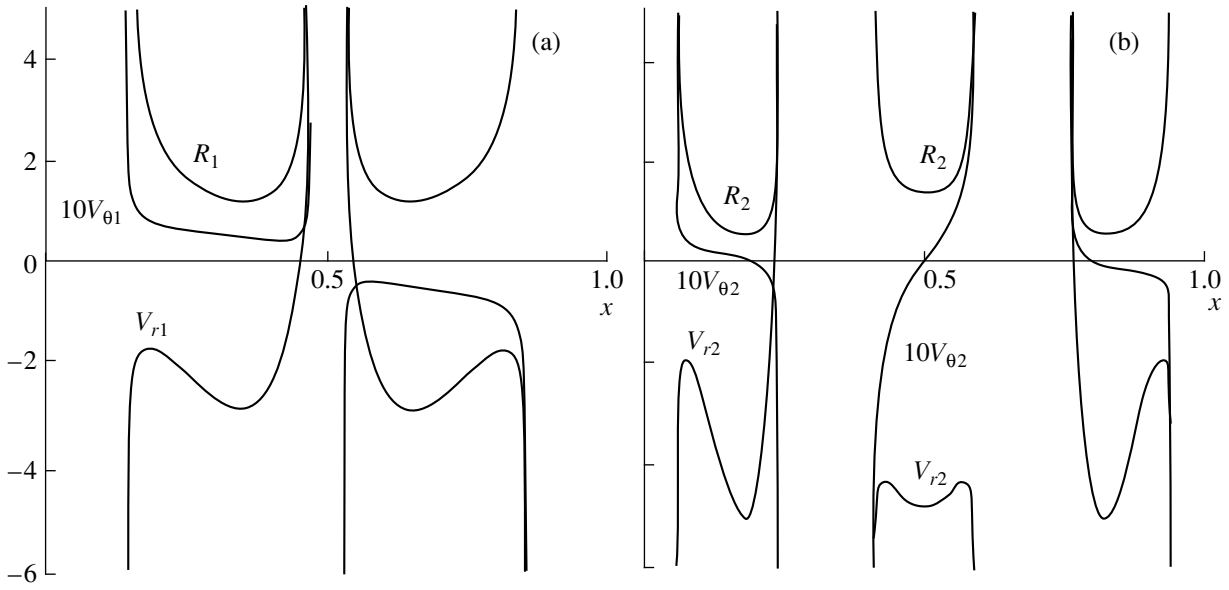

Fig. 3. Boundaries of quasi-rigid zones $R_{1,2}(x)$ and radial $[V_{r1,2}(x)]$ and transverse $[V_{\theta 1,2}(x)]$ velocity components at these boundaries for $b_1 = 10$ and $b_2 = 100$.

component $V_{\theta 2}$ is directed toward the confuser walls. Due to this fact, the central zone expands. In the outer (near-wall) zones, the transverse velocity component changes its sign. Closer to the walls, it is directed toward the middle of the confuser and has the opposite direction (toward the walls) inside the flow. Consequently, these zones become narrower. Moreover, as b grows, they shift toward the confuser walls.

In the framework of the approximate model under study ($\tau_s \longrightarrow 0$), the behavior of quasi-rigid zones in the limit of $b \longrightarrow \infty$ can be analyzed by using analytical methods and by examining the asymptotic expressions for solving the Jeffery–Hamel problem [1, 4, 6]. According to this analysis, the lateral zones "adhere" to the confuser walls at a certain sufficiently large value of parameter b (i.e., the Reynolds number) and their width decreases (unlimitedly). At the inner boundaries of these zones, the transverse component of the particle velocity is directed toward the walls. The radial component is positive, i.e., directed from the origin of coordinates (oppositely to the main flow of the medium). The central quasi-rigid zone expands and takes the shape of a half-strip with a rectangular lower border (a sector without a vertex). At its boundary, the radial component of the particle velocity is negative (directed to the origin of coordinates). At the lateral parts of this boundary, the transverse components are directed, as for the lateral zones, to the corresponding walls. This is an indication of the tendency to expansion.

ACKNOWLEDGMENTS

This work was supported by the Russian Foundation for Basic Research, projects nos. 99-01-00222, 99-01-00276, 99-01-00125.

REFERENCES

1. N. E. Kochin, I. A. Kibel', and N. V. Roze, in *Theoretical Hydromechanics* (Fizmatgiz, Moscow, 1963), Part 2.
2. L. G. Loĭtsyanskiĭ, *Mechanics of Liquids and Gases* (Nauka, Moscow, 1978).
3. K. Millsaps and K. Pohlhausen, J. Aeronaut. Sci. **20** (3), 187 (1953).
4. D. V. Georgievskiĭ, *Stability of Deformation Processes in Viscoelastic Materials* (URSS, Moscow, 1998).
5. D. V. Georgievskiĭ, Prikl. Mat. Mekh. **63**, 826 (1999).
6. L. D. Akulenko, D. V. Georgievskiĭ, S. A. Kumakshev, and S. V. Nesterov, Dokl. Akad. Nauk **374**, 44 (2000) [Dokl. Phys. **45**, 467 (2000)].
7. G. G. Lipscomb and M. M. Denn, J. Non-Newtonian Fluid Mech. **14**, 337 (1984).

Translated by Yu. Verevochkin

Doklady Physics, Vol. 45, No. 11, 2000, pp. 606–609. Translated from Doklady Akademii Nauk, Vol. 375, No. 1, 2000, pp. 42–45.
Original Russian Text Copyright © 2000 by Lavrovskiĭ, Semenova, Slezkin, Fominykh.

MECHANICS

Mediterranean Lenses as Liquid Gyroscopes in the Ocean

É. K. Lavrovskiĭ, I. P. Semenova, L. N. Slezkin, and V. V. Fominykh

Presented by Academician A. Yu. Ishlinskiĭ June 7, 2000

Received July 5, 2000

Owing to their shape, vast vortex formations found in the ocean at depths of approximately one kilometer have been called lenses [1–4]. Many lenses discovered in the Northern Atlantic thousands of kilometers to the southwest of Gibraltar contained Mediterranean water.

This study is based on the results of observations for three lenses called "Meddy" [3, 4] and the lens "Mesopolygon-85" [1, 2]. The general features intrinsic to this phenomenon and the characteristic orders of magnitudes for their parameters are the following: there exists a density-homogeneous [2] or weakly stratified rotating core [3]; the peripheral velocities are proportional to the radius; the highest peripheral velocity is ~30 cm/s; the rotation time is ~5 to 6 days; the horizontal and vertical sizes of the core are ~20 to 40 km and ~400 m, respectively [2]; the distinctions between the temperature and salinity in the lens center and in the background water at the same horizons attain +4°C and +1‰, respectively; the ratio of the lens-density excess to the background-water density at the same horizons is $\Delta\rho/\rho \sim 10^{-4}$ for the "Mezopolygon-85" lens; and the background-water stratification characterized by a Väisälä–Brunt frequency N squared amounts to $N^2 = \left|\frac{d\rho}{dh}\right|\frac{g}{\rho} \sim 10^{-5}$ s^{-2} at a horizon corresponding to the lens density (h is the depth counted off from the ocean surface and g is the gravitational acceleration).

We propose mechanical models for this phenomenon, which explain the displacements of the lenses for long distances (~3500 km along a straight line for the "Mezopolygon-85" and ~1700 km for the "Meddy-1") from Gibraltar to the southwest and the south and the long lifetime of these formations, ranging from 3 to 10 years and longer according to the estimates of [2].

Explaining the motion of the lenses as being transferred by deepwater flows is not consistent with measurement data. The cause should be sought in the distinctions between the mechanical characteristics of the lenses and those of the ambient water. We imply the distinctions in density and the existence of proper rotation. Initially, we ignore thermohaline processes. The ocean is taken as a perfect incompressible density-inhomogeneous liquid with a stable stratification. In this consideration, we choose a system of coordinates related to the rotating Earth. We compare two approaches: a lens as a rotating solid or as a homogeneous rotating liquid mass. On the basis of full-scale measurements, it was assumed that solids modeling lenses are strongly flattened axisymmetric ellipsoids with a semiaxis ratio of $\sim 10^2$. The effects of the medium are displayed by two mechanisms, namely, by static and dynamic mechanisms presented by Archimedean forces and by dynamic reactions, respectively, which involve the apparent masses. From the theory of motion for a solid in liquid [5], we used the structure of expressions for reactions induced by the motion of perturbed water, while the apparent masses involved in them are determined approximately allowing for the Earth's rotation and the ocean's stratification.

The specific action of these factors is expressed in the blocking perturbances introduced by a lens in a bounded region, whose dimensions are determined by the horizontal Rossby radius $R_R = (gH)^{1/2}/f_0$ (H is the characteristic vertical size, $f_0 = \Omega\sin\varphi$ is the Coriolis parameter, and φ is the latitude of the point under consideration) and by the vertical dimension, the so-called Rossby height, $H_R = L|f_0|/N$ (L is the characteristic horizontal size) [6, 7]. For the lens radius $L = R_l = 20$ km and the lens height $H_l = 0.4$ km, $R_R \sim 250$ km and $H_R \sim 0.2$ km. The perturbed ocean zone containing the lens occupies a cylinder with a radius of ~250 km and a height of ~0.8 km. This qualitative distinction from the classical theory [5], where the perturbed region is infinite, leads to substantial quantitative variations in the apparent masses. Estimations of the apparent masses show that $\lambda_{33} \approx M(R_R)^4/24(R_R - R_l)^2H_RH_l \approx 7.6 \times 10^4M$ along the lens-rotation axis and that $\lambda_{11} \approx \lambda_{22} \ll M$ in the perpendicular direction, where M is the lens mass. The apparent mass λ_{33} of a disk of the same dimensions for a motion within a nonrotating homogeneous unbounded space filled with liquid is lower by three orders of magnitude.

In the position of the hydrostatic equilibrium of a nonrotating solid ellipsoid in a stratified liquid, the hor-

Institute of Mechanics, Moscow State University, Michurinskiĭ pr. 1, Moscow, 117192 Russia

1028-3358/00/4511-0606$20.00 © 2000 MAIK "Nauka/Interperiodica"

izontal plane of symmetry is arranged at a horizon, where the background-water density ρ is equal to the body density ρ_l. The moment of hydrostatic forces is zero. The rotating body has a proper angular momentum $\mathbf{H} = C\boldsymbol{\omega}$, ω = const, C is the polar moment of inertia, and ω is the angular-velocity modulus for the proper rotation. In the case of an anticyclonic rotation (as it takes place in a lens), the angular-momentum vector is directed downwards to the ocean depth. The **H**-vector motion in the inertial space is the sum of its motion with the Earth and its motion with respect to the Earth. When a body has no velocity with respect to the Earth other than a proper-rotation velocity, the **H**-vector variation is related only to the variation of its direction in the inertial space owing to the rotation with the Earth (the gyroscopic precession). According to the theorem on angular-momentum variation, we have for H = const

$$\frac{d\mathbf{H}}{dt} = [\boldsymbol{\Omega} \times \mathbf{H}] = \mathbf{M}. \quad (1)$$

Here, $\boldsymbol{\Omega}$ is the angular velocity of the Earth's rotation and **M** is the moment of external forces acting on the body. For such a motion and anticyclonic rotation of the body, the moment must be directed westward. This is the moment of the Archimedean hydrostatic forces acting on a body in stratified liquid. For this, the body must be inclined in the meridian plane with respect to the local horizon, so that its southern part would be slightly drown, while the northern part must be slightly raised over the horizon as is shown in the figure. The moment M_A of the Archimedean forces acting from the side of a linearly stratified liquid on the axisymmetric ellipsoid of revolution, which is inclined under an angle α to the horizon, is determined by the expression

$$M_A = \frac{1}{5} Vg(c^2 - a^2)\frac{d\rho}{dh} \sin\alpha\cos\alpha.$$

Here, V is the ellipsoid volume, a and c are the large and small semiaxes, and $\frac{d\rho}{dh}$ = const is the coefficient in the dependence of the density variation with depth. The proper kinetic moment of the axisymmetric ellipsoid with mass $M = V\rho_l$ is determined by the expression $H = C\omega = (2/5)V\rho_l a^2\omega$. Substituting H and M_A into (1) and taking into account that $c \ll a$, $\sin\alpha \approx \alpha$, $\cos\alpha \approx 1$ for small angles α and that $\left|\frac{d\rho}{dh}\right|\frac{g}{\rho_l} = N^2$, we obtain an expression for the small angle of inclination α of the body's proper-rotation plane to the local horizon:

$$\alpha = \frac{2|\omega|\cos\varphi}{N^2}. \quad (2)$$

For the "Mezopolygon-85" lens ($\omega \sim \Omega/5$, $\varphi \approx 20°$, and $N^2 \sim 10^{-5}$ s^{-2}), we have $\alpha \approx 1'$, while for the "Meddy-1" lens ($\omega \sim \Omega/6$ and $\varphi \approx 28°$), $\alpha \approx 0.5'$. Possible additions to the angle α and the body inclination

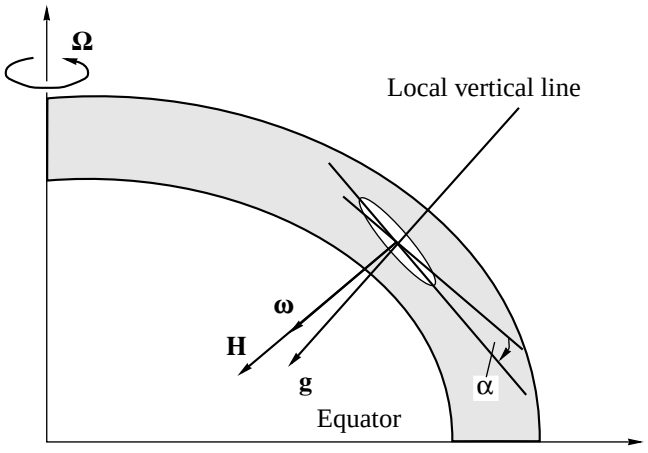

Figure.

to the meridian, which are associated with the lens motion with respect to the Earth with a velocity of 1 cm/s, are four orders of magnitude lower than α. In the case of investigating slow lens motions over long periods of time, these additions may be ignored.

The equations for the relative center-of-mass motion are composed in spherical coordinates: φ and λ are the geocentric latitude and longitude of the point under consideration, respectively, and r is the distance between the body's center of mass and the Earth's center. The ellipsoidal shape of the Earth is taken into account by introducing a small angle $r^{-1}\frac{\partial r}{\partial\varphi}$ between a local vertical and a radius vector directed from the Earth's center. Since

$$\cos\varphi \sim \sin\varphi \sim 1, \quad \left|\frac{d\varphi}{dt}\right| \ll \Omega,$$

$$\left|\frac{d\lambda}{dt}\right| \ll \Omega, \quad r = r(\varphi) + h(t)$$

(h is the depth counted off from the free ocean surface),

$$\frac{dr}{dt} = \frac{\partial r}{\partial\varphi}\frac{d\varphi}{dt} + \frac{dh}{dt}, \quad \left|\frac{dh}{dt}\right| \ll r\left|\frac{d\varphi}{dt}\right|,$$

$$\left|\frac{dh}{dt}\right| \ll r\cos\varphi\left|\frac{d\lambda}{dt}\right|,$$

the set of simplified equations in projections onto the principal axes of the body has the form

$$\begin{aligned} M\frac{d^2\lambda}{dt^2}r\cos\varphi - (2M\sin\varphi + \alpha\lambda_{33}\cos\varphi)\Omega r\frac{d\varphi}{dt} \\ = \lambda_{33}\Omega\cos\varphi\frac{dh}{dt}, \\ Mr\frac{d^2\varphi}{dt^2} + 2M\Omega r\sin\varphi\cos\varphi\frac{d\lambda}{dt} = -[M - m(h)]g\alpha, \\ \lambda_{33}\left[\frac{d^2h}{dt^2} + r\alpha\frac{d^2\varphi}{dt^2}\right] = [M - m(h)]g. \end{aligned} \quad (3)$$

Here, $m(h)g$ is the Archimedean force and the angle α is positive when the southern edge of the body is slightly drown. The first two equations are similar to those of a hydrostatic system and, in the approximation of the precession theory [8] with allowance for relationship $2M\sin\varphi \ll \alpha\lambda_{33}\cos\varphi$ being fulfilled for actual values of parameters, take the form

$$r\frac{d\varphi}{dt} = -\frac{1}{\alpha}\frac{dh}{dt}, \quad r\cos\varphi\frac{d\lambda}{dt} = -\frac{\alpha[M - m(h)]g}{2M\Omega\sin\varphi}. \quad (4)$$

Equation (4) shows that motion along a geographic parallel occurs under the conditions of geostrophic balance when the Coriolis inertia force is balanced by the pressure gradient. In this case, the role of $-\mathrm{grad}p$ is played by the projection onto the meridian of the skating force along the inclined plane. The former equation relates the velocity along a vertical with the horizontal velocity along a meridian.

From (2) and (4), we obtain the expression for the velocity along a parallel:

$$r\cos\varphi\frac{d\lambda}{dt} = -\frac{\Delta M}{M}\frac{g|\omega|}{N^2\tan\varphi}.$$

For $\frac{\Delta M}{M} \sim 10^{-4}$ (for the center-of-mass position 200 m higher than the relevant isopycnic line), $|\omega| \approx \frac{\Omega}{5} \approx 1.5\times10^{-5}\ \mathrm{s}^{-1}$, $N^2 \approx 10^{-5}\ \mathrm{s}^{-2}$, and $\varphi \approx 20°$, we obtain $u \sim 0.5$ cm/s. The order of magnitude for this velocity corresponds to the observed results.

Since $\alpha \ll 1$, we have from (4) that $r\frac{d\varphi}{dt} \gg \frac{dh}{dt}$; consequently, the path traveled by the body along the meridian is much larger than the depth variation. If the body was displaced ~600 km southwards, the submersion was ~90 m. For an average linear horizontal velocity of ~2 cm/s, this occurs for approximately one year. The traveled path, velocity, and time correspond to observations of the "Meddy-1" lens [5].

In the case of a linear stratification of the background and of using the relationship $\alpha r\frac{d^2\varphi}{dt^2} \approx \frac{d^2h}{dt^2}$ following from (4), the third equation of set (3) takes the form

$$2\frac{\lambda_{33}}{M}\frac{d^2h}{dt^2} + N^2h = 0$$

with a period of vibrations of ~10.3 days.

Thus, the mechanical model described reveals the principal features in the slow motion of the lenses, namely, the appearance of the western and southern components for the center-of-mass velocity, i.e., the motion of lenses to the southwest. However, this model is "too fast" for the motion along the vertical channel. We can "slow down" the motion along the vertical by introducing a strong resistance and by taking the turbulent viscosity into account. However, allowing for thermohaline processes which undoubtedly manifest themselves for long periods of time seems to be more appropriate for the model. For example, in effect, the motion of the "Meddy-1" lens at the observation interval is, for the most part, described by Eqs. (4), if we consider the center of mass of the lens to be situated virtually at the corresponding isopycnic line; i.e., $h \approx h_0$, but $h_0 \neq \mathrm{const}$, while $h_0 = h_0(t)$. The low vertical velocity $\frac{dh}{dt} = \frac{dh_0}{dt} > 0$ is caused by thermohaline processes for which the effect of cooling on the density prevails over the effect of salt diffusion from the lens. The lens remaining in the position of quasistatic equilibrium ($[M - m(h_0)] \approx 0$) at each time moment slowly sinks down. We call such a regime thermohaline submersion. It follows from (4) that $\frac{d\lambda}{dt} \approx 0$, $\frac{d\varphi}{dt} = -\frac{dh_0}{dt}/r\alpha < 0$; i.e., the longitude remains almost invariable, while the lens moves virtually southwards (observed in [4]).

The long life of the intrusion vortex formations is associated with the existence of the equilibrium form of the lens rotating core. The rotating mass of a liquid, in contrast to a solid inclined at an angle α (2) to the parallel in the equilibrium state, can create the hydrostatic moment necessary for equilibrium by varying its shape. We show that such a steady shape does exist for an anticyclone. We introduce the (x, y, z)-coordinate system with the origin in the center of mass of the lens. Let the z-, x-, and y-axes be directed upwards along the local vertical, eastwards, and northwards, respectively. The characteristic horizontal dimension of the lens is much smaller than the Earth's radius. Therefore, we consider the case of a stratified-liquid plane layer tangent to the Earth and residing in the uniform gravitational field. We represent the vector of the lens-particle velocity $\mathbf{V}$ by the components $v_x = -\omega(y - \kappa z)$, $v_y = \omega x$, and $v_z = 0$. This corresponds to the motion with a constant angular velocity ω along the circumferences whose centers are located along the straight line $y = \kappa z$ in the meridian plane. The equation of continuity is fulfilled. The Gromeko–Lamb equation for the core has the form

$$[2\mathbf{\Omega} + \mathrm{rot}\mathbf{V}]\times\mathbf{V} = -\frac{1}{\rho_l}\mathrm{grad}\Phi,$$
$$\Phi = p_l + 0.5\rho_l V^2 + \rho_l g z. \quad (5)$$

Outside the core, the liquid is quiescent and linearly stratified. The boundary conditions are $p_f(z_b) = p_l(x_b, y_b, z_b)$; x_b, y_b, and z_b are coordinates for the points of the core boundary; and $p_f(z)$ and $p_l(x, y, z)$ are the pressures outside and inside the lens, respectively. The projections of the relative vortex are $(0, \omega\kappa, 2\omega)$; the projections of the planetary vortex are $(0, 2\Omega_y, 2\Omega_z)$; and the projections of the absolute vortex are $(0, 2\Omega_y + \kappa\omega, 2\Omega_z + 2\omega)$. From the consistency requirements for

Eqs. (5), it follows that $\kappa = \frac{2\Omega_y}{2\Omega_z + \omega}$. Note that the tangent of the inclination angle for the absolute vortex with respect to the local vertical is exactly equal to κ. Integrating (5) and using the boundary conditions, we obtain the equation for the water mass interface:

$$\frac{\omega}{2}(\omega + 2\Omega_x)(x^2 + y^2) + \left(\omega\frac{2\Omega_y^2}{2\Omega_z + \omega} - \frac{1}{2}N^2\right)z^2 - 2\Omega_y\omega yz + \Delta = 0. \quad (6)$$

Here, $\Delta = p_l(0, 0, 0) - \int_0^{H_0} \frac{dp_f}{dz}dz$ is the pressure excess in the lens center with respect to the background at $z = 0$ and $z = H_O$ corresponds to the ocean surface. Reducing (6) to the canonical form by rotating the axes about the parallel ($y = y'\cos\alpha - z'\sin\alpha$, $z = y'\sin\alpha + z'\cos\alpha$) at an angle α, we find

$$\tan 2\alpha = \frac{4\omega\Omega_y}{\omega(2\Omega_z + \omega)^{-1}[4\Omega_y^2 - (\omega + 2\Omega_z)^2] - N^2}. \quad (7)$$

In the case of the anticyclone ($\omega < 0$) and the actual values of the parameters for the lenses under observation, it follows that α is a small angle and its expression coincides exactly with (2) for the inclination angle of a solid. The surface obtained is a triaxial ellipsoid close to an ellipsoid of revolution. The equation for this ellipsoid written out in the principal axes for $\alpha \ll 1$ with approximate values for the coefficients is

$$\frac{x^2 + (y')^2}{a^2} + \frac{(z')^2}{c^2} = 1,$$
$$a^2 = \frac{2\Delta}{\rho_1|\omega|(2\Omega_z - |\omega|)} > 0, \quad c^2 = \frac{2\Delta}{\rho_1 N^2} > 0. \quad (8)$$

The ratio between the principal semiaxes is $\frac{a}{c} = \frac{N}{\sqrt{|\omega|(2\Omega_z - |\omega|)}}$. For the "Mezopolygon-85" lens, we have $a/c \sim 1.2 \times 10^2$, which agrees well with the observations. Note that for the cyclone ($\omega > 0$), no closed equilibrium configuration exists for a homogeneous rotating mass of liquid in the stable-stratified ocean. This fact explains why the majority of the vortex formations found in the northern hemisphere were anticyclones [1, 2].

ACKNOWLEDGMENTS

The authors are grateful to S.S. Grigoryan, A.Yu. Ishlinskiĭ, and V.V. Beletskiĭ for their discussions at seminars and valuable remarks.

REFERENCES

1. *Interior Thermal-Wedge Vortices in the Ocean. Collection of Papers*, Ed. by K. N. Fedorov (Inst. Okeanologii Akad. Nauk SSSR, Moscow, 1986).
2. *Hydrophysical Studies According to the Mesopolygon Program. Collection of Scientific Papers*, Ed. by V. G. Kort (Nauka, Moscow, 1988).
3. L. Armi, D. Hebort, N. Oakey, *et al.*, J. Phys. Oceanogr. **19**, 354 (1989).
4. P. Richardson, D. Walsh, L. Armi, *et al.*, J. Phys. Oceanogr. **19**, 371 (1989).
5. N. E. Kochin, I. A. Kibel', and N. V. Roze, in *Theoretical Hydrodynamics* (Gostekhteorizdat, Moscow, 1955), Vol. 1.
6. A. E. Gill, *Atmosphere–Ocean Dynamics* (Academic, New York, 1982; Mir, Moscow, 1986).
7. A. S. Monin, *Theoretical Foundations of Geophysical Hydrodynamics* (Gidrometeoizdat, Leningrad, 1988).
8. A. Yu. Ishlinskiĭ, *Mechanics of Gyroscopic Systems* (Akad. Nauk SSSR, Moscow, 1963).

Translated by V. Bukhanov

Doklady Physics, Vol. 45, No. 11, 2000, pp. 610–612. Translated from Doklady Akademii Nauk, Vol. 375, No. 2, 2000, pp. 188–190.
Original Russian Text Copyright © 2000 by Bykov, Shmidt.

MECHANICS

Exact Time-Dependent Solutions in the Simplest Model of Chain-Flame Propagation

V. I. Bykov and A. V. Shmidt

Presented by Academician A. G. Merzhanov December 17, 1999

Received February 8, 2000

In the theory of combustion, the model of chain-flame propagation was proposed by Ya.B. Zel'dovich and D.A. Frank-Kamenetskiĭ [1] (see also [2]). In succeeding years, this line of research was actively developed by many investigators (see, for example, [3–6]). In modern notation, the following nonlinear equation corresponds to the simplest model of chain-flame propagation:

$$u_t = u_{xx} + 2u^2(1-u), \tag{1}$$

which is referred to as the Zel'dovich model [5, p. 198] by experts in mathematical modeling. At the same time, in mathematical studies on the dynamics of "reaction + diffusion" systems, problem (1) is treated as a part of the so-called KPP (Kholmogorov–Petrovskiĭ–Piskunov) problem concerning the existence of traveling-wave type solutions.

There is a well known classical exact solution to Eq. (1) [4]:

$$u_1(t, x) = \frac{1}{1 + \exp(x-1)}, \tag{2}$$

which has the form of a traveling wave with unity velocity. In this study, we first find the exact time-dependent solution to model (1):

$$u_2(t, x) = \frac{\exp(t-x)-1}{2t + x + \exp(t-x)}, \tag{3}$$

which, in contrast to classical self-similar solution (2), makes it possible to also study the transient processes leading to the steady-state wave. Furthermore, we generalize our consideration to the case of many spatial variables.

In recent years, the technique of constructing exact solutions to the sets of equations of the reaction + diffusion type was developed in the cycle of studies of O.V. Kaptsov [7–10] and in paper [11]. Solution (3) is found using namely this technique. The scheme of constructing solution (3) to model (1) is as follows.

According to [7, 8], manifold

$$h(t, x, u_x, u_{xx}, \ldots) = 0 \tag{4}$$

is invariant with respect to equation (1), if

$$(D_t(h)\big|_{\{1\}})\big|_{\{4\}} = 0, \tag{5}$$

where D_t is the operator of total differentiation with respect to time t. Relationship (5) is assumed to be met due to (1), (4), and their differential consequences with respect to variable x.

Invariant manifold (4) for equation (1) is sought in the form

$$u_{xx} = \alpha(u)u_x + \beta(u). \tag{6}$$

Substituting (6) in (1), we obtain

$$u_t = \alpha(u)u_x + \beta(u) - 2u^3 + 2u^2. \tag{7}$$

Invariance condition (5) for manifold (6) with respect to equation (7) has the form

$$u_{txx} = D_t(\alpha(u)u_x + \beta(u)). \tag{8}$$

Condition (8) must be met due to Eqs. (6), (7), and to their differential consequences:

$$\begin{aligned}&\alpha''u_x^3 + (\alpha u_x + \beta)(2\alpha' u_x + \alpha^2 + \beta' - 6u^2 + 4u)\\ &+ u_x(2\alpha'\alpha u_x + \alpha'\beta + \alpha\beta' + \beta'' u_x - 12u_x u + 4u_x)\\ &= (\alpha' u_x + \beta')(\alpha u_x + \beta - 2u^3 + 2u^2)\\ &+ \alpha(\alpha' u_x^2 + \alpha(\alpha u_x + \beta) + \beta' u_x - 6u_x u^2 + 4u_x u).\end{aligned} \tag{9}$$

Considering (9) as the condition for which the third-power polynomial in terms of u_x becomes zero, we obtain the following set of equations:

$$\alpha'' = 0, \quad 2\alpha'\alpha + \beta'' - 12u + 4 = 0,$$

$$\beta + u^3 - u^2 = 0, \quad \beta'(u^2 - u^3) - \beta(2u - 3u^2) = 0.$$

The solution to this set has the following form:

$$\alpha = 3u - 1, \quad \beta = -u^3 + u^2.$$

Institute of Computer Modeling, Siberian Division, Russian Academy of Sciences, Akademgorodok, Krasnoyarsk, 660036 Russia

1028-3358/00/4511-0610$20.00 © 2000 MAIK "Nauka/Interperiodica"

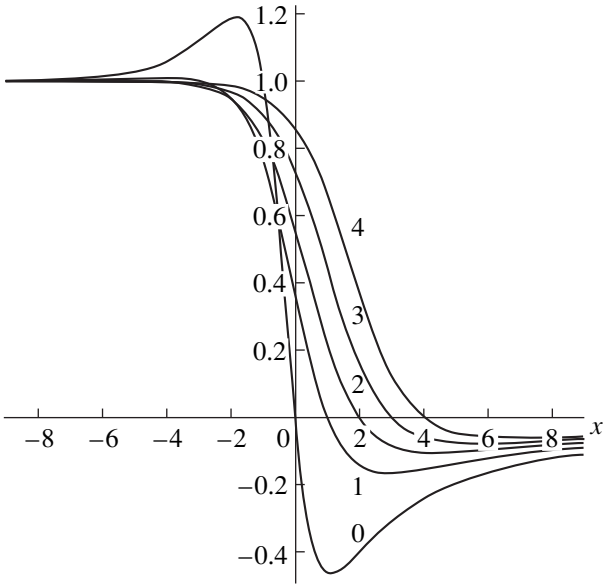

Fig. 1. Characteristic profiles $u_2(t, x)$ at moments of time $t = 0, 1, 2, 3, 4$.

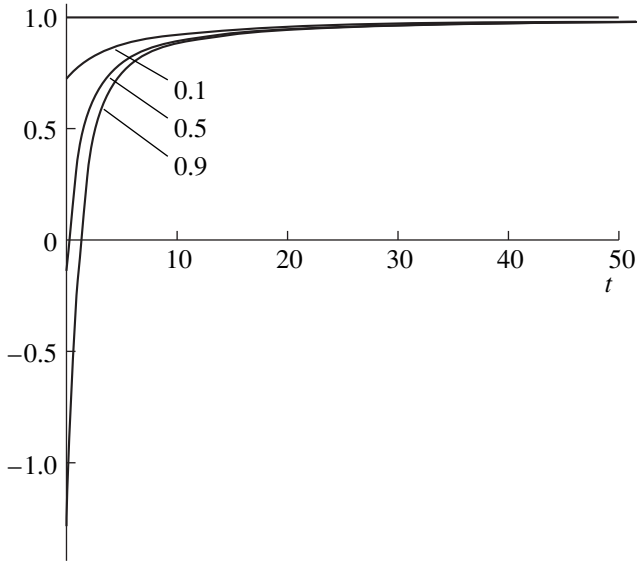

Fig. 2. Asymptotic curves for the velocity of the $u_2(t, x)$ wave propagation for levels $u_2 = 0.1, 0.5, 0.9$.

This means that Eq. (1) has the invariant manifold

$$u_{xx} - (3u - 1)u_x + u^3 - u^2 = 0. \qquad (10)$$

Integrating ordinary differential equation (10) and determining the dependence of the functions of integration on t by means of the substitution of the found solution into Eq. (1), we obtain an explicit solution to (3).

Generally speaking, the described procedure provides an opportunity to obtain a more general expression for the explicit solution to Eq. (1) (with parameters k and m):

$$u(t, x; k, m) = \frac{k\exp(t - x) - 1}{2t + x + m + k\exp(t - x)},$$

which, however, can be transformed to form (3) by shifting independent variables t and x.

Comparing (2) and (3), we note that, accurate to a translation in x, we can pass to the limit

$$u_2(t, x) \longrightarrow u_1(t, x) \quad \text{for } t \longrightarrow \infty;$$

i.e., at reasonably large times, new solution (3) tends to classical self-similar solution (1). What more, $u_2(t, x)$ makes it possible to investigate not only the solutions to model (1) at large times, but also the transient processes. The characteristic profiles $u_2(t, x)$ for various moments of time are shown in Fig. 1. Profile $u_2(t, x)$ has two pronounced extrema (upper and lower "overshoots"). Direct calculations show that the upper overshoot disappears quite quickly, while the lower overshoot tends to zero rather slowly. It is easy to write out the integral characteristics of the upper and lower overshoots:

$$S_{\text{up}} = \int_{-\infty}^{-1-2t} \left(-1 + \frac{\exp(t - x) - 1}{2t + x + \exp(t - x)}\right) dx$$
$$= 3t + 1 - \ln(\exp(3t + 1) - 1),$$

$$S_{\text{low}} = -\int_{t}^{\infty} \frac{\exp(t - x) - 1}{2t + x + \exp(t - x)} dx.$$

The latter integral is diverging. This characterizes the slow convergence to zero of the lower overshoot.

The convergence of $u_2(t, x)$ in the wave velocity is different for various levels of u_2 (Fig. 2). However, at reasonably large times, the velocity of wave motion tends to unity [to the velocity of motion of classical wave (2)]. The relationship between the classical and new solutions to model (1) of chain-flame propagation is illustrated in Fig. 3. The classical wave catches up with the new solution and surpasses it. At times of the order of 10^3, they already move in parallel at a constant velocity.

For a multidimensional model of chain-flame propagation,

$$u_t = \sum_{i=1}^{n} u_{x_i x_i} + 2u^2(1 - u), \qquad (11)$$

the classical self-similar solution has the form

$$u_1(t, x_1, \ldots, x_n) = \frac{1}{1 + \exp(X - t)}, \qquad (12)$$

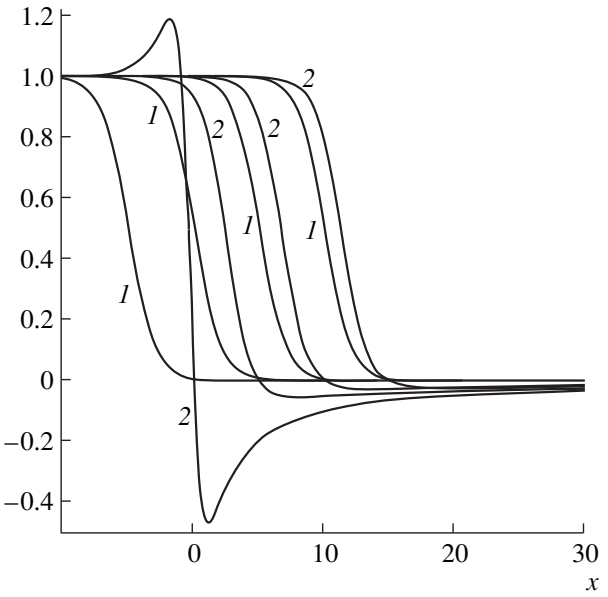

Fig. 3. Comparison of the new (2) and classical (1) solutions at moments of time $t = 0, 5, 10, 15$.

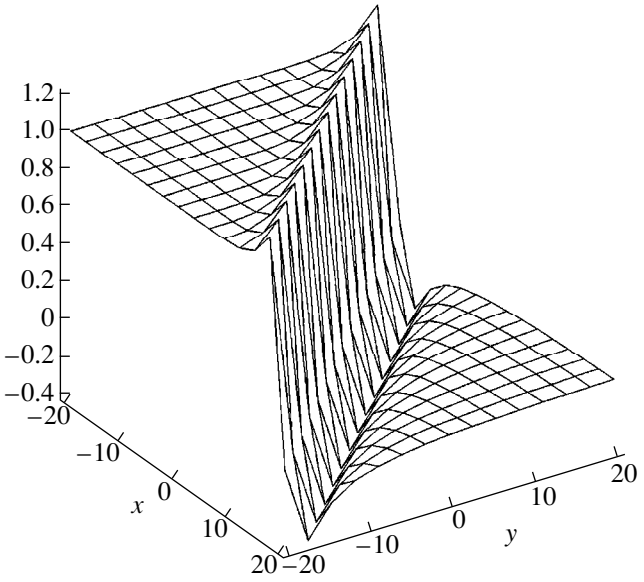

Fig. 4. Profile $u_2(t, x, y)$ for two-dimensional model (11) of chain-flame propagation at $t = 0$.

where $X = \frac{1}{\sqrt{n}}\sum_{i=1}^{n} x_i$. The new time-dependent solution similar to (3) is

$$u_2(t, x_1, \ldots, x_n) = \frac{\exp(t - X) - 1}{2t + X + \exp(t - X)}. \qquad (13)$$

The two-dimensional-wave profile $u_2(t, x_1, x_2)$ at the moment of time $t = 0$ is shown in Fig. 4. Nonlinear "step" (13) tends to classical step (12) at reasonably large times, which is similar to what occurs in the one-dimensional case (see Fig. 3).

Thus, in this paper, we considered a new exact solution to the model of chain-flame propagation. This solution enables us to investigate not only the limiting regimes, but the transient ones as well. Knowledge of such solutions can be used, in particular, in testing the numerical algorithms and codes intended for calculating the mathematical models of the reaction + diffusion type having a more general form than those considered here. Knowledge of the parameter-dependent exact solutions $u_2(t, x; k, m)$ also provides an opportunity to easily analyze the effect of these parameters on the characteristics of wave processes in specific systems.

ACKNOWLEDGMENTS

This work was supported in part by the Russian Foundation for Basic Research, grant no. 97-01-00770, and by a grant from the Russian Ministry of Education.

REFERENCES

1. Ya. B. Zel'dovich and D. A. Frank-Kamenetskiĭ, Dokl. Akad. Nauk SSSR **19**, 693 (1938).
2. D. A. Frank-Kamenetskiĭ, *Diffusion and Heat Transfer in Chemical Kinetics* (Nauka, Moscow, 1987).
3. Ya. B. Zel'dovich, G. I. Barenblatt, V. B. Librovich, and G. M. Makhviladze, *Mathematical Theory of Combustion and Explosion* (Nauka, Moscow, 1980).
4. A. G. Merzhanov and B. I. Khaikin, Prog. Energ. Combust. Sci. **14**, 1 (1988).
5. V. P. Maslov, V. G. Danilov, and K. A. Volosov, *Mathematical Modeling of Heat and Mass Transfer Processes* (Nauka, Moscow, 1987).
6. A. I. Vol'pert and I. G. Petrovskiĭ, in *Selected Works. Differential Equations* (Nauka, Moscow, 1987), pp. 333–358.
7. O. V. Kaptsov, Mat. Model. **4** (8), 31 (1992).
8. V. K. Andreev, O. V. Kaptsov, V. V. Pukhnachev, and A. A. Rodionov, *Application of Group-Theoretical Methods in Hydrodynamics* (Nauka, Novosibirsk, 1994).
9. O. V. Kaptsov, Mat. Model. **7** (3), 107 (1995).
10. O. V. Kaptsov, J. Nonlinear Math. Phys. **4** (1), 283 (1995).
11. A. V. Shmidt, Vychisl. Tekhnol. **3** (4), 87 (1998).

Translated by V. Bukhanov

Doklady Physics, Vol. 45, No. 11, 2000, pp. 613–616. Translated from Doklady Akademii Nauk, Vol. 375, No. 2, 2000, pp. 191–194.
Original Russian Text Copyright © 2000 by Ivlev, Ishlinskiĭ, Maksimova.

MECHANICS

On Properties of Isotropic-Fluid Flows

D. D. Ivlev*, Academician A. Yu. Ishlinskiĭ, and L. A. Maksimova***

Received May 18, 2000

We consider the properties of flows for isotropic incompressible fluids under shear-free stress. We argue that in the general case of arbitrary principal stresses, flow is freest when the two principal stresses are equal to each other and the third differs from them. In this case, the flow is governed by wave equations.

1. Saint-Venant [1] proposed the following set of equations describing the plane flow of an isotropic perfectly plastic fluid:

the equilibrium equations

$$\frac{\partial \sigma_x}{\partial x} + \frac{\partial \tau_{xy}}{\partial y} = 0, \quad \frac{\partial \tau_{xy}}{\partial x} + \frac{\partial \sigma_y}{\partial y} = 0, \tag{1.1}$$

where σ_x, σ_y, and τ_{xy} are the stress tensor components in the Cartesian (x, y)-coordinate system;

the plasticity condition

$$(\sigma_x - \sigma_y)^2 + 4\tau_{xy}^2 = 4k^2, \quad k = \text{const}, \tag{1.2}$$

where k is the shear yield stress;

the incompressibility condition

$$\varepsilon_x + \varepsilon_y = 0; \tag{1.3}$$

and the isotropy condition

$$\varepsilon_{xy}(\sigma_x - \sigma_y) = \tau_{xy}(\varepsilon_x - \varepsilon_y), \tag{1.4}$$

where ε_x, ε_y, and ε_{xy} are the strain-rate tensor components.

The isotropy condition (1.4) requires that the principal directions of the stress tensor and those of the strain-rate tensor be coaxial.

We assume that a stressed state with σ_x, σ_y, and τ_{xy} = const exists. In this case, we can choose the coordinate axes along the principal directions 1 and 2, namely,

$$\sigma_x = \sigma_1, \ \sigma_y = \sigma_2, \ \tau_{xy} = 0; \ \sigma_1, \sigma_2 = \text{const}. \tag{1.5}$$

In view of (1.5), the equilibrium equations are satisfied. From (1.2) and (1.5), we have

$$\sigma_1 - \sigma_2 = \pm 2k. \tag{1.6}$$

It follows from (1.4)–(1.6) that

$$\varepsilon_{xy}(\sigma_1 - \sigma_2) = 0, \quad \varepsilon_{xy} k = 0. \tag{1.7}$$

We assume that

$$\sigma_1 = \sigma_2, \quad k = 0. \tag{1.8}$$

By virtue of (1.8), Eq. (1.7) is satisfied and the quantity ε_{xy} may be nonvanishing. In this case, the isotropic-fluid flow is determined by incompressibility condition (1.3), which can be represented as

$$\frac{\partial u}{\partial x} + \frac{\partial v}{\partial y} = 0. \tag{1.9}$$

Here, u and v are the displacement velocity components.

Assuming that the velocity potential exists, namely,

$$u = \frac{\partial \varphi}{\partial x}, \quad v = \frac{\partial \varphi}{\partial y}, \tag{1.10}$$

and using (1.9) and (1.10), we arrive at

$$\frac{\partial^2 \varphi}{\partial x^2} + \frac{\partial^2 \varphi}{\partial y^2} = 0. \tag{1.11}$$

It follows from assumption (1.10) that the flow is irrotational; i.e.,

$$\frac{\partial u}{\partial y} - \frac{\partial v}{\partial x} = 0. \tag{1.12}$$

Relationships (1.9)–(1.12) define the kinematics of a potential flow for an ideal incompressible fluid.

For $k \neq 0$, it follows from (1.6) and (1.7) that

$$\varepsilon_{xy} = 0, \quad \frac{\partial u}{\partial y} + \frac{\partial v}{\partial x} = 0. \tag{1.13}$$

Equations (1.9) and (1.13) govern the flow of an incompressible perfectly plastic fluid under the uniform stress given by (1.5) and (1.6). In order to satisfy the incompressibility condition, we introduce the stream function

$$u = -\frac{\partial \psi}{\partial y}, \quad v = \frac{\partial \psi}{\partial x}. \tag{1.14}$$

* *Institute of Problems in Mechanics, Russian Academy of Sciences, pr. Vernadskogo 101, Moscow, 117526 Russia*

** *Yakovlev Chuvash State Pedagogical University, ul. Dzerzhinskogo 20, Cheboksary, 428000 Russia*

1028-3358/00/4511-0613$20.00 © 2000 MAIK “Nauka/Interperiodica”

It follows from (1.13) and (1.14) that

$$\frac{\partial^2\psi}{\partial x^2} - \frac{\partial^2\psi}{\partial y^2} = 0. \quad (1.15)$$

Thus, for desirably small values of $k \neq 0$, the uniform flow of the isotropic fluid is governed by wave Eq. (1.15). Provided that the stress components are equal to each other, i.e., $\sigma_1 = \sigma_2$, Laplace Eq. (1.11) governs the flow of an ideal incompressible fluid but does not hold true in the limit as $k \longrightarrow 0$ [see (1.6)].

It is worth noting that the relationships between the stress components and the strain rate impose constraints on the flows governed by Eq. (1.15). For an incompressible viscous fluid under conditions (1.15), we can write out that

$$\varepsilon_x + \varepsilon_y = 0, \quad \varepsilon_{xy} = 0, \quad \varepsilon_x - \varepsilon_y = \frac{1}{\mu}(\sigma_1 - \sigma_2), \quad (1.16)$$

where μ is the coefficient of viscosity.

It follows from (1.16) that

$$u = \frac{1}{2\mu}(\sigma_1 - \sigma_2)x + C_1,$$
$$v = -\frac{1}{2\mu}(\sigma_1 - \sigma_2)y + C_2, \quad C_1, C_2 = \text{const}. \quad (1.17)$$

2. In the case of a three-dimensional flow, we consider the incompressibility conditions

$$\varepsilon_x + \varepsilon_y + \varepsilon_z = 0, \ \frac{\partial u}{\partial x} + \frac{\partial v}{\partial y} + \frac{\partial w}{\partial z} = 0 \quad (2.1)$$

and the isotropy conditions [2]

$$\sigma_{ik}\varepsilon_{kj} = \varepsilon_{ik}\sigma_{kj} \quad (2.2)$$

and require that the principal directions for the stress tensor and the strain-rate tensor be coaxial.

In the Cartesian coordinate system, isotropy conditions (2.2) take the form

$$\begin{aligned}
&\sigma_x\varepsilon_{xy} + \tau_{xy}\varepsilon_y + \tau_{xz}\varepsilon_{yz} = \varepsilon_x\tau_{xy} + \varepsilon_{xy}\sigma_y + \varepsilon_{xz}\tau_{yz},\\
&\tau_{xy}\varepsilon_{xz} + \sigma_y\varepsilon_{yz} + \tau_{yz}\varepsilon_z = \varepsilon_{xy}\tau_{xz} + \varepsilon_y\tau_{yz} + \varepsilon_{yz}\sigma_z, \quad (2.3)\\
&\tau_{xz}\varepsilon_z + \tau_{yz}\varepsilon_{xy} + \sigma_z\varepsilon_{xz} = \varepsilon_{xz}\sigma_x + \varepsilon_{yz}\tau_{xy} + \varepsilon_z\tau_{xz}.
\end{aligned}$$

We assume that

$$\tau_{xy} = \tau_{yz} = \tau_{xz} = 0, \quad \sigma_x = \sigma_1, \quad \sigma_y = \sigma_2, \quad \sigma_z = \sigma_3; \quad \sigma_i = \text{const}. \quad (2.4)$$

From (2.3) and in view of (2.4), we have

$$\varepsilon_{xy}(\sigma_1 - \sigma_2) = 0, \quad \varepsilon_{xz}(\sigma_1 - \sigma_3) = 0, \quad \varepsilon_{yz}(\sigma_2 - \sigma_3) = 0. \quad (2.5)$$

We now assume that

$$\sigma_1 = \sigma_2 = \sigma_3. \quad (2.6)$$

In this case, relationships (2.5) are satisfied and the quantities ε_{xy}, ε_{xz}, and ε_{yz} may be nonvanishing.

Assuming that the velocity potential exists, i.e.,

$$u = \frac{\partial\varphi}{\partial x}, \quad v = \frac{\partial\varphi}{\partial y}, \quad w = \frac{\partial\varphi}{\partial z}, \quad (2.7)$$

and using (2.1) and (2.7), we obtain the harmonic Laplace equation

$$\frac{\partial^2\varphi}{\partial x^2} + \frac{\partial^2\varphi}{\partial y^2} + \frac{\partial^2\varphi}{\partial z^2} = 0. \quad (2.8)$$

It follows from conditions (2.7) that the flow is irrotational, i.e.,

$$\frac{\partial u}{\partial y} - \frac{\partial v}{\partial x} = 0, \ \frac{\partial v}{\partial z} - \frac{\partial w}{\partial y} = 0, \ \frac{\partial w}{\partial x} - \frac{\partial u}{\partial z} = 0. \quad (2.9)$$

Relationships (2.1) and (2.7)–(2.9) define the flow kinematics for an ideal incompressible fluid.

In the case of

$$\sigma_1 = \sigma_2, \quad \sigma_1 - \sigma_3 = 2k, \quad k \neq 0, \quad (2.10)$$

we have from (2.5) and (2.10) that

$$\varepsilon_{xz} = \varepsilon_{yz} = 0 \quad (2.11)$$

and that the quantity ε_{xy} may be nonvanishing.

In terms of the displacement-velocity components, Eqs. (2.11) take the form

$$\frac{\partial u}{\partial z} + \frac{\partial w}{\partial x} = 0, \quad \frac{\partial v}{\partial z} + \frac{\partial w}{\partial y} = 0. \quad (2.12)$$

To satisfy Eqs. (2.12), we assume [3] that

$$u = \frac{\partial\psi}{\partial x}, \quad v = \frac{\partial\psi}{\partial y}, \quad w = -\frac{\partial\psi}{\partial z}. \quad (2.13)$$

According to (2.1) and (2.13), the function Ψ must obey the wave equation

$$\frac{\partial^2\psi}{\partial x^2} + \frac{\partial^2\psi}{\partial y^2} - \frac{\partial^2\psi}{\partial z^2} = 0. \quad (2.14)$$

Thus, relationships (2.10), corresponding to the full-plasticity condition [4], specify the shear nature for the flow of an isotropic incompressible fluid.

It follows from relationships (2.13) that

$$\frac{\partial u}{\partial y} - \frac{\partial v}{\partial x} = 0. \quad (2.15)$$

According to (2.15), the flow determined by relationships (2.1) and (2.12)–(2.14) is irrotational in the (x,y)-plane.

In the case of

$$\sigma_i \neq \sigma_j, \quad (2.16)$$

with regard to (2.16) and (2.5), the equation

$$\varepsilon_{xy} = 0, \quad \frac{\partial u}{\partial y} + \frac{\partial v}{\partial x} = 0 \tag{2.17}$$

must be attached to relationships (2.11).

It follows from (2.13) and (2.16) that

$$\frac{\partial^2 \psi}{\partial x \partial y} = 0. \tag{2.18}$$

Using (2.18) and (2.14), we arrive at

$$\psi = f_1(x+z) + f_2(x-z) + f_3(y+z) + f_4(y-z). \tag{2.19}$$

Conditions (2.17) and (2.18) impose constraints on the flow governed by relationships (2.1) and (2.12).

Thus, in the case (2.6) of all principal stresses being equal to each other, Eqs. (2.1) and (2.7)–(2.9), which correspond to the flow of an ideal incompressible fluid, are valid. In the case where not all principal stresses are equal to each other, the flow of an isotropic incompressible fluid is freest when condition (2.10) is satisfied. The flow is governed by relationships (2.1) and (2.12)–(2.14).

3. In the case of the orthogonal curvilinear coordinates α, β, and γ, the incompressibility condition takes the form

$$\varepsilon_\alpha + \varepsilon_\beta + \varepsilon_\gamma = 0. \tag{3.1}$$

If the axes α, β, and γ correspond to the principal directions 1, 2, and 3, respectively, then conditions (2.5) are written out as

$$\varepsilon_{\alpha\beta}(\sigma_1 - \sigma_2) = 0, \quad \varepsilon_{\alpha\gamma}(\sigma_1 - \sigma_3) = 0, \quad \varepsilon_{\beta\gamma}(\sigma_2 - \sigma_3) = 0. \tag{3.2}$$

The relationships

$$\sigma_i = \sigma_j, \quad \sigma_i - \sigma_\kappa = 2k \tag{3.3}$$

specify three cases which are similar to (2.5), (2.10), and (2.11):

$$\varepsilon_{\alpha\gamma} = \varepsilon_{\beta\gamma} = 0, \quad \varepsilon_{\alpha\beta} \neq 0, \tag{3.4}$$

$$\varepsilon_{\alpha\beta} = \varepsilon_{\beta\gamma} = 0, \quad \varepsilon_{\alpha\gamma} \neq 0, \tag{3.5}$$

$$\varepsilon_{\alpha\beta} = \varepsilon_{\alpha\gamma} = 0, \quad \varepsilon_{\beta\gamma} \neq 0. \tag{3.6}$$

As an example, we consider the cylindrical coordinates ρ, θ, and z. In this case,

$$\varepsilon_\rho = \frac{\partial u}{\partial \rho}, \quad \varepsilon_{\rho\theta} = \frac{1}{2}\left[\rho \frac{\partial}{\partial \rho}\left(\frac{v}{\rho}\right) + \frac{1}{\rho}\frac{\partial u}{\partial \theta}\right],$$
$$\varepsilon_\theta = \frac{1}{\rho}\frac{\partial v}{\partial \theta} + \frac{u}{\rho}, \quad \varepsilon_{\theta z} = \frac{1}{2}\left(\frac{1}{\rho}\frac{\partial w}{\partial \theta} + \frac{\partial v}{\partial z}\right), \tag{3.7}$$
$$\varepsilon_z = \frac{\partial w}{\partial z}, \quad \varepsilon_{\rho z} = \frac{1}{2}\left(\frac{\partial u}{\partial z} + \frac{\partial w}{\partial \rho}\right),$$

where u, v, and w are the displacement-velocity components along the axes ρ, θ, and z, respectively.

According to (3.1) and (3.7), the incompressibility equation is given by

$$\frac{\partial u}{\partial \rho} + \frac{1}{\rho}\frac{\partial v}{\partial \theta} + \frac{u}{\rho} + \frac{\partial w}{\partial z} = 0. \tag{3.8}$$

With regard to (3.7), Eqs. (3.4) take the form

$$\varepsilon_{\rho z} = \varepsilon_{\theta z} = 0, \quad \frac{\partial w}{\partial \rho} + \frac{\partial u}{\partial z} = 0, \quad \frac{\partial w}{\partial \theta} + \frac{\partial}{\partial z}(\rho v) = 0. \tag{3.9}$$

For Eqs. (3.9) to be satisfied, we assume that

$$u = \frac{\partial \psi}{\partial \rho}, \quad v = \frac{1}{\rho}\frac{\partial \psi}{\partial \theta}, \quad w = -\frac{\partial \psi}{\partial z}. \tag{3.10}$$

Using Eqs. (3.10) and (3.8), we arrive at

$$\frac{\partial^2 \psi}{\partial \rho^2} + \frac{1}{\rho^2}\frac{\partial^2 \psi}{\partial \theta^2} - \frac{\partial^2 \psi}{\partial z^2} + \frac{1}{\rho}\frac{\partial \psi}{\partial \rho} = 0. \tag{3.11}$$

With allowance for (3.7), Eqs. (3.5) take the form

$$\varepsilon_{\rho\theta} = \varepsilon_{\theta z} = 0, \quad \frac{\partial}{\partial \rho}\left(\frac{v}{\rho}\right) + \frac{\partial}{\partial \theta}\left(\frac{u}{\rho^2}\right) = 0, \quad \frac{\partial}{\partial z}\left(\frac{v}{\rho}\right) + \frac{\partial}{\partial \theta}\left(\frac{w}{\rho^2}\right) = 0. \tag{3.12}$$

For Eqs. (3.12) to be satisfied, we assume that

$$u = \rho^2 \frac{\partial \psi}{\partial \rho}, \quad v = -\rho \frac{\partial \psi}{\partial \theta}, \quad w = \rho^2 \frac{\partial \psi}{\partial z}. \tag{3.13}$$

Using (3.8) and (3.13), we arrive at

$$\frac{\partial^2 \psi}{\partial \rho^2} - \frac{1}{\rho^2}\frac{\partial^2 \psi}{\partial \theta^2} + \frac{\partial^2 \psi}{\partial z^2} + \frac{3}{\rho}\frac{\partial \psi}{\partial \rho} = 0. \tag{3.14}$$

With regard to (3.7), Eqs. (3.6) take the form

$$\varepsilon_{\rho\theta} = \varepsilon_{\rho z} = 0, \quad \frac{\partial}{\partial \rho}\left(\frac{v}{\rho}\right) + \frac{\partial}{\partial \theta}\left(\frac{u}{\rho^2}\right) = 0, \quad \frac{\partial}{\partial z}\left(\frac{v}{\rho^2}\right) + \frac{1}{\rho^2}\frac{\partial w}{\partial \rho} = 0. \tag{3.15}$$

For the first equation of (3.15) to be satisfied, we assume that

$$u = -\rho^2 \frac{\partial \psi}{\partial \rho}, \quad v = \rho \frac{\partial \psi}{\partial \theta}. \tag{3.16}$$

From the second equations of (3.15) and (3.16), we obtain

$$\frac{\partial w}{\partial \rho} = \rho^2 \frac{\partial^2 \psi}{\partial \rho \partial z}. \tag{3.17}$$

Using Eqs. (3.8) and (3.17), we arrive at

$$\frac{\partial^2 w}{\partial\rho\partial z} = -\frac{\partial}{\partial\rho}\left(\frac{\partial u}{\partial\rho} + \frac{1}{\rho}\frac{\partial v}{\partial\theta} + \frac{u}{\rho}\right),$$
$$\frac{\partial^2 w}{\partial\rho\partial z} = \rho^2\frac{\partial^3\psi}{\partial\rho\partial z^2}. \qquad (3.18)$$

From Eqs. (3.18) and (3.16), we obtain the equation for the function $\Phi = \dfrac{\partial\psi}{\partial\rho}$:

$$\frac{\partial^2\Phi}{\partial z^2} + \frac{1}{\rho^2}\frac{\partial^2\Phi}{\partial\theta^2} - \frac{\partial^2\Phi}{\partial\rho^2} - \frac{5}{\rho}\frac{\partial\Phi}{\partial\rho} - \frac{3}{\rho^2}\Phi = 0. \qquad (3.19)$$

REFERENCES

1. B. Saint-Venant, J. Math. Pure Appl., Ser. II **16**, 308 (1871); **16**, 373 (1871); in *Theory of Plasticity* (Inostrannaya Literatura, Moscow, 1948).
2. A. Yu. Ishlinskiĭ, Izv. Akad. Nauk SSSR, Otd. Tekh. Nauk, No. 3 (1945).
3. L. A. Maksimova, Dokl. Akad. Nauk **358**, 772 (1998) [Dokl. Phys. **43**, 131 (1998)].
4. A. Haar and Th. Kárman, Nachr. Ges. Wiss. Goettingen, Math.–Phys. Kl. **2**, 204 (1909); in *Theory of Plasticity* (Inostrannaya Literatura, Moscow, 1948).

Translated by V. Chechin

Doklady Physics, Vol. 45, No. 11, 2000, pp. 617–619. Translated from Doklady Akademii Nauk, Vol. 375, No. 3, 2000, pp. 328–330.
Original Russian Text Copyright © 2000 by Berezkin, Krivosheev, Petrov, Utkin.

MECHANICS

Effect of Delayed Crack Nucleation under Threshold Pulse Loading

A. N. Berezkin, S. I. Krivosheev, Yu. V. Petrov, and A. A. Utkin

Presented by Academician E. I. Shemyakin March 14, 2000

Received March 14, 2000

The kinetic nature of fracture in solids underlies some features in the behavior of macroscopic cracks at the starting stage of their propagation in a dynamic stress field [1–3]. Analysis of experimental data demonstrates that one of the dominant factors in this process is the incubation period of preparation for the development of a macroscopic rupture of a material. Among the effects related to the existence of the incubation time, the effect of fracture delay is of special importance. This effect implies that a rupture at a given point of the material can occur at a stage when the magnitude of the local force field is reduced. This phenomenon was clearly observed in experiments involving the spalling of materials [1] and, based on the theory of incubation time, was predicted for samples with macroscopic cracks [2].

In this paper, we report the results of our experimental study, including those confirming the existence of delayed fracture near the crack tip under short-pulse loading. We interpret these results in terms of the incubation-time criterion [3].

The experiments were performed using polymethyl methacrylate samples. The samples had a thin cut imitating a macroscopic crack and were characterized by the following material parameters: $c_1 = 1970$ m/s, $c_2 = 1130$ m/s, and $K_{I_c} = 1.47$ MPa m$^{1/2}$, where c_1 and c_2 are the longitudinal and transverse velocities of the elastic waves and K_{I_c} is the ultimate stress-intensity factor under static loading.

The character of fracture under dynamic loading was determined with the help of a magnetic-pulse method of loading. The scheme and the procedure of loading [4] created a pulsed pressure uniformly distributed over the edges of the cracklike cut. This pressure was formed using the flat current-carry bus. The generator of the electric-current pulses produced an oscillatory mode discharge with a period $T \sim 5.5$–6 μs and attenuation-time constant $T_1 \sim 4$ μs. The amplitude of the electric-current pulse ranged from 150 to 300 kA in correspondence with the loading stress amplitude varying from 140 to 320 MPa. In the case of the oscillatory mode of the capacitor-bank discharge to the flat copper buses with cross sections chosen to meet the maximum value of the action integral for copper [5], it was possible to consider the pressure distribution as uniform and to determine it using the following relationship:

$$P(t) = P_0 \exp\left(-\frac{2t}{T_1}\right)\sin^2\left(2\pi\frac{t}{T}\right). \quad (1)$$

At the time moment $t_m = \arctan\left(2\pi\frac{T_1}{T}\right)\frac{T}{2/\pi}$, the pressure attains its maximum value

$$P_m = \frac{P_0 \exp\left(-\frac{2t_m}{T_1}\right)}{\left(1 + \frac{T^2/T_1^2}{4/\pi^2}\right)}.$$

As a photochronograph, we used an SFR-2 high-speed camera with the optical scheme assembled to correspond to the chronograph mode.

We tested ten samples. In these tests, the oscillation period T was 5.6 μs, the attenuation-time constant was $T_1 = 4.2$ μs, and the pressure-pulse amplitude P_m varied from 140 to 320 MPa. The results of analyzing a high-speed photography pattern are shown in Fig. 1. Note the stepwise character of the crack growth. At its initial moment, the crack-growth velocity ranges from 100 to 500 m/s depending on the loading. If the applied load exceeds the threshold value, the initial part of the distance passed before the first stop is several millimeters and the corresponding velocity equals 420–450 m/s. The rest part is passed at a substantially lower velocity, on the order of 100 m/s. The moments of stops in the crack motion correlate with the time necessary for the loading wave to pass the doubled distance from the crack edges to the sample boundary. In spite of the stepwise character of the crack growth, the resulting crack

Research Institute of Mathematics and Mechanics, St. Petersburg State University (Petrodvorets Branch), Bibliotechnaya pl. 2, Petrodvorets, 198904 Russia

1028-3358/00/4511-0617$20.00 © 2000 MAIK “Nauka/Interperiodica”

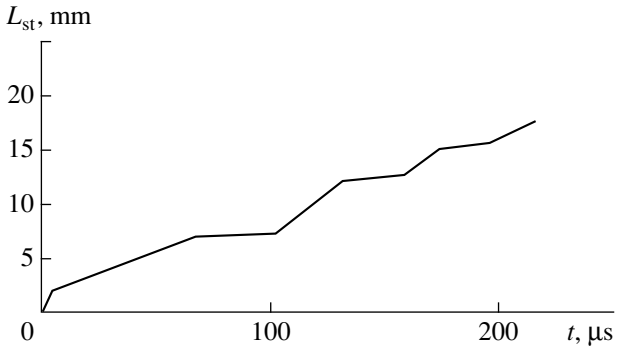

Fig. 1. Typical high-speed photography pattern of crack growth: the crack length L_{st} as a function of time.

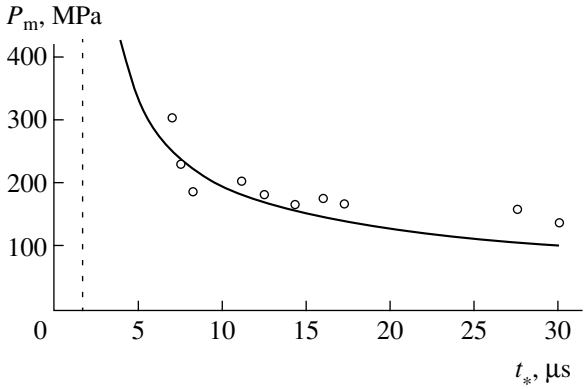

Fig. 2. Amplitude of the fracturing pulse as a function of time elapsed before fracture onset.

length was found to be proportional to the loading amplitude causing the fracture.

Analysis of the high-speed photography patterns allowed us to reveal the dependence of the initial moment of crack propagation on the amplitude of the applied load. To compare this experimental dependence with calculation results, we used the mathematical model involving the loading of edges of a semi-infinite crack by normally acting forces. The solution to such a problem describes the actual experimental situation before the arrival of waves reflected from the model boundaries to the crack tip. For the samples used in the experiment, the time was only slightly larger than 100 μs. The stress-intensity factor has the following form [6] for this problem:

$$K_I(t) = \int_0^t \frac{\alpha P(s)}{\sqrt{t-s}} ds, \qquad (2)$$

where $\alpha = \dfrac{2c_2\sqrt{c_1^2 - c_2^2}}{c_1\sqrt{\pi c_1}}$. Since only loading amplitude $P(t)$ was varied during the experiments, the intensity factor values differed only by a certain multiplier. The highest intensity factor value was attained after the beginning of loading at the time moment $t \approx 1.7$ μs.

The use of the structure-time criterion [3] provides an opportunity to calculate the moment of the fracture onset as a function of the amplitude of the applied pulse. In the case under consideration, this criterion can be written in the form [7]

$$\frac{1}{\tau}\int_{t-\tau}^{t} K_I(t')dt' \le K_{I_c}, \qquad (3)$$

where τ is the incubation time, which is an independent characteristic of the material. For the chosen material, $\tau = 32$ μs. This value was previously found in experiments that determined threshold amplitudes leading to fracture [4].

Calculation shows that the minimum amplitude corresponding to the fracture is 94.7 MPa for the loading pulses used in these experiments. In Fig. 2, we show the calculated dependence of the applied pulse amplitude P_m on the time t_* corresponding to the onset of crack growth. Circles denote the experimental results. It can be seen that the time elapsed before the beginning of crack propagation far exceeds the duration of the loading pulse. The dashed line ($t \approx 1.7$ μs) corresponds to the moment when the stress-intensity factor attains its highest value. The time in this figure is measured from the moment of load application.

Study of the stressed state at the crack tip shows that the crack motion begins at a certain elapsed time after the moment when the local force field at the crack tip attains its peak, i.e., at the descending branch of the stress-intensity factor. It was found that before the beginning of the crack motion, a significant decrease in the stress-intensity factor (by more than a factor of five) can occur. This phenomenon is referred to as delayed fracture. Fracture delay was observed in experiments with the spallinglike fracture [6]. It was also predicted by the fracture theory for materials with cracks [3, 7]. Fracture delay is defined as the time elapsed from the moment when the local force field attains the highest value to the moment of fracture. The delayed fracture can be explained in terms of the structure-time approach, whereas the conventional concept of critical stress-intensity factor is inconsistent with this phenomenon. In Fig. 2, the fracture delay is the distance from the calculated curve or the experimental point to the dashed line.

We may conclude, that the experimental study of fracture in polymethyl methacrylate samples with macroscopic cracks under the effect of loading by microsecond pulses reveals the following characteristic features of this phenomenon:

the stepwise character of the crack growth continuing after the termination of the loading;

proportionality of the crack length to a loading amplitude that exceeds the threshold value;

delay in the beginning of crack motion with respect to the moment of attaining the highest value of a local force field near the crack tip.

ACKNOWLEDGMENTS

This work was supported by the Russian Foundation for Basic Research (project no. 99-01-00718, projects TsKP-97-01-05009 and "Integration") and also by the Competition Center of the St. Petersburg University grants for research in the field of fundamental natural science (the field "Mechanics", project no. 97-0-4.3-28).

REFERENCES

1. N. A. Zlatin, G. S. Pugachev, S. M. Mochalov, and A. M. Bragov, Fiz. Tverd. Tela (Leningrad) **17**, 2599 (1975) [Sov. Phys. Solid State **17**, 1730 (1975)].
2. D. A. Shockey, D. C. Erlich, J. F. Kalthoff, and H. Homma, Eng. Fract. Mech. **23**, 311 (1986).
3. N. F. Morozov and Yu. V. Petrov, *Problems of Dynamics in the Fracture of Solids* (St.-Peterburg. Gos. Univ., St. Petersburg, 1997).
4. S. I. Krivosheev and Yu. V. Petrov, Preprint No. 142, IPMash RAN (Institute of Problems in Machine Science, Russian Academy of Sciences, St. Petersburg, 1997).
5. G. A. Shneerson, *Field and Transient Processes in the Devices with Superhigh Pulse Currents* (Énergoatomizdat, Moscow, 1991; Nova Science, New York, 1997).
6. G. P. Cherepanov, *Mechanics of Brittle Fracture* (Nauka, Moscow, 1974; McGraw-Hill, New York, 1979).
7. Yu. V. Petrov and A. A. Utkin, in *Mechanics of Fracture. Theory and Experiment* (St.-Peterburg. Gos. Univ., St. Petersburg, 1995), pp. 94–104.

Translated by V. Bukhanov

Doklady Physics, Vol. 45, No. 11, 2000, pp. 620–622. Translated from Doklady Akademii Nauk, Vol. 375, No. 3, 2000, pp. 331–333.
Original Russian Text Copyright © 2000 by A. Vinogradov, Yu. Vinogradov.

MECHANICS

Cauchy–Krylov Functions and Algorithms for Solving Boundary Value Problems in Mechanics of Shells

A. Yu. Vinogradov and Yu. I. Vinogradov

Presented by Academician I. F. Obraztsov February 28, 2000

Received February 28, 2000

Using one of the existing methods for the separation of variables, we can reduce arbitrary rigid differential equations to a set of ordinary differential equations of the first order. This set can be represented in the matrix form:

$$\mathbf{Y}'(x) = A\mathbf{Y}(x) + \mathbf{F}(x), \quad (*)' = \frac{d(*)}{dx}, \quad 0 \le x \le 1. \quad (1)$$

Here, $\mathbf{Y} = \{y_1(x), \ldots, y_m(x)\}^{\mathrm{T}}$ is the desired m-dimensional vector function of the problem; $A = \|a_{ij}\|$ is the $m \times m$ matrix of the m-dimensional variable coefficients $a_{ij} = a_{ij}(x)$; and $\mathbf{F} = \{f_1(x), \ldots, f_m(x)\}^{\mathrm{T}}$ is the vector function defining the external load.

The boundary conditions are also represented in the vector-matrix form:

$$H_{\mathrm{L}}(0)\mathbf{Y}(0) = \mathbf{b}_{\mathrm{L}}(0), \quad H_{\mathrm{R}}(1)\mathbf{Y}(1) = \mathbf{b}_{\mathrm{R}}(1). \quad (2)$$

Here, H_{L} and H_{R} are the matrices defining the boundary conditions, which have, respectively, the dimensions $(m - r) \times m$ and $r \times m$ and the ranks $(m - r)$ and r, and $\mathbf{b}_{\mathrm{L}}$ and $\mathbf{b}_{\mathrm{R}}$ are the vectors in the $(m - r)$-space and r-space, respectively.

We assume that an arbitrary solution $\mathbf{Y}_0(x)$ to the set of homogeneous differential equations written out in form (1) can be found to an accuracy of the constants $\mathbf{C}$:

$$\mathbf{Y}_0(x) = \Phi(x)\mathbf{C}, \quad (3)$$

where $\Phi(x)$ is the $m \times m$ matrix of an arbitrary system of functions.

A similar situation took place when A.N. Krylov employed the Cauchy general method [1] of integrating differential equations with constant coefficients and first obtained the known hyperbolic-trigonometric functions for a differential equation governing the bending of elastically supported beams [2].

The Cauchy method, remarkable in terms of its generality, proved complicated in application. Therefore, this method was not employed further. In particular, as applied to differential equations in the mechanics of plates and shells, functions with similar properties have not been obtained to date.

We will seek such a set of functions which would be a solution to the homogeneous differential equation for set (1) and would satisfy the arbitrary initial conditions of the Cauchy problem. Under the initial conditions, this implies that such a set represented in the matrix form is reduced to a unit matrix. Our goal is similar to that of A.N. Krylov, but we use arbitrary solution (3) as a basis rather than the Cauchy method.

We admit that a set of Cauchy–Krylov functions, which is a solution to homogeneous differential Eq. (1), is found. Then,

$$\mathbf{Y}_0(x) = K(x)\mathbf{Y}(0), \quad (4)$$

where $K(x)$ is the $m \times m$ matrix of the Cauchy–Krylov functions and $\mathbf{Y}(0)$ is an m-column defining the arbitrary initial conditions.

Solution (3) is valid for arbitrary values of its argument, among which for $x = 0$. Hence,

$$\mathbf{C} = \Phi(x)^{-1}\mathbf{Y}(0).$$

Eliminating column $\mathbf{C}$ of the integration constants from solution (3) and comparing the result with Eq. (4), we find that the set of Cauchy–Krylov functions is defined by an arbitrary set of functions:

$$K(x) = \Phi(x)\Phi(0)^{-1}. \quad (5)$$

It is evident that the Cauchy–Krylov functions can be constructed, e.g., for differential equations in the mechanics of plates and shells.

It is of principle importance that in contrast to the Cauchy method, the approach under consideration allows us to construct the Cauchy–Krylov functions for differential equations with variable coefficients.

The necessity of seeking an arbitrary set of the functions $\Phi(x)$ is an evident, and possibly the single disadvantage of this method for constructing Cauchy–Krylov functions.

This disadvantage is not detrimental in applications, because solutions have already been found for certain

Institute of Applied Mechanics,
Russian Academy of Sciences,
Leninskiĭ pr. 32a, Moscow, 117334 Russia

1028-3358/00/4511-0620$20.00 © 2000 MAIK “Nauka/Interperiodica”

cases (e.g., solutions have already been obtained for differential equations in the mechanics of standard-shape plates and shells). A similar situation takes place for many equations of mathematical physics.

The fact that the Cauchy–Krylov functions are capable of specifying relations between desired quantities and their values for an arbitrary argument as well as for arbitrary initial conditions is an extremely important feature of these functions, which allows us to construct new methods for solving boundary value problems.

Similarly to the above-said, we can obtain

$$\mathbf{Y}_0(x) = \Phi(x)\Phi(x_s)^{-1}\mathbf{Y}(x_s), \quad (6)$$

where $\Phi(x)\Phi(x_s)^{-1}$ are the Cauchy–Krylov functions and $\mathbf{Y}(x_s)$ is a column of desired quantities for an arbitrary initial argument x_s.

The Cauchy–Krylov functions obtained allow us to construct simple and stable algorithms for solving boundary value problems for rigid differential equations, which save computer calculation time and memory, and to obtain solutions with a controllable accuracy. In order to simplify our consideration, we do not analyze the partial solution to Eq. (1).

As an example, we construct algorithms for solving boundary value problems for rigid differential equations in the mechanics of plates and shells.

We admit that Eq. (1) is written out in the canonical form and that the vector-function $\mathbf{Y}(x)$, characterizing the cross section of a shell, consists of geometric $\mathbf{p}$ and force $\mathbf{q}$ parts. We subdivide the matrix $K(x)$ of the Cauchy–Krylov functions into the corresponding blocks A_{ij}, $i, j = 1, 2$. Then, relationships (6) are represented as two matrix equations:

$$\begin{aligned}\mathbf{q}_s &= -A_{12}^{-1}A_{11}\mathbf{p}_s + A_{12}^{-1}\mathbf{p}_e,\\ \mathbf{q}_e &= (A_{21} - A_{22}A_{12}^{-1}A_{11})\mathbf{p}_s + A_{22}A_{12}^{-1}\mathbf{p}_e.\end{aligned} \quad (7)$$

Here, the indices s and e stand for the start- and end points, respectively, of an arbitrarily chosen interval, in which the numerical calculations are stable along the shell length. Using the geometric and force conditions of conjugation for these stable-calculation intervals, we obtain the set of matrix algebraic equations:

$$B_{11}\mathbf{p}_0 - B_{21}\mathbf{p}_1 = \mathbf{R}_0,$$
$$\ldots$$
$$B_{3i}\mathbf{p}_{i-1} + (B_{4i} - B_{1i+1})\mathbf{p}_i - B_{2i+1}\mathbf{p}_{i+1} = \mathbf{R}_i,$$
$$\ldots$$
$$B_{3s}\mathbf{p}_{s-1} + B_{4s}\mathbf{p}_3 = \mathbf{R}_s,$$

where s is the number of intervals conjugated,

$$B_{i1} = -A_{12i}^{-1}A_{11i}, \quad B_{2i} = -A_{12i}^{-1},$$
$$B_{3i} = (A_{21i} - A_{22i}A_{12i}^{-1}A_{11i}), \quad B_{4i} = A_{22i}A_{12i}^{-1}.$$

Solving the set of the algebraic equations obtained with allowance for the boundary conditions, we find the vectors $\mathbf{p}_i$. The corresponding vectors $\mathbf{q}_i$ are determined by relationships (7). It is evident that the algorithm constructed reproduces the algorithms of analytical solutions to boundary value problems and has no numerical analogues.

A set of algebraic equations for solutions to a boundary value problem can be obtained by the following algorithm of translating the boundary conditions to a given point x^* of an interval.

With the help of the Cauchy–Krylov functions, we define relations between the vector-functions at the ends of arbitrary stable-calculation intervals. For the $(i + 1)$th end of the interval, we have

$$\mathbf{Y}_{i+1} = K(x_{i+1}, x_i)\mathbf{Y}_i. \quad (8)$$

We translate boundary conditions (2) into the ith end of a stable-calculation interval and transform them to the orthonormal form with the help of known formulas used in Godunov's method [3]. As a result, we have

$$W_i\mathbf{Y}_i = \boldsymbol{\omega}_i.$$

Using solution (8), we eliminate Y_i from this expression for the boundary conditions, transform them into the orthonormal form, and obtain the boundary conditions at the $(i + 1)$th end of the stable-calculation interval:

$$W_{i+1}\mathbf{Y}_{i+1} = \boldsymbol{\omega}_{i+1}.$$

Reiterating the procedures described, we translate the boundary conditions defined at the left end of the interval to those at a given point x^*:

$$W_L(x^*)\mathbf{Y}(x^*) = \boldsymbol{\omega}_L(x^*).$$

The boundary conditions at the right end of the interval are similarly translated to the point x^*:

$$W_R(x^*)\mathbf{Y}(x^*) = \boldsymbol{\omega}_R(x^*).$$

Combining the boundary conditions translated into the point x^*, we write out

$$W_L^*\mathbf{Y}(x^*) = \boldsymbol{\omega}^*.$$

At this point, we complete the solution to the boundary value problem with the solution to the algebraic equation obtained:

$$\mathbf{Y}(x^*) = (W_L^*)^{-1}\boldsymbol{\omega}^*.$$

In essence, the algorithm constructed differs from that of Godunov's method, in which the stability of numerically solving differential equations is ensured by the orthonormalization of the solutions rather than, as

is needed, of the boundary conditions as we propose to use.

The simplicity of the methods constructed is evident. Their efficiency was confirmed by the solution of boundary value problems in the mechanics of shells and by the reduction of the computer calculation time by two orders of magnitude. The use of analytically constructed Cauchy–Krylov functions also provides an admissible calculation error.

The methods proposed allow us to use, in practice, numerous analytical solutions to rigid differential equations which were previously considered to be useless when numerically solving boundary value problems.

REFERENCES

1. V. A. Steklov, *Foundation of the Integration Theory of Ordinary Differential Equations* (Gos. Izd., Moscow, 1927).
2. A. N. Krylov, *About Calculation of Beams Laying on an Elastic Base* (Akad. Nauk SSSR, Leningrad, 1931).
3. S. K. Godunov, Usp. Mat. Nauk **16**, 171 (1961).

Translated by V. Chechin

Doklady Physics, Vol. 45, No. 11, 2000, pp. 623–626. Translated from Doklady Akademii Nauk, Vol. 375, No. 3, 2000, pp. 334–337.
Original Russian Text Copyright © 2000 by Vlasov, Fedik.

MECHANICS

Diffusion-Induced Relaxation of Residual Stresses

N. M. Vlasov and Corresponding Member of the RAS I. I. Fedik

Received August 21, 2000

The relaxation kinetics of residual stresses in a cylindrical shell in relation to the diffusion flow of vacancies is considered. Theoretical results are applied to explain the failure of contact between a bulk cylinder and a shell under thermal loading.

The continuity of thermal flow in the construction elements is achieved through the suitable connection of the contacting surfaces. The contact failure is accompanied by an increase in thermal resistance and, as a consequence, by a rise in temperature. The possible cause of this undesired phenomenon is a diffusion-induced relaxation of residual stresses. This relaxation stems from the migration of vacancies and depends on the stressed state in the bulk. Such a dependence is based on the relation between the stress sign and the direction of the vacancy flow in relation to the diffusion. This flow is always directed toward the domain of compressive stress. In this paper, we consider the relaxation kinetics of residual stresses with different signs in a cylindrical shell. The inner surface of the shell is in contact with the surface of a bulk cylinder (for example, a rodlike fuel element with a shell). The choice of such a model system is justified for several reasons. First, in the cylindrical shell, it is possible to obtain residual stresses of different sign through cutting and addition (exclusion) of a part of the material and subsequent joining of the edges of the cut. Second, the distribution of residual stresses is described by simple analytical relationships. Third, a logarithmic dependence of residual stresses on field coordinates enables us to derive the exact analytical solution to the diffusion equation in force fields.

Let the system "cylinder shell" be at a constant temperature with the coefficients of linear expansion being equal. Hence, under these conditions, thermal stresses do not arise. We also assume that the dislocation mechanisms of stress relaxation are negligible since the stresses are small. Then, the residual stresses of different sign in the cylindrical shell are created in the following way. In one case, (a) the edges of the shell cut are moved apart at an angle ω and a missing material is placed in the opening. Thus, the parts of the material near the outer and inner shell surfaces will be in compressed and tensile states, respectively. In the second case, (b) we cut the shell to an opening angle ω and join the edges of the cut. A self-balanced system of residual stresses changes the sign. Now, the material near the inner and that near the outer surface will be in a state of compression and tension, respectively. If cylindrical shells with residual stresses of different sign tightly enclose the solid cylinder, then the contact between them becomes tighter in case (a) and fails in case (b). This is determined by the diffusion-induced vacancy flow resulting from the relaxation of residual stresses. Indeed, in case (a), the vacancy flow is directed from the inner shell surface to the outer. The atomic flow directed in the opposite direction causes a decrease in the inner shell radius, and contact between adjacent surfaces becomes tighter. In case (b), diffusion-induced vacancy flow is directed from the outer surface of the shell to the inner surface. This is accompanied by an increase in the inner shell radius and, as a consequence, by a failure of contact between adjacent surfaces. Thus, diffusion-induced relaxation of residual stresses dependent on sign can either improve the contact between adjacent surfaces or make it worse.

The nonzero components of the residual stress tensor for the operations corresponding to cases (a) and (b) are determined by the following relationships (the planar deformation) [1]:

$$\sigma_{rr} = \frac{\mu\omega}{2\pi(1-\nu)}\left[\ln\frac{r}{R} - \frac{1-\left(\frac{r}{R}\right)^2}{1-\left(\frac{r_0}{R}\right)^2}\left(\frac{r_0}{r}\right)^2\ln\frac{r_0}{R}\right],$$

$$\sigma_{\varphi\varphi} = \frac{\mu\omega}{2\pi(1-\nu)}\left[1 + \ln\frac{r}{R} + \frac{1+\left(\frac{r}{R}\right)^2}{1-\left(\frac{r_0}{R}\right)^2}\left(\frac{r_0}{r}\right)^2\ln\frac{r_0}{R}\right], \quad (1)$$

$$\sigma_{zz} = \nu(\sigma_{rr} + \sigma_{\varphi\varphi})$$

$$= \frac{\mu\omega\nu}{2\pi(1-\nu)}\left[1 + 2\ln\frac{r}{R} + \frac{2\left(\frac{r_0}{R}\right)^2}{1-\left(\frac{r_0}{R}\right)^2}\ln\frac{r_0}{R}\right],$$

where μ is the shear modulus, ν is the Poisson ratio, ω is the rotation angle of the edges of the shell cut, and r_0 and R are the inner and outer radii of the shell, respectively. These relationships are also used to describe the stress field in the neighborhood of the wedge disclina-

1028-3358/00/4511-0623$20.00 © 2000 MAIK "Nauka/Interperiodica"

tion [2], which simulates various structural imperfections of an actual crystal (for example, the ternary joints of grain boundaries in a polycrystal) [3, 4]. The direction of the diffusion-induced vacancy flow is determined by the first invariant of the residual stress tensor:

$$\sigma_{ll} = \sigma_{rr} + \sigma_{\varphi\varphi} + \sigma_{zz}$$
$$= \frac{\mu\omega(1+\nu)}{2\pi(1-\nu)}\left[1 + 2\ln\frac{r}{R} + \frac{2\left(\frac{r_0}{R}\right)^2}{1-\left(\frac{r_0}{R}\right)^2}\ln\frac{r_0}{R}\right]. \quad (2)$$

The sign of σ_{ll} depends on rotation angle ω for the edges of the shell cut, all other factors being equal. In case (a), it is usually assumed that $\omega < 0$ ($\sigma_{ll} > 0$ on the inner shell surface and $\sigma_{ll} < 0$ on the outer surface). The opposite sign of $\omega > 0$ corresponds to case (b) ($\sigma_{ll} < 0$ on the inner shell surface and $\sigma_{ll} > 0$ on the outer surface). The interaction potential between a vacancy and the residual stress field is determined by the well-known relationship

$$V = \frac{\sigma_{ll}}{3}\Delta v, \quad (3)$$

where Δv is the change in the volume of the crystal when the vacancy is introduced. Since vacancies cause the decrease in the lattice parameter, one usually assumes that $\Delta v < 0$. The equilibrium vacancy concentration depends exponentially on potential V:

$$c_p = c_0 \exp\left(\frac{V}{kT}\right), \quad (4)$$

where c_0 is the averaged vacancy concentration. In the domain of compression of the shell material, the equilibrium vacancy concentration exceeds the mean value, since $V > 0$. The tensile stress reduces the equilibrium vacancy concentration as compared to the mean value, since $V < 0$. This physically means that, due to the relaxation of the residual stresses, vacancies migrate from the tensile domain to the compression domain, whereas the atomic flow proceeds in the opposite direction. The nonuniform field of the vacancy concentration creates concentration-induced stresses of the opposite sign of the residual stresses. These are calculated in a similar fashion as the thermal stresses [5]. The linear expansion coefficient corresponds to a change in the lattice parameter due to vacancy concentration.

To illustrate the relaxation kinetics of residual stresses, consider the compression domain ($r_0 \le r \le R_1$) of the shell material near its inner surface. This domain is bounded by the outer radius R_1, where $\sigma_{ll} = 0$ and, therefore, $V = 0$. Then, at $r = R_1$, the mean vacancy concentration remains unchanged due to the vacancy inflow from the tensile domain ($R_1 < r \le R$). The use of this illustrative example is explained by the fact that such a distribution of residual stresses leads to contact failure between the cylinder and shell owing to diffusion-induced vacancy flow. Diffusion-induced vacancy redistribution is described by the non-steady-state diffusion equation in the potential field V with corresponding initial and boundary conditions:

$$\frac{1}{D}\frac{\partial c}{\partial t} = \Delta c + \frac{\nabla(c\nabla V)}{kT}, \quad r_0 \le r \le R_1,$$
$$c(r,0) = c_0, \quad c(r_0,t) = c_p, \quad c(R_1,t) = c_0, \quad (5)$$

where D is the diffusion coefficient for vacancies and c_p is the equilibrium vacancy concentration at $r = r_0$. The rest notation is the same as used before. At the initial time instant, the vacancy concentration is equal to the mean value of c_0. The same concentration also remains at $r = R_1$, since at this boundary $V = 0$ and vacancies from the tensile domain ($R_1 < r \le R$) of the shell material migrate there. The boundary condition at $r = r_0$ indicates that the equilibrium vacancy concentration is immediately established, and further on, it remains unchanged in the process of diffusion-induced redistribution. Note that the field of compressive stresses in the vicinity of the inner shell surface is equivalent to the pressure inside the cylindrical cavity. If this pressure exceeds the Laplace pressure, the cavities enhance their radius as a result of vacancy flow. In the case under study, the field of compressive stresses is distributed nonuniformly and has a peak at boundary $r = r_0$. The existence of the compressive stresses in the whole range ($r_0 \le r \le R_1$), rather than at boundary $r = r_0$ only, increases the vacancy flow and the rate of increase for the inner shell radius. This is described by the second term in the right-hand side of Eq. (5). The logarithmic coordinate dependence of potential V essentially simplifies the diffusion equation in the force field. Since the vacancy diffusion depends on gradient ∇V of the potential, the constants in relationship (2) can be neglected. We have $\Delta V = 0$ because V is a harmonic function. The above discussion leads us to the following mathematical formulation of problem (5):

$$\frac{1}{D}\frac{\partial c}{\partial t} = \frac{\partial^2 c}{\partial r^2} + \frac{1+\alpha}{r}\frac{\partial c}{\partial r}, \quad r_0 \le r \le R_1, \quad (6)$$
$$\alpha = \frac{\mu\omega(1+\nu)\Delta v}{3\pi(1-\nu)kT}, \quad c(r,0) = c_0,$$
$$c(r_0,t) = c_p, \quad c(R_1,t) = c_0.$$

The dimensionless parameter α determines the contribution of the field of residual compressive stresses to the total diffusion-induced vacancy flow:

$$\mathbf{j} = -D\left(\frac{\partial c}{\partial r} - \frac{c}{kT}\frac{\partial V}{\partial r}\right) = -D\left(\frac{\partial c}{\partial r} + \frac{\alpha c}{r}\right). \quad (7)$$

At $\alpha \ll 1$, the field of residual stresses should be considered as a weak disturbance of the vacancy flow due to the concentration gradient. If $\alpha \gg 1$, the residual stresses prevail in the process of diffusion. At $\alpha \approx 1$, the

diffusion-induced vacancy flow related to the gradients of concentration and potential V are comparable. These vacancy flows have opposite directions: $\frac{\partial V}{\partial r}$ directs vacancies toward boundary $r = r_0$ and $\frac{\partial c}{\partial r}$ directs them from this boundary. The dynamic equilibrium determined by relationship (4) is achieved when these vacancy flows are equal. Any deviation from equilibrium (for example, a part of the vacancies being spent to the increase of the shell radius) is rapidly restored. As follows from the estimations, α is close to unity. Indeed, for $\mu \approx 5 \times 10^{10}$ Pa, $\omega = 0.1$ rad, $\nu \approx 0.3$, $\Delta v \approx 10^{-29}$ m^3, and $kT \approx 10^{-20}$ J, we obtain $\alpha \approx 1$. The sign of parameter α depends on ω and Δv. For our example, $\omega > 0$, $\Delta v < 0$, and, hence, $\alpha < 0$. Further on, without loss of generality, we assume that $\alpha = -1$. This allows us to emphasize the role of residual stresses due to diffusion-induced vacancy migration. At $\alpha = -1$, the solution to Eq. (6) describes the kinetics of diffusion-induced vacancy redistribution in the field of residual compressive stresses:

$$\frac{c - c_0}{c_p - c_0} = \frac{R_1 - r}{R_1 - r_0} - \frac{2}{\pi}\sum_{n=1}^{\infty}\frac{\sin\left[\frac{\pi n(r - r_0)}{R_1 - r_0}\right]}{n}\exp\left[-\frac{\pi^2 n^2 Dt}{(R_1 - r_0)^2}\right]. \quad (8)$$

The residual compressive stresses convert the problem from having cylindrical symmetry to being planar; i.e., the profile of concentration is formed in accordance to the planar symmetry. As a result, we have a higher formation rate for the vacancy concentration field. This directly follows from the form of diffusion equation (6). Indeed, at $\frac{\partial c}{\partial r} < 0$, the variation rate for the vacancy concentration $\frac{\partial c}{\partial t}$ at $\alpha = -1$ exceeds the corresponding value of $\frac{\partial c}{\partial t}$ at $\alpha = 0$. The equilibrium vacancy concentration determined by the competition of two diffusion processes is formed as $t \longrightarrow \infty$. Its profile is the linear function of coordinates. This results from our approximation ($\alpha = -1$), since $\exp\left(\ln\frac{r}{R}\right) = \frac{r}{R}$.

The increase in the inner shell radius due to the relaxation of residual stresses is governed by the diffusion-induced vacancy flow. Each vacancy exchanging positions with an atom causes an increase in the volume of the cylindrical hollow in the order of the atomic volume. In the quasi-equilibrium approximation (a slow process of shell radius variation is accompanied by a rapid tuning of the field of vacancy concentration), the rate of increasing the shell radius can be written as (under condition $c_p \ll 1$; i.e., the vacancy concentration at the boundary is significantly less than that in the hollow)

$$\frac{dr_0}{dt} = -\Omega N_0 D\left(\frac{\partial c}{\partial r} - \frac{c}{kT}\frac{\partial V}{\partial r}\right)_{r = r_0} = \frac{\Omega N_0 D(R_1 c_p - r_0 c_0)}{r_0(R_1 - r_0)} + \frac{2\Omega N_0 D(c_p - c_0)}{R_1 - r_0} \times \sum_{n=1}^{\infty}\exp\left[-\frac{\pi^2 n^2 Dt}{(R_1 - r_0)^2}\right], \quad (9)$$

where Ω is the atomic volume and N_0 is the number of atoms per unit volume. The rest notation coincides with the one previously used. In the framework of the model under consideration (the instantaneous attainment of equilibrium vacancy concentration at boundary $r = r_0$), the maximum rate of increase in the inner shell radius occurs at initial moments of time. Further on, this process becomes slower, and at $Dt/r_0^2 \gg 1$, the rate tends to the steady-state value

$$\frac{dr_0}{dt} = \frac{\Omega N_0 D(R_1 c_p - r_0 c_0)}{r_0(R_1 - r_0)}. \quad (10)$$

In general, the change in the radius δr_0 can be found by integrating expressions (9) and (10). At $R_1 c_p \gg r_0 c_0$, $\Omega N_0 \approx 1$, and $R_1 \gg r_0$, we have in the steady-state case

$$\frac{dr_0}{dt} \approx \frac{c_p D}{r_0} \longrightarrow \delta r_0 = \sqrt{2c_p Dt}; \quad (11)$$

i.e., we obtain the well-known relationship for the diffusion-induced change of characteristic sizes (e.g., at the growth of the new phase). The change in the shell radius δr_0 depends on the level of residual stresses, which determines the equilibrium vacancy concentration at boundary $r = r_0$. At $c_p \approx 10^{-4}$ atm, $D \approx 10^{-12}$ cm^2/s, and $t \approx 10^4$ s, we obtain $\delta r_0 \approx 10^{-6}$ cm. This value should be compared with the change in the shell radius due to the thermal expansion of the material:

$$\delta r_0 \approx \beta r_0 T, \quad (12)$$

where β is the coefficient of linear expansion and T is the increase in temperature. For $\beta \approx 10^{-6}$ K^{-1}, $T \approx 10^3$ K, and $r_0 \approx 1$ cm, we have $\delta r_0 \approx 10^{-3}$ cm. This means that on a macroscopic scale, the change in the entire shell radius resulting from the relaxation of residual stresses is essentially smaller in comparison with the thermal expansion of the shell material. In other words, the failure of thermal contact along the whole perimeter of the shell contacting with the cylinder in relation to the vacancy flow is possible only when the shell moves from the cylinder as a result of the difference in the

coefficients of linear expansion. At the contact boundary between the shell and the cylinder, there are, as a rule, discontinuities (hollows) of different nature. Their characteristic sizes are significantly smaller than the shell radius. Therefore, evolution of these discontinuities is determined by the diffusive relaxation of residual stresses, since the thermal increase of their size is relatively small. Indeed, for $r_1 = 10^{-4}$ cm (r_1 is the characteristic size of a hollow) under the same temperature conditions, we obtain $\delta r_1 = \beta r_1 T \approx 10^{-7}$ cm. The increase in size of the same hollow due to diffusion-induced vacancy flow under the conditions discussed above is $\delta r_1 \approx 10^{-6}$ cm. Thus, the local failure of the thermal contact between adjacent surfaces due to a diffusion-induced development of discontinuities is probably under a long-term thermal loading of construction elements. Naturally, this situation arises when residual compressive stresses exist on the inner surface of a cylindrical shell. If the residual stresses change their sign, then the inner shell radius becomes smaller and the discontinuities at the interface disappear. This is related to the fact that the diffusion-induced vacancy flow is now directed from the tensile domain ($r_0 \le r \le R_1$) to the compressive domain ($R_1 < r \le R$). The thermal contact between the surfaces becomes tighter. In this case, the mathematical treatment of the diffusion processes does not differ from those reported earlier.

REFERENCES

1. A. I. Lur'e, *Theory of Elasticity* (Nauka, Moscow, 1970).
2. V. A. Likhachev and R. Yu. Khaĭrov, *Introduction to the Theory of Disclinations* (Leningradsk. Gos. Univ., Leningrad, 1975).
3. N. M. Vlasov and V. A. Zaznoba, Dokl. Akad. Nauk **363**, 472 (1998) [Dokl. Phys. **43**, 761 (1998)].
4. N. M. Vlasov and V. A. Zaznoba, Fiz. Tverd. Tela (St. Petersburg) **41** (1), 64 (1999) [Phys. Solid State **41**, 55 (1999)].
5. I. I. Fedik, V. S. Kolesov, and V. N. Mikhaĭlov, *Temperature Fields and Stresses in Nuclear Reactors* (Énergoatomizdat, Moscow, 1985).

Translated by Yu. Vishnyakov

Doklady Physics, Vol. 45, No. 11, 2000, pp. 627–631. Translated from Doklady Akademii Nauk, Vol. 375, No. 3, 2000, pp. 338–342.
Original Russian Text Copyright © 2000 by Chashechkin, Kistovich, Il'inykh.

MECHANICS

Experimental Study of the Generation of Periodic Internal Waves by the Boundary Layer on a Rotating Disk

Yu. D. Chashechkin, Yu. V. Kistovich, and Yu. S. Il'inykh

Presented by Academician A. Yu. Ishlinskiĭ February 10, 2000

Received February 11, 2000

The exact solution to the linearized problem of the generation of internal waves, which involves internal waves and internal boundary flows [1], allows us to estimate errors intrinsic to the well-known method of force (or mass) sources [2]. In the case of small displacements, calculations of perturbances excited by an oscillating bar satisfactorily agree with the measurement results of [3]. There exist situations when a body moving periodically in continuously stratified viscous fluid does not radiate (in the linear case) and generates only isopycnic boundary flows. This situation takes place, e.g., in the case of a horizontal disk performing torsional vibrations [4]. However, by virtue of the nonlinear nature of the hydrodynamic system of equations, various forms of motion interfere with one another. In particular, thin-layer boundary flows can be a source of periodic waves [4]. Previously, experimental studies of such internal-wave generators were not conducted. Therefore, it is of interest to investigate the practical feasibility of the principles for nonlinear generation. In the present paper, the possibility of generation of three-dimensional beams of periodic internal waves by torsional vibrations of a horizontal disk are studied and the principal regularities connecting wave-field characteristics with the properties of a medium and source motion parameters are established.

The experiments were performed in a laboratory wave channel with dimensions $9.0 \times 0.6 \times 0.6$ m filled with an exponentially stratified solution of common salt, which had transparent windows made of optical glass. The period (for the frequency N) of the buoyancy

$$T_b = \frac{2\pi}{N} = 2\pi\sqrt{\frac{\Lambda}{g}},$$

where $\Lambda = \left(\frac{d\ln\rho_0}{dz}\right)^{-1}$ is the stratification scale, $\rho_0(z)$ is the density profile, and g is the free-fall acceleration, was determined by the density tag method [5] and was found in our experiment to be $T_b = 7.5$ s. Observations of the flow pattern in the vertical plane were performed by the shadow IAB-451 device using the method called "the vertical slit-thread in focus" [6]. Due to the symmetry of the flow pattern in the linearly stratified medium, the shadow device visualizes the perturbance distribution in the central vertical axis, where the light beam passes along the tangent to the wave phase surfaces. The rest contributions initiated by perturbances along the beam are mutually compensated. The measurements of wave displacements were carried out by an electrical-conduction single-electrode sensor and using sweep-vibration methods [7]. The sensor was calibrated before each experiment in accordance with the lifting-submersing procedure. The error of wave-displacement measurement did not exceed 20%.

The wave source was a horizontal disk 1 mm thick and 2 (or 4) cm in diameter. The disk was fixed to a vertical rod 2 mm in diameter, which was connected through a reducer to a dc motor. To reduce perturbances of the medium, the rod was placed in an immobile tube 6 mm in diameter. Adjustment of the rotation frequency and the law of disk motion was performed by varying the voltage applied to the motor. The angular displacement of the motor was recorded by a multiturn potentiometer. Three types of disk motion were studied: torsional harmonic vibrations (with the angular velocity $\Omega = \Omega_0\sin\omega^* t$); intermittent alternate rotations (meander)

$$\Omega = \Omega_0\begin{cases} +\Omega_0, & nT < t < nT + \frac{T}{2} \\ -\Omega_0, & nT + \frac{T}{2} < t < nT + T, \end{cases}$$

where $T = 2\pi/\omega^*$; and harmonic torsional vibrations against the background of a uniform rotation ($\Omega = A + \Omega_0\sin\omega^* t$). The maximum linear velocity for the disk edge motion was $U = 10$ cm/s.

The flow shadow pattern appearing after the completion of two 4-cm-disk vibrations is shown in Fig. 1. Among the optical inhomogeneities of the pattern, we

Institute of Problems in Mechanics,
Russian Academy of Sciences,
pr. Vernadskogo 101, Moscow, 117526 Russia

1028-3358/00/4511-0627$20.00 © 2000 MAIK "Nauka/Interperiodica"

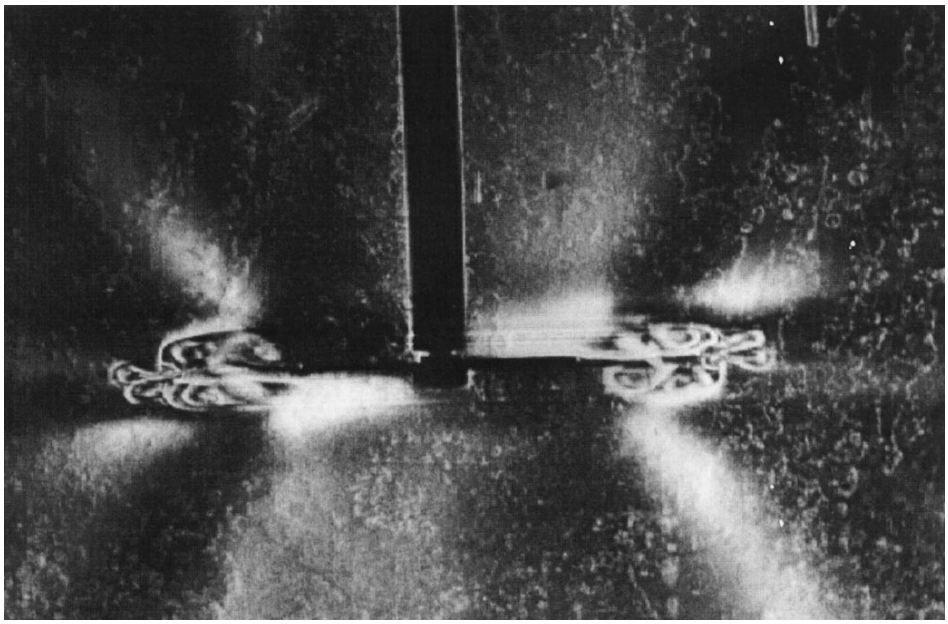

Fig. 1. Shadow pattern of a flow formed by a horizontal disk performing torsional vibrations; T_b = 7.5 s, T = 20 s, U = 2 cm/s.

can distinguish a sequence of thin strips positioned in parallel to the disk, which are linked by three embedded ring-shaped structures. Two systems of inclined, almost horizontal, diffusive dark and light strips branch out of the external surface of the layered structure. In the upper half space, the interior strip is dark, whereas in the lower one, the opposite situation takes place. Horizontal strips are antisymmetric to both the right and the left. The positions of the horizontal interlayers, as well as the size and shape of the vortices linking these interlayers, and the mutual positions of the dark and light inclined strips vary with time.

Comparison with the results of [3, 8] for shadow observations of stratified flows shows that inclined diffusive strips represent schematically periodic internal waves with frequency $\omega = 2\omega^* = 0.62$ s^{-1}, which propagate at an angle $\theta = 47°$ to the horizon, as well as diffusive horizontal strips, i.e., waves of the zero frequency, and high-gradient interlayers, i.e., shells of rotating ring-shaped flows at the disk edge. The distribution of optical perturbances in the shadow image, when the blackening density is determined by the horizontal component of the refractive index (or the density) bound by the linear relationship [8], testifies to the existence of an antisymmetric pattern of periodic waves: a crest in the upper half space corresponds to a hollow in the lower one and vice versa.

Observations of the flow pattern show that at the initial phase of the flow, boundary flows arise at both disk sides; each of these flows forms a circular flow rotating together with the disk, the cross section of this flow having an annular shape. The large and small ring radii monotonically increase with time up to the moment of changing the rotation direction. At this moment, the flow separates from the disk and begins to attenuate. As far as the ring-shaped flow is being damped, its vertical dimension decreases and its vortices collapse. In the case of changing the rotation direction (at every half of a period), a new pair of boundary flows and, correspondingly, a pair of new monotonically raising annular flows arise. In each of these flows, the fluid takes part in two types of rotary movement, namely, around the vertical disk axis in the horizontal plane and in the vertical plane around the circular symmetry axis. As in the uniform medium, the disk forms the middle flow [9], in which the fluid flows along the vertical axis and is thrown away in the disk plane forming a wave beam of zero frequency in the stratified medium. The direction of the middle flow induced by the disk is independent of its rotation direction.

In the shadow pattern (Fig. 1), we observe traces of three pairs of annular flows. The first (outer) flow pair has collapsed under the action of buoyancy forces; the second (central) pair has a clearly expressed annular structure similar to the vortex structure in a homogeneous fluid [10]; and the third pair intervenes in them. The external boundaries of annular flows are seen above and below the disk as thin horizontal interlayers. Their thickness does not exceed 0.3 mm and, in fact, is determined by the resolution of the shadow device [6]. The shape of the exterior annular flow demonstrates that the mixing of the fluid inside this flow is weak, since its fragments come to the disk horizon within the observation time.

The outer boundary of annular flows being formed near the disk radiates two groups of axisymmetric periodic internal waves at a frequency $\omega = 2\omega^*$. These waves propagate at an angle $\theta = 47°$ to the horizon. Fur-

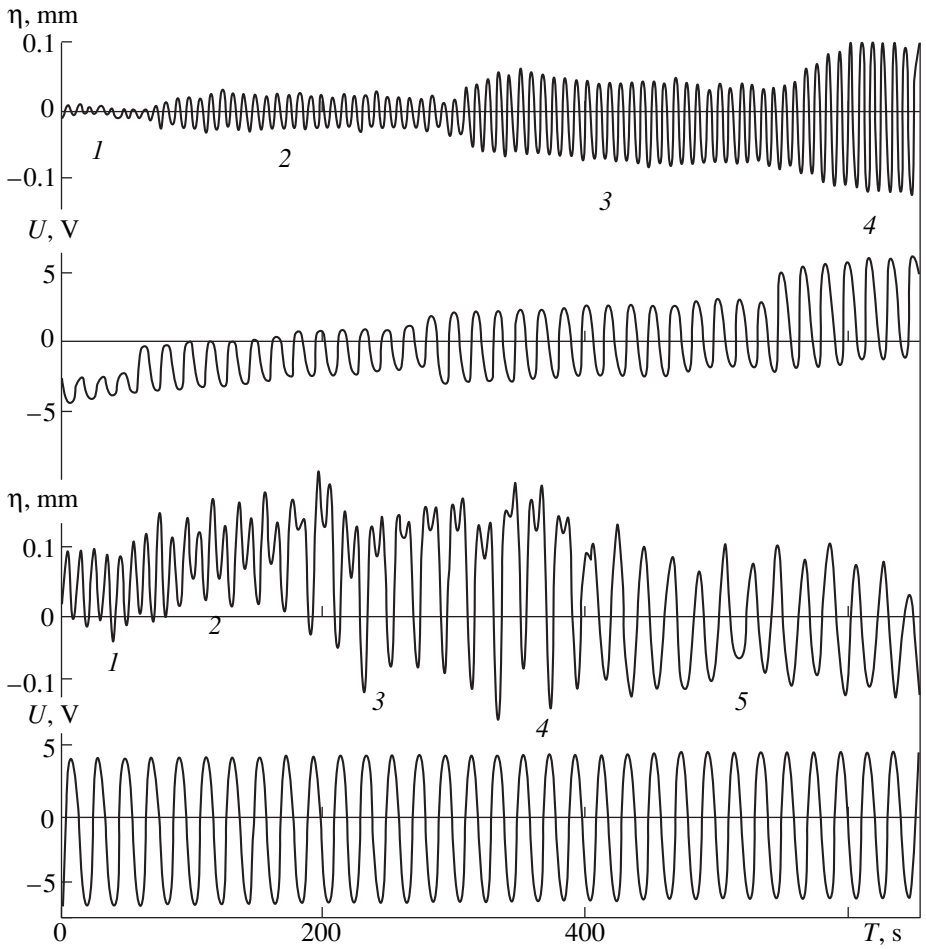

Fig. 2. Recorded signals of electrical-conductance and disk position sensors.

thermore, all elements of this pattern are repeated in every half of a period and the common-rotation direction of annular vortices in the horizontal plane changes.

The signals registered from the electrical-conductance sensor installed in the internal-wave beam at a distance of 8 cm from the disk (the sensitive element of the sensor is depicted in the upper right angle of Fig. 1) are shown in Fig. 2. In the same figure, the signals from the disk angular position for which a multiturn potentiometer is used is also presented. The upper pair of records corresponds to the case when the 4-cm disk performs harmonic torsional vibrations at a constant frequency and with different amplitudes [(*1–4*): U = 0.4, 1.3, 3.5, and 5.8 cm/s]. Stable internal waves are excited at all velocities of disk motion. Comparing the upper pair of records, we can see that the frequency of the radiated wave exceeds that for the torsional vibrations by a factor of two. The small amplitude modulation of the signal is initiated by seiches existing in the basin. The drift of the potentiometer signal with time is caused by the specific asymmetry of the control signal and by features of the motor operation in itself. The internal-wave amplitude increases linearly with the torsional-vibration amplitude [(*1–4*): η = 0.01, 0/03, 0/06. 0.11 cm].

The lower pair of the records in Fig. 2 corresponds to the case when, in addition to the alternating voltage, the permanent voltage is applied to the motor. The value representing this voltage consequently becomes equal to the harmonic-signal amplitude and, furthermore, exceeds it. In this case, torsional harmonic vibrations of the 2-cm disk ($U\sin\omega^* t$, U = 2.8 cm/s, ω^* = 0.31 s^{-1}) are added to the unidirectional rotation (with velocity values *1–5*, respectively, of 0, 1.0, 3.5, 6.0, and 9.8 cm/s) and are gradually transformed into motion with the alternate angular velocity of the constant sign ($U_0 > U$). In the sensor signal which is initially harmonic and has the frequency $2\omega^*$, a noticeable component appears that becomes dominating with further increase in the permanent rotation component (see segment *3*). In this case, the energy of emitted waves also increases.

The dependence of the vertical displacements in the internal-wave beam on the maximum velocity of the disk edge in the case of purely torsional vibrations is presented in Fig. 3 (the sensor is placed at a distance of

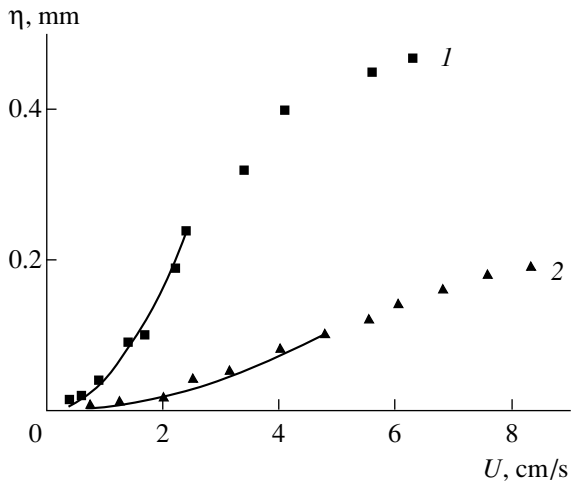

Fig. 3. Vibration amplitudes for particles on the internal-wave beam axis as a function of the disk edge rotation velocity: (*1*) $D = 4$ and (*2*) 2 cm.

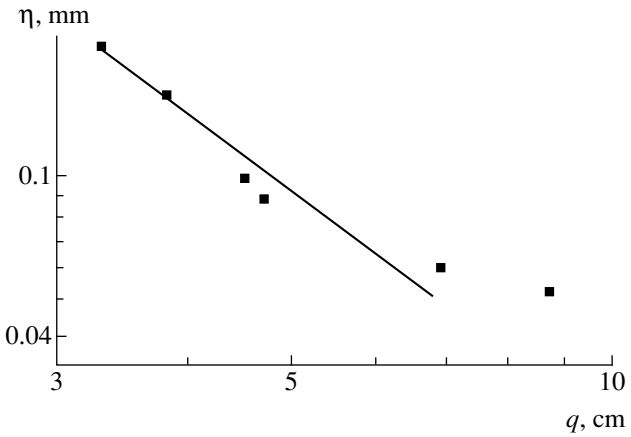

Fig. 4. Vibration amplitude for particles on the beam axis as a function of the distance to the radiator ($T_b = 7.5$ s, $D = 4$ cm, $T = 16.7$ s, $U = 2$ cm/s).

8 cm from the disk along the beam axis). At low rotation velocities of the disk ($U < 3$ cm/s), the wave amplitude increases quadratically for the radiators of both diameters ($D = 2$ and 4 cm: $\eta = 0.005U^2$ and $0.04U^2$; η and U are expressed in millimeters and centimeters per second, respectively, see curves *1* and *2*). At intermediate velocities, the amplitude-increase rate is gradually slowed, and for $U > 8$ cm /s, saturation takes place owing to the combined action of the nonlinearity and viscosity effects.

The plot illustrating the attenuation of particle displacement amplitudes at the beam axis as a function of the distance to the radiator is presented in the double-logarithmic scale in Fig. 4. Making use of the least-squares method shows that for $q < 7$ cm, experimental points are grouped around the curve $\eta = 1.14q^{-1.54}$. At longer distances ($q > 7$ cm), the recorded wave amplitude attains saturation (the vertical displacement is on the order of 0.05 mm) caused by the wave background of the basin. This background is formed due to the action of other independent sources (mechanical vibrations of the ground, as well as vibrations of the base and walls of the basin, which are caused by the action of the wave-producing device). The level of residual vibrations in Fig. 4 corresponds to the modulation depth in Fig. 2.

As was shown in the experiments, the amplitude of the wave being radiated substantially depends on the characteristics of disk motion (under the condition of preserving the frequency and amplitude for its periodic component). When the envelope is a meander, only annular flows and waves are observed in the flow pattern (running internal waves are absent).

As is shown in the theory of the excitation of internal waves by the horizontal disk performing the torsional vibrations in a stratified viscous fluid [4], the true wave source is an isopycnic boundary flow characterized by a single azimuth velocity component u_φ. The stream function Ψ for the beam of radiated waves satisfies the equation

$$\left[\frac{\partial^2}{\partial t^2}\left(\Delta - \frac{1}{r^2}\right) + N^2\left(\Delta - \frac{\partial^2}{\partial z^2}\right) - \nu\frac{\partial}{\partial t}\left(\Delta - \frac{1}{r^2}\right)^2\right]\Psi = \frac{1}{r}\frac{\partial^2 u_\varphi^2}{\partial t \partial z}, \quad (1)$$

where Δ is Laplacian, ν is the kinematic viscosity, and the origin of the cylindrical coordinate system (r, φ, z) is taken in the disk center. The solution to this equation with exact boundary conditions describes both running waves [4] and zero-frequency waves. The form of the right-hand side of Eq. (1) implies that the frequency of waves excited by harmonic torsional vibrations of the disk is twice that of their own frequency. The meander squared is a quantity independent of time, which explains the radiative inefficiency of the periodic motion of this type.

It follows from the solution to Eq. (1) that torsional vibrations of a disk whose radius is smaller than the viscous wave scale $L_V = \sqrt[3]{g\nu}/N$ excite a single-mode wave beam. The displacements of the particles along the beam axis are

$$h(q) = \frac{U^2R^2\sin\theta}{48(1+\sqrt{2})}\left(\frac{2\cos^4\theta}{\pi^3\nu^4N^8q^{10}}\right)^{1/6}\Gamma\left(\frac{7}{6}\right), \quad (2)$$

where Γ is the gamma function and q is the distance along the beam axis to the source. The quadratic dependence of the wave amplitude on the velocity U in (2) is consistent with the measurement data exhibited in Fig. 3. In this theory, the wave amplitude also depends quadratically on the disk radius. The ratio of the coefficients in formulas interpolating experimental data of Fig. 3 is equal to 8, whereas the ratio squared for disk

diameters is 4. This discrepancy is associated with the fact that under the experimental conditions, the waves excite both isopycnic boundary flows and annular rotating vortices. The efficiency of the second generation mechanism that is not taken into account in the theory elevates with increasing disk diameter. The decrease in the beam amplitude with the distance from the source, which is calculated in accordance with (2) under the experimental conditions presented in Fig. 4, is given by the expression $h = 1.29q^{-5/3}$, where h and q are expressed in millimeters and centimeters, respectively. For $q < 7$, empirical data can be approximated by the dependence $h = 1.14q^{-1.54}$. Deviations in the indices (8%) and coefficients (13%) do not exceed the measurement error for the wave amplitudes by the contact electrical-conductance sensor, which attains 20% in the experiments under discussion. Thus, the disk performing high-amplitude torsional vibrations in the continuously stratified fluid efficiently radiates periodic internal waves.

The method described expands the spectrum of possible means for excitation of internal waves including wave generation under the action of viscous stresses [11], as well as by varying the volume and position of a body [12].

ACKNOWLEDGMENTS

This work was carried out under the financial support of the Ministry of Science and Technology of the Russian Federation (in the framework of the Program of Supporting Unique Experimental Facilities) and of the Russian Foundation for Basic Research, project no. 99-05-64980.

REFERENCES

1. Yu. D. Chashechkin and Yu. V. Kistovich, Dokl. Akad. Nauk **355**, 54 (1997) [Phys. Dokl. **42**, 377 (1997)].
2. M. G. Lighthill, *Wave in Fluids* (Cambridge Univ. Press, Cambridge, 1978; Mir, Moscow, 1981).
3. Yu. S. Il'inykh, Yu. V. Kistovich, and Yu. D. Chashechkin, Izv. Akad. Nauk, Fiz. Atm. Okeana **35**, 649 (1999).
4. Yu. V. Kistovich and Yu. D. Chashechkin, Dokl. Akad. Nauk **367**, 636 (1999) [Dokl. Phys. **44**, 573 (1999)].
5. S. A. Smirnov, Yu. D. Chashechkin, and Yu. S. Il'inykh, Izmer. Tekh., No. 6, 15 (1998).
6. L. A. Vasil'ev, *Schlieren Methods* (Nauka, Moscow, 1968; Israel Program for Scientific Translations, Jerusalem, 1971).
7. A. V. Gvozdev, V. I. Neklyudov, and Yu. D. Chashechkin, Izmer. Tekh., No. 3, 33 (1990).
8. D. E. Mowbray, J. Fluid Mech. **27**, 595 (1967).
9. H. Schlichting, *Theory of Boundary Layers* (McGraw-Hill, New York, 1955; Nauka, Moscow, 1960).
10. *Album of Fluid Motion*, Ed. by M. VanDyke (Parabolic Press, Stanford, 1982; Mir, Moscow, 1986).
11. A. V. Kistovich and Yu. D. Chashechkin, Prikl. Mekh. Tekh. Fiz. **40** (6), 31 (1999).
12. S. A. Makarov, V. I. Neklyudov, and Yu. D. Chashechkin, Izv. Akad. Nauk SSSR, Fiz. Atm. Okeana **26** (7), 744 (1990).

Translated by G. Merzon

Doklady Physics, Vol. 45, No. 11, 2000, pp. 632–634. Translated from Doklady Akademii Nauk, Vol. 375, No. 3, 2000, pp. 343–346.
Original Russian Text Copyright © 2000 by Shamolin.

MECHANICS

Integrability according to Jacobi in the Problem of Motion of a Four-Dimensional Solid in a Resistant Medium

M. V. Shamolin

Presented by Academician A. Yu. Ishlinskiĭ December 27, 2000

Received February 29, 2000

In [1, 2], the complete integrability for a two-dimensional problem of motion of a solid in a resistant medium under jet flow was shown. In this situation, for a system of dynamic equations there exists one first integral, which is a transcendental function (in the sense of the theory of functions for complex variables, which have essential singularities) of quasi-velocities. In the above-mentioned studies, the overall interaction between the medium and the body was assumed to be concentrated on a part of the body's surface that has the shape of a (one-dimensional) plate.

More recently [3, 4], the two-dimensional problem was generalized for the spatial (three-dimensional) case. In this instance, the system of dynamic equations has a complete set of first integrals: one analytic, one meromorphic, and one transcendental. In this event, the overall interaction between the medium and the body is assumed to be concentrated on a part of the body's surface that has the shape of a flat (two-dimensional) disk.

Every so often, the structure of the dynamic equations of motion is conserved when the dynamic properties are extended to cases of higher dimension. For example, a theory of motion for a four-dimensional (or even *n*-dimensional) solid is currently being developed [5, 6]. The authors of those papers succeeded in demonstrating that the equations of motion near an immobile point are Hamiltonian equations for a multidimensional solid. The present paper deals with study of the motion of the so-called four-dimensional solid interacting with a resistant medium according to the laws of jet flow. The results of this type of study are presented for the first time.

In this paper, the overall interaction of a (four-dimensional) solid with a medium is assumed to be concentrated on the (three-dimensional) part of the body's surface that has the shape of a (three-dimensional) sphere. In this case, the vector of the angular velocity of motion for the body is six-dimensional and the center-of-mass velocity is four-dimensional.

Setting up the problem and equations on the *so*(4) group. We assume that a four-dimensional solid moves in a resistant medium filling in a four-dimensional domain of a Euclidean space and that the overall interaction of the medium with the body is concentrated on a (three-dimensional) part of the body's surface that has the shape of a three-dimensional disk D^3. The distance between the point N of the resistance force application and the center D of the disk is a function of only one parameter. This parameter is the angle of attack α measured between the vector of the velocity $\mathbf{v}$ at the point D and the middle perpendicular to the disk drawn from the body's center of mass C in a four-dimensional space (cf. [2, 4]).

In the four-dimensional space, the resistance is normal to the disk D^3; the resistance force can be written out in the form $S = s_1(\alpha)v^2$, where s_1 is the nonnegative resistance coefficient.

We relate the coordinate system $Dx_1x_2x_3x_4$ to the body; the axis Dx_1 of the system coincides with the axis CD and the axes Dx_2, Dx_3, and Dx_4 lie in the disk hyperplane.

If the inertia operator is of the diagonal form $\mathrm{diag}\{I_1, I_2, I_3, I_4\}$ in the system $Dx_1x_2x_3x_4$ and Ω is the angular velocity matrix for the solid, i.e., $\Omega \in so(4)$, then the part of the equations of motion for the four-dimensional solid corresponding to the group $so(4)$ has the following form [5–7]:

$$\Omega^{\cdot}\Lambda + \Lambda\Omega^{\cdot} + [\Omega, \Omega\Lambda + \Lambda\Omega] = M. \qquad (1)$$

Here,

$$\Lambda = \mathrm{diag}\{\lambda_1, \lambda_2, \lambda_3, \lambda_4\},$$

$$\lambda_1 = \frac{1}{2}(-I_1 + I_2 + I_3 + I_4), \ldots,$$

$$\lambda_4 = \frac{1}{2}(I_1 + I_2 + I_3 - I_4),$$

Institute of Mechanics, Moscow State University, Michurinskiĭ pr. 1, Moscow, 117192 Russia

1028-3358/00/4511-0632$20.00 © 2000 MAIK "Nauka/Interperiodica"

M is the moment of external forces acting on the body in R^4 and projected onto the "natural" coordinates in $so(4)$, and $[\cdot]$ is the commutator in $so(4)$. The matrix $\Omega \in so(4)$ is conveniently expressed in terms of the following natural coordinates:

$$\begin{pmatrix} 0 & -\omega_6 & \omega_5 & -\omega_3 \\ \omega_6 & 0 & -\omega_4 & \omega_2 \\ -\omega_5 & \omega_4 & 0 & -\omega_1 \\ \omega_3 & -\omega_2 & \omega_1 & 0 \end{pmatrix}. \quad (2)$$

Here, ω_1, ω_2, ω_3, ω_4, ω_5, and ω_6 are the components of the angular velocity in projections onto the natural coordinates in $so(4)$.

The resistance coefficient s_1 is conveniently presented in the form $s_1(\alpha) = s(\alpha)\,\mathrm{sgn}\cos\alpha$. If $(0, x_{2N}, x_{3N}, x_{4N})$ are the coordinates of the point N in the system $Dx_1x_2x_3x_4$ and $\{-S, 0, 0, 0\}$ is the coordinates of the resistance vector in the same system, then the following mapping should be constructed for calculating the resistance moment:

$$R^4 \times R^4 \longrightarrow so(4). \quad (3)$$

This mapping transforms a pair of vectors from R^4 to a certain element of the group $so(4)$.

The resistance moment is of the following form in projections onto the coordinates in the $so(4)$ group:

$$(0, 0, x_{4N}S, 0, -x_{3N}S, x_{2N}S) \in R^6 \simeq M \in so(4). \quad (4)$$

Here, we should take into account that $x_{2N} = R(\alpha)\cos\beta_1$, $x_{3N} = R(\alpha)\sin\beta_1\cos\beta_2$, and $x_{4N} = R(\alpha)\sin\beta_1\sin\beta_2$ if $(v, \alpha, \beta_1, \beta_2)$ are the spherical coordinates in R^4.

With allowance made for all these points, we can arrive at the following equations of motion in the resistance field under consideration:

$$(\lambda_4 + \lambda_3)\dot{\omega_1} + (\lambda_3 - \lambda_4)(\omega_3\omega_5 + \omega_2\omega_4) = 0, \quad (5)$$

$$(\lambda_2 + \lambda_4)\dot{\omega_2} + (\lambda_2 - \lambda_4)(\omega_3\omega_6 - \omega_1\omega_4) = 0, \quad (6)$$

$$(\lambda_4 + \lambda_1)\dot{\omega_3} + (\lambda_4 - \lambda_1)(\omega_2\omega_6 + \omega_1\omega_5) = x_{4N}S, \quad (7)$$

$$(\lambda_3 + \lambda_2)\dot{\omega_4} + (\lambda_2 - \lambda_3)(\omega_5\omega_6 + \omega_1\omega_2) = 0, \quad (8)$$

$$(\lambda_1 + \lambda_3)\dot{\omega_5} + (\lambda_3 - \lambda_1)(\omega_4\omega_6 - \omega_1\omega_3) = -x_{3N}S, \quad (9)$$

$$(\lambda_1 + \lambda_2)\dot{\omega_6} + (\lambda_1 - \lambda_2)(\omega_4\omega_5 + \omega_2\omega_3) = x_{2N}S. \quad (10)$$

Dynamics on R^4. By analogy with the three-dimensional case, expressions similar to Euler and Rivals formulas can be derived; i.e., in an arbitrary coordinate system, the velocities and accelerations for two arbitrary points A and B of a four-dimensional solid are connected by the following relations:

$$v_B = v_A + \Omega AB, \quad w_B = w_A + \Omega^2 AB + \mathbf{E}AB. \quad (11)$$

Here, $\Omega \in so(4)$ and $\mathbf{E} = \dot{\Omega} \in so(4)$. The matrix $\mathbf{E}$ is referred to as the acceleration matrix.

Equations of motion for the center of mass of a four-dimensional solid in R^4 can be derived employing formulas (11).

Motion in a resistant medium under the action of servo coupling (cf. [1, 4]). We consider a class of body motion for which the following condition is obeyed at all times:

$$v = \text{const}. \quad (12)$$

We also assume that a certain (servo) pulling force acts on the body; the force ensures that condition (12) is fulfilled and is a reaction of a given servo coupling (cf. the two- and three-dimensional cases [1–4]).

The fulfillment of condition (12) can be attained using a specific choice for the magnitude of the pulling force along the straight line CD.

The case of a dynamically-symmetric solid. We suppose that, by analogy with the three-dimensional case, the following equalities are obeyed:

$$I_2 = I_3 = I_4. \quad (13)$$

In such an event, there exist three cyclic first integrals for Eqs. (5)–(10):

$$\omega_1 = \omega_1^0, \quad \omega_2 = \omega_2^0, \quad \omega_4 = \omega_4^0.$$

For simplicity, we consider motions at zero levels:

$$\omega_1^0 = \omega_2^0 = \omega_4^0 = 0. \quad (14)$$

For describing the body motion, a pair of dynamic functions $(R(\alpha), s(\alpha))$ is used, information about which is of a qualitative nature. By analogy with low-dimensional cases, without loss of generality for [1–4], we can assume that

$$R(\alpha) = A\sin\alpha, \quad A > 0, \quad s(\alpha) = B\cos\alpha, \quad B > 0.$$

As a result, in a part of $so(4)$, the equations take the following form $\left(\text{here, } n_0^2 = \dfrac{AB}{2I_2}\right)$:

$$\dot{\omega_3} = n_0^2 v^2 \sin\alpha\cos\alpha\sin\beta_1\sin\beta_2, \quad (15)$$

$$\dot{\omega_5} = -n_0^2 v^2 \sin\alpha\cos\alpha\sin\beta_1\cos\beta_2, \quad (16)$$

$$\dot{\omega_6} = n_0^2 v^2 \sin\alpha\cos\alpha\cos\beta_1. \quad (17)$$

If the natural replacement of the angular velocities is introduced according to the formulas

$$z_1 = \omega_3\cos\beta_2 + \omega_5\sin\beta_2, \quad (18)$$

$$z_2 = -\omega_3\sin\beta_2\cos\beta_1 + \omega_5\cos\beta_2\cos\beta_1 + \omega_6\sin\beta_1, \quad (19)$$

$$z_3 = \omega_3 \sin\beta_2 \sin\beta_1 - \omega_5 \cos\beta_2 \sin\beta_1 + \omega_6 \cos\beta_1, \quad (20)$$

then the combined equations of motion on $so(4) \times R^4$ [with the four conditions in (12) and (14) taken into account] acquire the symmetric form

$$\begin{aligned}
\alpha^{\cdot} &= -z_3 + \sigma n_0^2 \nu \sin\alpha,\\
z_3^{\cdot} &= n_0^2 \nu^2 \sin\alpha\cos\alpha - (z_1^2 + z_2^2)\frac{\cos\alpha}{\sin\alpha},\\
z_2^{\cdot} &= z_2 z_3 \frac{\cos\alpha}{\sin\alpha} + z_1^2 \frac{\cos\alpha}{\sin\alpha}\frac{\cos\beta_1}{\sin\beta_1}, \qquad (21)\\
z_1^{\cdot} &= z_1 z_3 \frac{\cos\alpha}{\sin\alpha} - z_1 z_2 \frac{\cos\alpha}{\sin\alpha}\frac{\cos\beta_1}{\sin\beta_1},\\
\beta_1^{\cdot} &= z_2 \frac{\cos\alpha}{\sin\alpha};\\
\beta_2^{\cdot} &= -z_1 \frac{\cos\alpha}{\sin\alpha\sin\beta_1}. \qquad (22)
\end{aligned}$$

The sixth-order system of Eqs. (21), (22) has an independent subsystem (21) of the fifth order. In general, for complete integration of the given system, we need to know five independent first integrals. However, after substituting the variables

$$z_1, z_2 \longrightarrow z = \sqrt{z_1^2 + z_2^2}, \quad z_* = \frac{z_2}{z_1}, \qquad (23)$$

system (21), (22) can be reduced to the following form:

$$\begin{aligned}
\alpha^{\cdot} &= -z_3 + \sigma n_0^2 \nu \sin\alpha,\\
z_3^{\cdot} &= n_0^2 \nu^2 \sin\alpha\cos\alpha - z^2 \frac{\cos\alpha}{\sin\alpha}, \qquad (24)\\
z^{\cdot} &= z z_3 \frac{\cos\alpha}{\sin\alpha};\\
z_*^{\cdot} &= \sqrt{1 + z_*^2}\, z \frac{\cos\alpha}{\sin\alpha}\frac{\cos\beta_1}{\sin\beta_1},\\
\beta_1^{\cdot} &= \frac{z z_*}{\sqrt{1 + z_*^2}}\frac{\cos\alpha}{\sin\alpha}; \qquad (25)\\
\beta_2^{\cdot} &= -z_1(z, z_*)\frac{\cos\alpha}{\sin\alpha\sin\beta_1}. \qquad (26)
\end{aligned}$$

The fifth-order system of Eqs. (21) is seen to be decomposed into independent subsystems of even lower order: system (24) is of the third order and system (25) (after the replacement of time) is of the second order. Thus, for complete integrability of system (24)–(26), it is sufficient to indicate two independent integrals of system (24): one for system (25) and an additional integral attaching Eq. (26).

System (24) appears in the dynamics of a three-dimensional solid [4]. It has two transcendental integrals:

$$\frac{z^2 + z_3^2 - \sigma n_0^2 \nu z_3 \sin\alpha + n_0^2 \nu^2 \sin^2\alpha}{z\sin\alpha} = C_1 = \text{const}, \qquad (27)$$

$$G\left(\frac{z}{\sin\alpha}, \frac{z_3}{\sin\alpha}, \sin\alpha\right) = C_2 = \text{const}. \qquad (28)$$

The first integral of system (25) has the form

$$\frac{\sqrt{1 + z_*^2}}{\sin\alpha} = C_3 = \text{const}. \qquad (29)$$

In turn, the additional first integral is of the form

$$\pm\frac{\cos\beta_1}{\sqrt{C_3^2 - 1}} = \sin\{C_3(\beta_2 + C_4)\}, \quad C_4 = \text{const}. \qquad (30)$$

Conclusion. Previously, only motions of a four-dimensional body were considered for $M \equiv 0$. The present paper opens up new lines of thinking, i.e., the investigation of equations of motion for a solid on $so(4) \times R^4$ ($M \neq 0$).

As for the technique of integrating the dynamic systems under consideration, it can also be extended, almost without exception, to the $so(n) \times R^n$ space of an arbitrary dynamically symmetric n-dimensional solid.

REFERENCES

1. V. A. Samsonov and M. V. Shamolin, Vestn. Mosk. Univ., Ser. 1: Mat., Mekh., No. 3, 51 (1989).
2. V. A. Samsonov and M. V. Shamolin, *Model Problem on Body Motion in a Fluid with Jet Flow*, Scientific Report of the Institute of Mechanics, Moscow State University No. 3969 (Moscow, 1990).
3. M. V. Shamolin, Izv. Akad. Nauk, Mekh. Tverd. Tela, No. 2, 65 (1997).
4. M. V. Shamolin, Dokl. Akad. Nauk **364**, 627 (1999) [Dokl. Phys. **44**, 110 (1999)].
5. O. I. Bogoyavlenskiĭ, Dokl. Akad. Nauk SSSR **287**, 1105 (1986) [Sov. Phys. Dokl. **31**, 309 (1986)].
6. O. I. Bogoyavlenskiĭ, Dokl. Akad. Nauk SSSR **272**, 1364 (1983) [Sov. Phys. Dokl. **28**, 858 (1983)].
7. V. V. Trofimov and A. T. Fomenko, Itogi Nauki Tekh., Sovrem. Probl. Mat. Nov. Dostizh. (VINITI, Moscow, 1986), vol. 29, pp. 3–80.

Translated by V. Tsarev